Development and Application of a Coupled Atmospheric and Hydrological Modelling System

Inaugural-Dissertation
zur
Erlangung des Doktorgrades
der Mathematisch-Naturwissenschaftlichen Fakultät
der Universität zu Köln

vorgelegt von
Qian Xia
aus Hunan, China

Köln
2019

Berichterstatter: Prof. Dr. Y. Shao
Prof. Dr. K. Schneider

Tag der mündlichen Prüfung: 23. 10. 2018

Abstract

A complete simulation for the regional water cycle and the catchment-scale hydrological response to climate change requires hydro-meteorological models, which represent the relevant processes taking place in the atmosphere, at the land surface, and in the subsurface, as well as their interactions. In this study, a coupled Atmospheric and Hydrological Modelling System (AHMS) is developed by two-way coupling the atmospheric model WRF and the distributed hydrological model HMS via the land surface model Noah-MP LSM. This fully coupled system enables to explicitly describe hydrological processes for the atmospheric modelling at catchment and continental scale. The Huaihe basin in China is selected as a study case.

A new parameterization of hillslope runoff is developed by considering the effect of hillslope topography on infiltration capacity. This new parameterization is first applied in the coupled land surface and hydrological model NoahMP-HMS that is offline driven by surface meteorological data. The offline simulations with and without the new parameterization are compared to the observations. The comparison shows that this new parametrization significantly enhances the production of surface runoff. By including this enhancement in the runoff estimates, the NoahMP-HMS can reproduce the hydrological processes within the Huaihe basin and the regional water balance at high precision. It is revealed by the statistical evaluations. The Nash-Sutcliffe efficiency coefficients (NSIs) are 0.67, 0.81, and 0.80 for the simulated daily streamflow from 1980 to 1987 at three hydrological stations in the main river; and their water balance indexes (WBIs) are close to 1.0.

The spatiotemporal variability of hydrological processes in the basin is studied, based on the NoahMP-HMS simulation from 1979 to 2003. On monthly scale, the change of water storage in the aquifer is linearly correlated to net precipitation. Due to a large amount of net precipitation from June to August, the groundwater table starts uplifting from June and reaches its maximum in September. Over the basin, deep groundwater is found in the mountains, and shallow groundwater at the foothills of the mountains and in the downstream plains. The monthly precipitation largely determines the monthly runoff in the basin, nevertheless, the runoff shows a larger temporal variability. Throughout the year, the groundwater continuously supplies water for the rivers, while the surface runoff shows an obvious monthly variation. Furthermore, the runoff coefficients in the mountains are significantly higher than in the plains, which implies a high flood risk by the intense rainfall in this region.

The AHMS with the new parameterization is used for the coupled atmospheric and

hydrological simulation in the Huaihe basin from July to November 1991. The evaluation of AHMS results with the observations indicates that the AHMS performs well in modelling atmospheric variables and provides reasonable daily streamflow estimates (NSIs = 0.55, WBIs = 0.63–0.79). Compared to the stand-alone WRF simulation, the soil water dynamics behaves differently in the AHMS simulation, on which the impact of hydrological processes is associated with groundwater depth. Under suction of deep unsaturated soil and gravity effect, soil drainage occurring at the bottom of soil model domain is higher than gravitational drainage (in WRF); it results in drier soil conditions in the mountains. Groundwater is capable of moistening overlaying soil by capillary rise; these capillary fluxes widely occur in the relatively deep groundwater region, especially in dry soil conditions, which efficiently recharges soil water content. Besides, gravitational water can accumulate above groundwater table and laterally flows, which is described in the AHMS but not in the WRF; consequently, the soil moisture in the shallow groundwater region (depths of 0–2 m) is significantly higher (increased by 26%) in the AHMS.

Due to the spatial variation of groundwater depth in the basin, the impact of the coupled atmospheric and hydrological simulation on soil moisture presents a large spatial variability. Consistently, the shift of evaporation and air temperature exhibits a similar spatial patter as that of soil moisture. On average, the embedment of hydrological processes into the AHMS results in higher soil moisture (by 7%) and evaporation (by 8%), as well as lower air temperature (-0.2 ºC) in the Huaihe basin. Their effect on basin-averaged precipitation is insignificant, but results in a spatial redistribution of precipitation in the basin, with local changes up to ±30%.

In summary, the simple, but efficient parameterization of hillslope runoff is achieved. Benefiting from it, the model captures well the hydrological processes in the Huaihe basin. The AHMS can appropriately simulate the atmospheric and the hydrological processes at catchment scale, and their interaction.

Zusammenfassung

Zur Simulation des vollständigen regionalen Wasserkreislaufs und der hydrologischen Reaktion auf Klimaänderungen auf der Skala von Wassereinzugsgebieten werden hydro-meteorologische Modelle benötigt, die die relevanten Prozesse der Atmosphäre, an der Landoberfläche und des Erdbodens, sowie ihre Wechselwirkungen darstellen. In dieser Arbeit wird ein gekoppeltes atmosphärisches und hydrologisches Modellierungssystem (AHMS) entwickelt, das die beidseitigen Wechselwirkungen zwischen dem hydrologischen Modell HMS und dem regionalen Atmosphärenmodell WRF über das Landoberflächenmodell Noah-MP LSM realisiert. Das vollständig gekoppelte System erlaubt die explizite Beschreibung der hydrologischen Prozesse auf Skalen von Wassereinzugsgebieten bis zu Kontinenten. Das Einzugsgebiet des Huaihe in China dient als Fallstudie.

Eine neue Parametrisierung für den Überlandabfluss wird mit Berücksichtigung der Auswirkungen der Hangverteilung auf die Infiltrationskapazität entwickelt. Diese neue Parametrisierung wird zunächst in dem Modell NoahMP-HMS angewendet, welches "offline" mit meteorologischen Bodendaten angetrieben wird. Die "offline" Simulationen mit und ohne die neue Parametrisierung werden mit Beobachtungsdaten verglichen. Dabei zeigt sich, dass die neue Parametrisierung die Generierung von Überlandabfluss deutlich erhöht. Durch diese überarbeitete Abschätzung des Überlandabflusses kann das Modell NoahMP-HMS die hydrologischen Prozesse im Einzugsgebiet des Huaihe und die Wasserbilanz auf regionaler Skala mit hoher Präzision reproduzieren. Dies zeigt sich für den simulierten täglichen Abfluss des Flusses Huaihe zwischen 1980 und 1987 für drei hydrologische Messstationen am Hauptfluss anhand des Nash-Sutcliffe Effizienzköffizienten (NSIs) von 0,67, 0,81 und 0,80, und die Wasserbilanzindizes (WBIs) nahe 1,0.

Die raumzeitliche Variabilität der hydrologischen Prozesse im Einzugsgebiet wird mit einer NoahMP-HMS Simulation für den Zeitraum von 1979 bis 2003 untersucht. Auf Monatsskala besteht ein linearer Zusammenhang zwischen der im Boden gespeicherten Wassermenge im Aquifer und der Nettoniederschlagsmenge. Aufgrund der hohen Nettoniederschlagsmenge von Juni bis August steigt der Grundwasserspiegel ab Juni und erreicht sein Maximum im September. Im Untersuchungsgebiet liegt in den Gebirgsregionen tiefes Grundwasser vor, während es im Vorgebirge und im Flachland relativ hoch ist. Der monatliche Oberflächenabfluss wird hauptsächlich durch den Monatsniederschlag bestimmt, weist jedoch eine größere zeitliche Variabilität als dieser auf. Während die Zufuhr von Grundwasser in den Fluss stetig über das ganze Jahr geschieht, unterliegt der Überlandabfluss einer klaren monatlichen

Variabilität. Des Weiteren wird aus der gleichen Menge Niederschlag im Gebirge deutlich mehr Überlandabfluss generiert als im Flachland. Dies fuehrt zu einer erhöhten Flutgefahr durch Starkniederschläge in den Gebirgsregionen.

Das AHMS mit der neuen Parametrisierung wird zur Simulation der gekoppelten Hydrologie und Atmosphäre des Huaihe Einzugsgebiet der Zeitraum von Juli bis November 1991 verwendet. Die Evaluation des AHMS mit Beobachtungsdaten zeigt, dass das Modell die atmosphärischen Variablen gut darstellt und die täglichen Flussablussmengen vernuenftig abschätzt (NSIs = 0,55, WBIs = 0,63–0,79). Im Vergleich mit der WRF-Simulation weist die AHMS-Simulation eine unterschiedliche Bodenwasserdynamik auf, wobei der Einfluss hydrologischer Prozesse mit der Grundwassertiefe zusammenhängt. In tiefgelegenen Grundwasserregionen sinkt, durch das Zusammenwirken von Gravitation und Saugwirkung ungesättigter Böden, das Wasser stärker ab als bei der WRF Simulation, wo nur der Einfluss der Gravitation eine Rolle spielt. Dies fuerht zu trockeneren Böden in den Gebirgsregionen bei der AHMS-Simulation. Dieser kapillare Feuchtefluss ist insbesondere unter trockenen Bedingungen im relativ tiefen Grundwasserbereich relevant, wo es die Bodenfeuchtigkeit wieder auffuellt. Des Weiteren kann sich absinkendes Bodenwasser über dem Grundwasserspiegel akkumulieren und lateral abfließen. Dieser Prozess ist in AHMS dargestellt, jedoch nicht in WRF. Infolgedessen simuliert AHMS im Vergleich zu WRF im flachen Grundwasserbereich (Tiefen von 0–2 m) eine deutlich größere Bodenfeuchte (26%).

Aufgrund der räumlichen Variation der Grundwassertiefe im Einzugsgebiet zeigt die gekoppelte atmosphärische und hydrologische Simulation eine große räumliche Variabilität der Bodenfeuchte auf. Entsprechend weisen die Änderungen der simulierten Evaporation und der Lufttemperatur ähnliche räumliche Muster wie die Änderungen der Bodenfeuchte auf. Im Mittel ist für den Simulationszeitraum die Bodenfeuchte um 7% und die Evaporation um 8% erhöht, sowie die Temperatur um 0,2°C verringert. Die Auswirkungen des gekoppelten Models auf den gemittelten Niederschlag im Einzugsgebiet sind unbedeutend. Es fuehrt jedoch zu einer räumlichen Neuverteilung des Niederschlags im Becken mit lokalen Änderungen von bis zu ±30%.

Insgesamt konnte in der vorliegenden Studie eine einfache aber effiziente Parametrisierung für den Hangabfluss gefunden werden. Mit dieser kann das Modell die hydrologischen Prozesse im Flusseinzugsgebiet gut erfassen. Mit dem AHMS können Atmosphäre und Hydrologie, sowie ihre Wechselwirkungen, für ein gesamtes Flusseinzugsgebiet simuliert werden.

Table of Contents

1 Introduction

The water cycle is a key agent in the climate system (Mölders and Raabe, 1997) acting from global to regional scale and linking land, atmosphere, ocean and subsurface dynamics. Over land, its major components include precipitation, evapotranspiration, ice and snowmelt, soil water in aquifers, and river runoff. Rivers and lakes store a small amount of water, but river networks enable water to be transported laterally within catchments. Globally, they provide a critical link returning water from land to ocean (Miller et al., 1994). The stored water in aquifers is a key factor that controls numerous processes and feedbacks within the climate system.

The importance of hydrological components in land surface models (LSMs) has been recognized in the one-way-coupled atmospheric-land surface-hydrological modelling. For instance, the inclusion of surface runoff and groundwater in LSMs changes sensible and latent heat fluxes at the land surface (Habets et al., 1999; Stieglitz et al., 1997; Clark and Gedney, 2008; Chen and Kumar, 2001; Niu and Yang, 2003). Whereas, the evolution of the atmospheric boundary layer is directly affected by the spatial pattern of heat fluxes from and to the land surface (Shrestha et al., 2014). Hence, the integration of surface and subsurface hydrological processes into atmospheric models can help to understand the land-atmosphere interactions, which results in a better boundary condition for hydrological simulation.

Coupled land surface-hydrological models are a common tool to investigate the impact of climate change on water resources. These models are usually driven by external meteorological forcing data, isolating the terrestrial water cycle from the climate system. In fact, climate change can affect the hydrological cycle, but the changes in the hydrologic cycle, particularly the terrestrial system, in return alters the climate at local and possibly larger scale by land-atmosphere interactions (Maxwell et al., 2011). These interactions are not only crucial for assessing renewable water resources under current conditions, but also for exploring the potential impacts of climate change on water resources and terrestrial ecosystems. Thus, a model with an ability to describe the interactions between climate change and terrestrial water cycle is required to simulate the effects of future climate change on the sustainable development of regional water resource and ecosystem.

For hydrological modelling, a major challenge is the scale inconsistency between hydrological and atmospheric processes (Hostetler, 1994). Reconciling the discordant scales of hydrological and atmospheric models can be addressed by two-way coupling the models and by improving the resolution of hydrological sub-model within the atmospheric models. Regional climate models (RCMs) provide rainfall forecasts with large spatial coverage and high temporal resolution. Benefited by the high resolution of nested domains in RCMs, some small-scale atmospheric feature, e.g. orographic precipitation, can be simulated. More importantly, the development of nested, limited-area, regional climate model allows one to capture regional and local scale features, which can also be transferred to higher resolution simulations. Since climate-induced hydrological processes are strongly associated with precipitation characteristic (Booij, 2005) (e.g. amount, intensity, duration, type, and distribution), air temperature, etc., this development is critical for hydrological modelling.

Many coupled atmospheric-hydrological models have been developed (Shrestha et al., 2014; Wagner et al., 2016; Maxwell et al., 2011; Butts et al., 2014), and their complexity differs upon the research focus and temporal scale. Coupled modelling system with high complexity, e.g. three-dimensional variably saturated surface and subsurface flow model (ParFlow), are mainly applied for small watershed and/or short-term simulation. On the contrary, low complex models were developed by incorporating one or more hydrological components, e.g. groundwater (Seuffert et al., 2002; York et al., 2002) and/or surface runoff (Habets et al., 1999; Niu et al., 2005), into climate models.

This study aims at developing a coupled atmospheric and hydrological modelling system with intermediate complexity for describing a closed water cycle on catchment-scale (and continental scale). This coupled system can be used for coupled atmospheric and hydrological simulations, the short-term or long-term forecasts of catchment-scale hydrological events, the assessment for the potential effects of climate change on the availability of water resources and the sustainable development of ecosystem, the study of the dynamic feedback mechanism between the atmosphere, land surface, and subsurface.

The objectives of this study are:

1. To improve the runoff simulation by a new parameterization of hillslope runoff;
2. To develop an intermediate complex coupled Atmospheric and Hydrological Modelling System (AHMS), by incorporating a physical-based, mesoscale hydrological model to the Weather Research Forecasting (WRF) Model;
3. To evaluate the performance of the AHMS;
4. To understand how the hydrological processes in the AHMS affect the surface fluxes, and their feedback to the atmosphere.

This thesis is divided into 6 chapters. In Chapter 2, a relevant research review and motivation are presented. In Chapter 3, the AHMS is described along with the introduction of the study area. In Chapter 4, a new parameterization for hillslope runoff is developed, in which the influence of topography on the generation of surface runoff is considered. The land surface and hydrological simulation by the NoahMP-HMS in the Huaihe basin is compared with the observation to determine the effectiveness of the new parameterization. Further, the spatiotemporal variability of the hydrological processes in the basin is analyzed based on the long-term hydrological simulations. In Chapter 5, the AHMS is used for the coupled atmospheric and hydrological simulation in the Huaihe basin. Meanwhile, the impact of this coupled simulation on surface fluxes and atmospheric variables is discussed and quantified by comparing with the stand-alone atmospheric simulation. In the last chapter, the discussion, conclusion, and outlook are given.

2 Research Review and Motivation

2.1 Climate change and hydrological response

Climate change has been widely observed over recent decades in various aspects, such as rising global mean surface temperature, large-scale atmospheric circulation variability, large regional variations in precipitation trends, increasing tropospheric water vapor, and so on. Consistent with the growth of water vapor in air, an increasing number of heavy precipitation events are observed in many land regions (Trenberth et al., 2007). Furthermore, the combination of slightly changed annual precipitation and the disproportionately large increase in intense rainfall events (e.g. Easterling et al., 2000; Klein Tank et al., 2003; Klein Tank et al., 2006; Song et al., 2015) indicates a growing frequency of no/little precipitation days (Groisman and Knight, 2008). This tendency, unfortunately, increases the risks of both drought and floods, for two reasons: (1) long-duration episodes of below-average precipitation potentially cause droughts, especially if accompanying a high temperature; (2) the infiltration-excess runoff resulted from highly concentrated rainfall in a short period and the saturation-excess runoff stemmed from long-duration rainfall are highly likely to cause floods, especially if they exceeds the storage capacity of rivers, lakes, and reservoirs. Therefore, the land surface conditions are of major importance to hydrological extreme events.

The Land surface models (LSMs) with hydrologic components, usually offline driven by meteorological forcing data, is a common way to monitor terrestrial conditions and to evaluate the effects of climate change on water resource as well as extreme hydrological events, i.e. floods and drought. For example, Arnell (2003) used a macro-scale hydrological model to simulate global runoff under current and future climate conditions. The results suggest that the change of runoff pattern is largely determined by precipitation variations and evaporation offsets. Their consequent effects for global and regional water resources show that for some regions, especially in southern and eastern Asia, the increase of runoff during wet seasons may not provide more usable water resource (Arnell, 2004).

It is acknowledged that climate change may raise the risk of hydrological extremes and the pressure of regional water resource (Lehner et al., 2006). Also, some researchers (e.g. Yu et al., 2002; Yang et al., 2012; Xu et al., 2013) detected signs in some regions that runoff increases during high-flow periods and runoff decreases during low-flow periods. This change tendency of runoff in rainfall-dominated regions is generally caused by enhanced inter-seasonal variability of precipitation; while in rainfall-snowmelt or snowmelt-dominated regimes, it is resulted from surface warming primarily. For example, it has been confirmed that winter discharges increase as a result of increased precipitation and intensified snowmelt in winter for some sub-catchments of the Rhine basin, and summer discharges decrease due to reduced snow storage aggregated in winter and an increase of evapotranspiration by detailed hydrological simulation (Middelkoop et al., 2001). These hydrological changes induced by climate variability, especially the variation in precipitation characteristic – including amount, frequency, intensity, duration, and type – and increasing temperature, could increase the risks of floods (Booij, 2005) and droughts (Calanca, 2007; Strzepek et al., 2010), and also change local water resources (Guo et al., 2002), impacting further on domestic use, industry, agriculture as well as inland navigation, water quality and ecology.

2.2 Representation of hydrological components in LSMs

The main function of LSMs is to partition incoming radiation into latent and sensible heat flux, ground heat flux and snowmelt energy, as well as to separate precipitation to evapotranspiration, runoff, and infiltration. The land surface parameterization scheme was first developed in the 1960s, i.e. a leaky-bucket parameterization (Manabe et al., 1965), to represent land surface processes as the lower boundary condition of the atmosphere. Since then, the importance of land surface representation in atmospheric models on time scale ranging from days to centuries has been increasingly recognized. Thereafter, LSMs have considerably advanced by the incorporation of various physical processes, such as soil hydrology, vegetation growth, evapotranspiration, snow sublimation and melt, etc. Meanwhile, some hydrological components, e.g. surface runoff and groundwater, were described in LSMs to more realistically represent terrestrial water balance.

2.2.1 Surface runoff

The LSMs in global and regional climate modelling generally prognoses the average soil moisture for each grid cell by computing water fluxes, such as runoff and infiltration rate. This one-dimensional vertical treatment neglects soil moisture heterogeneity within one grid cell. This deficiency deserves serious attention, because the heterogeneity issues concerning soil moisture and resulting runoff generation strongly influence the heat and water budgets at the land surface (Warrach et al., 2002). Fortunately, researchers have attempted to consider the subgrid variability in soil moisture prognostication and runoff production. In the following, several frequently used approaches are elaborated in detail, as well as their integration in LSMs.

The variable infiltration capacity (VIC) model is a large-scale, semi-distributed hydrologic model in which the direct runoff (surface runoff) is calculated based on the concept of the Xinanjiang model (Zhao, 1992). Different from the definition in soil physics, the infiltration capacity in the VIC model is defined as the total volumetric capacity of a soil column to store water. The VIC model (Liang et al., 1994, 1996) includes a parameterization of the variability of infiltration storage capacity to represent the subgrid variability of topography, soil type, and vegetation. It allows the generation of surface runoff before the land surface is entirely saturated.

Habets et al. (1999a) employed the VIC model-based runoff formulation in the coupled macroscale ISBA (Interaction between the Soil, the Biosphere and the Atmosphere) and MODCOU (a hydrological model). First, this coupled model was test in the Hydrologic Atmospheric Pilot Experiment area (Habets et al., 1999b). It has been turned out that this coupled model properly simulated daily streamflow in this region. Subsequently, this model was applied to the Rhone River basin with a drainage area of 86496km^2 (Habets et al., 1999c); this simulation illustrated that the aggregation method concerning the subgrid scale variability led to annual estimation of evaporation and runoff closer to that in their reference high-resolution run.

TOPMODEL (a TOPography based hydrological MODEL), a conceptual rainfall-runoff model developed by Beven and Kirkby (1979), was used to simulate catchment-scale hydrological processes. The model combines the distributed effects of channel network topography and dynamic contributing areas within basin to emphasize the topographic control over the saturated fraction of a watershed and surface and subsurface runoff production. With this hint, Famiglietti and Wood (1994) utilized the catchment-scale TOPMODEL approach to present the horizontally heterogeneous runoff and energy balance processes in LSMs. Following his approach, Stieglitz et al. (1997) incorporated an analytic form of TOPMODEL equation into one-dimensional soil column frame in LSMs. It can be easily applied at large spatial scale because this approach only needs the statistics of topography, rather than the higher-resolution topography itself. This analytical TOPMODEL method that uses a three-parameter gamma distribution function was more widely used to represent the discrete distribution of topographic index (Stieglitz et al., 1997; Chen and Kumar, 2001; Niu and Yang, 2003).

In the soil-vegetation-atmosphere transfer (SVAT) model, Warrach et al. (2002) taken the subgrid variability of soil moisture into account by incorporating the VIC model-based runoff formulation and the TOPMODEL approach. Moreover, this SVAL model was applied to the Sleeper River watershed (111 km2), and the result shows a significant improvement in the daily runoff simulation from January 1970 to September 1974.

Niu et al. (2005) have proposed a simple TOPMODEL-based runoff parameterization

(SIMTOP) with two main modifications: (1) SIMTOP uses an exponential function instead of a three-parameter gamma distribution function to represent the discrete distribution of topographic index, improving the saturated fraction, especially in mountainous regions. (2) The subsurface runoff is reproduced by an exponential function of water table depth and a single coefficient for maximum subsurface runoff, which facilitates its application on global scale. This SIMTOP is used to take replace of baseline runoff scheme in Community Land Model version 2.0 (CLM 2.0) and its subsequent updates. It has been confirmed that the SIMTOP performed better than the baseline runoff scheme.

According to the descriptions above, the presented surface runoff generation schemes concern an assumption that a grid cell can be partly saturated, thereby generating saturated-excess runoff to participate in overland routing. It refers to the subgrid variability of soil moisture which is mainly controlled by topography. This soil moisture heterogeneity exists within a watershed at almost any scale (Stieglitz et al., 1997), which allows wide application of VIC and TOPMODEL at regional scales. The subgrid runoff parameterization in LSMs has been proved to considerably impact on the timing and intensity of river discharge as well as surface fluxes (Clark and Gedney, 2008; Chen and Kumar, 2001; Niu and Yang, 2003).

2.2.2 Groundwater

LSMs cannot be expected to reproduce water budget correctly if they do not involve the significant hydrologic components, as the parameterization schemes are developed based on water balance (Yeh et al., 2005a). In early LSMs, the flux at the bottom of soil hydrological model domain is simply parameterized as a constant or as a function of overlying moisture gradient, but without any consideration of groundwater in aquifers. In 1960s, however, the regional groundwater flow has been found to account for the loss through the vadose zone (Toth, 1962). And the interactions of land surface, vadose zone, and groundwater affects the prediction of storm runoff, evapotranspiration, water table fluctuation (Levine and Salvuccci, 1999). Thereafter, researchers have been trying to incorporate the unconfined aquifers into LSMs, often by the inclusion of the lateral groundwater distribution and the interactive flux between water table and the vadose zone.

A two-way coupling of the mesoscale weather prediction model (Lokal Modell (LM), German Weather Service) with the land surface hydrologic model ‘TOPMODEL’-Based Land Surface-Atmosphere Transfer Scheme (TOPLATS, Princeton University) was carried out by Seuffert et al. (2002). In TOPLATS, the subsurface flow from the aquifers is parameterized as a value that depends on the catchment mean water-table depth (Beven and Kirkby, 1979). The simulation results demonstrate that the lateral soil water transport between neighboring soil columns is important for weather prediction, as horizontally redistributed soil moisture can affect evaporation and precipitation.

To study aquifer-atmosphere interaction on decadal timescales, York et al. (2002) developed a coupled aquifer-land surface-atmosphere model where the USGS groundwater model MODFLOW (McDonald et al., 1988) was integrated into the atmospheric model. The simulation shows that about 5% (wet year) to 20% (dry year) of annual evapotranspiration is drawn from aquifers, and the evapotranspiration is found to be highest in cells located in topographic depressions where the water table is in the root zone.

The lumped and statistical-dynamics based models that describes the water balance in unconfined aquifers are interactively coupled to Land Surface Transfer Scheme (LSX) of NCAR (Pollard and Thompson, 1995). Based on the dataset of large-scale water table and streamflow in Illinois from 1984 to 1994, a regression equation was proposed to estimate groundwater discharge for reasonably simulating water table, soil saturation, runoff, evaporation, etc. (Yeh and Eltahir, 2005a). However, some certain disagreements still occurred, probably stemming from the spatial variability of water table depth. Hence, a statistical-dynamics method was used to describe the subgrid variability of water table depth (WTD) in the grid-scale groundwater runoff (Yeh and Eltahir, 2005b). In this approach, the dynamic probability distribution function (PDF) of WTD is specified as a two-parameter gamma distribution that is derived from the observation, which results in well-matched simulations in the test of Illinois.

Maxwell et al. (2005) replaced the soil moisture computation in CLM (Common Land Model (Dai et al., 2003)) by a mixed formulation of Richards equation in a variably saturated groundwater model (ParFlow; Ashby and Falgout, 1996). This combined model (CLM.PF) is a physically based and dynamically coupled land surface groundwater model. The study shows that CLM.PF performs more realistically in the simulation of runoff and soil moisture than the uncoupled CLM, although two models behave similarly for evapotranspiration prediction.

There are more studies (e.g. Maxwell et al., 2008; Tian et al., 2012) to investigate surface heat and water fluxes under water table dynamics. These researches have confirmed two general findings: (1) The saturated soil in aquifers, interacting with unsaturated soil through soil drainage and capillary flux, changes the local water supply to the atmosphere; (2) Laterally transported subsurface runoff redistributes the groundwater in aquifers and changes the spatial pattern of soil moisture. These two processes impact on soil moisture and surface energy and water balance, which consequently alters the atmospheric boundary layer and possibly the precipitation development. Briefly, the groundwater as an essential storage of water resource and its redistribution play an important role in climate modelling as well as weather forecasting.

2.3 Atmosphere-Land Surface-Hydrology coupling

The implementation strategies for linking atmospheric and hydrological models can be classified into two categories: an integrated modelling approach and a coupled one. The integrated approach is a method of coupling that specific models are combined directly using some subroutines in the codes. Using this method, some atmosphere-land surface-hydrology systems, e.g. PF.WRF (Maxwell et al., 2011), were successfully developed. The simplified flowchart of PF.WRF is shown in Fig. 2-1. The land surface model Noah LSM provides an interface for the combination of the subsurface hydrological model (ParFlow) and the atmospheric model (WRF), communicating surface energy and moisture fluxes between ParFlow and WRF. Wherein, ParFlow entirely replaces the surface soil moisture simulation in the Noah LSM by its incorporation as a subroutine. With the integrated ParFlow, PR.WRF can describe three-dimensional subsurface water flow and two-dimensional shallow overland flow.

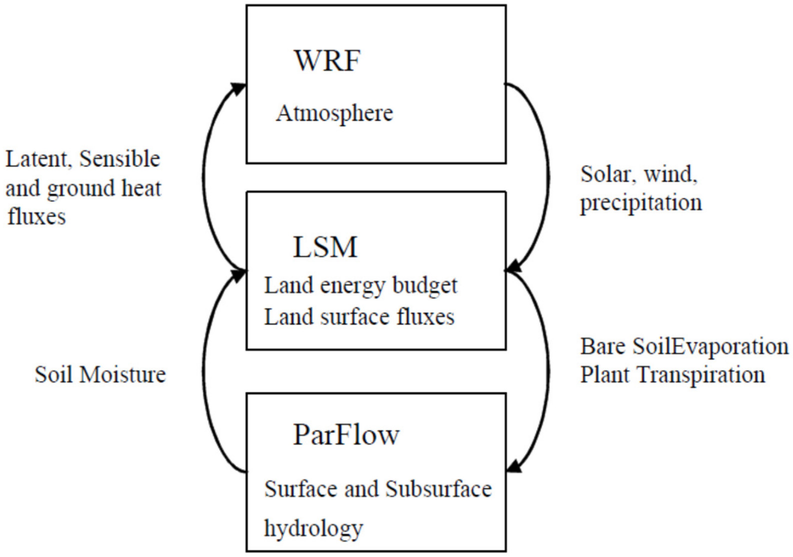

Fig. 2-1 Simplified flowchart of PF.WRF, including WRF, Noah LSM, and ParFlow. [Adopted from Maxwell (2011), Figure 1]

The coupled approach involves the coupling of two independent models via an external coupler. For example, Shrestha et al. (2014) developed a highly modular and scale-consistent terrestrial systems modelling platform (TerrSysMP, see in Fig. 2-2) that consists of COSMO, CLM, ParFlow, and an OASIS3 coupler. This OASIS3 coupler uses a technique based on the message passing interface standards MP1/MP2 and the Project for the Integrated Earth System Modeling (PRISM) for the parallel communication of two-dimensional arrays between the main process (OASIS3) and the participating component models (more details in Valcke, 2013). The configuration file of OASIS3 enables itself to determine the sequence and frequency of coupling, coupling fields and their spatial grid as well as the transformation for 2D coupled fields. Accordingly, the sending and receiving between the component models can be done sequentially.

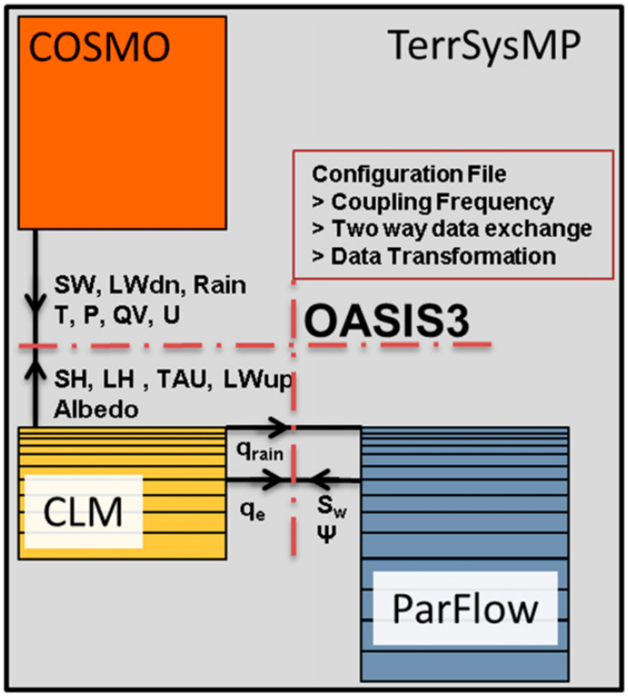

Fig. 2-2 Schematic diagram of TerrSysMP. OASIS3 provides the interfaces for the coupling of the atmospheric model (COSMO), the land surface model (CLM), and the subsurface model (ParFlow). [Adopted from Shrestha (2014), Figure 1]

The scientists use these approaches to build atmospheric-land surface-hydrological modelling systems. For instance, Maxwell et al. (2011) developed a coupled hydrological-atmospheric model PF.WRF, a combination of the Weather Research and Forecasting (WRF) Model and a parallel hydrology model (ParFlow). Based on PF.WRF, an idealized simulation (with a 3D domain size of 15 km × 15 km × 14.462 km) was run for 48 hours at 5s resolution, and a series of semi-idealized simulations were performed for the Little Washita watershed in Oklahoma (with a 45×32 km^2 domain). The idealized simulations illustrate that more precise runoff mechanism and lateral water flows change the spatial pattern of land surface fluxes.

Shrestha et al. (2014) presented a highly modular and scale-consistent terrestrial systems modeling platform (TerrSysMP), which consists of an atmospheric model COSMO, a land surface model CLM3.5, and a 3D variably saturated groundwater flow model ParFlow. Using this TerrSysMP, they performed a short-time real data simulation for the Rur catchment in Germany (150 km × 150 km, from July 21 to 27, 2012). The results show that the integrated 3D ParFlow model slightly improves the prediction of land-atmosphere exchange fluxes and is strongly sensitive to initial soil moisture content.

Gochis et al. (2015) provided a WRF-hydro model coupling extension package by including channel routing models and groundwater models in the atmospheric model WRF. The WRF-hydro is designed to simulate land surface hydrology, energy states and fluxes at a high spatial resolution (typically 1 km or less). Butts et al. (2014) developed a dynamically coupled climate-hydrological modeling system based on a regional climate modeling system HIRHAM and a comprehensive hydrological modelling system MIKE SHE. The coupled system was applied to a managed groundwater-dominated catchment, the Skjern River catchment in Denmark, for the continuous simulations from May 1, 2009 to April 30, 2010 (12 months). The small difference in net precipitation and runoff is found in the catchment during this single hydrological year.

Overall, recent research efforts have focused on coupling of distinct models, such as WRF-ParFlow (Maxwell et al., 2011), ARPS-ParFlow (Maxwell et al., 2007), COSMO-ParFlow (Shrestha et al., 2014), WRF-HMS (Wagner et al., 2016), WRF-hydro (Gochis et al., 2015).

2.4 Issues on the surface runoff production

The distributed hydrological model system HMS was firstly developed by Yu et al. (2006) for mesoscale and large-scale hydrological simulations. Based on it, Yang et al. (2010) obtained a coupled land surface-hydrological model system (CLHMS) and used this CLHMS to simulate monthly hydrological processes in the Huaihe basin of China (Yang et al., 2012). Furthermore, Li et al. (2014) modified the CLHMS by considering the spatial inhomogeneity of hydrological parameters and incorporating a subgrid direct surface runoff scheme to improve the ability of the CLHMS to predict daily mean river discharge.

For representing the spatial variability of hydrological parameters, Li et al. (2015) calibrated the Manning roughness coefficient and the hydraulic conductance of stream-aquifer interconnection in subbasins using the topographical and hydrogeological characteristics. These calibrated parameters in the subbasins form a new parameter database; their specific values are listed in Table 2.1. Meanwhile, the default parameter values in the model are defined as an old parameter database (see in Table 2.1).

Table 2.1 Old and new parameter databases of the Manning roughness coefficient and the hydraulic conductance in the Huaihe basin. [Adapted from Table 2 and Table 4 of Li et al. (2015)]

	the old parameter database		the new parameter database	
	roughness coefficient	hydraulic conductance	roughness coefficient	hydraulic conductance
WJB subbasin	0.02	10^{-5}	0.01	10^{-8}
WJB-LTZ subbasin	0.02	10^{-5}	0.02	10^{-6}
LTZ-BB subbasin	0.02	10^{-5}	0.02	10^{-5}
downstream area	0.02	10^{-5}	0.02	10^{-3}

Note: Wangjiaba (WJB), Lutaizi (LTZ), and Bengbu (BB) are three important hydrological monitoring stations in the Huai River. The drainage area above the Wangjiaba station is viewed as the upstream area of the Huai River.

With different parameter databases in Table 2.1, CLHMS was used to simulate the hydrological processes from 1980 to 1987 in the Huaihe basin. The accuracy of streamflow estimates is evaluated by the water balance index (WBI), Pearson product-moment correlation coefficient (PMC), Nash-Sutcliffe coefficient of efficiency index (NSI), index of agreement (IOA), and normalized root-mean-square error (NRSE). Their calculation formulas are listed in Appendix 7.2. The evaluation indexes of simulated daily streamflow in two simulations are shown in Table 2.2. The comparison shows that the parameter database with the consideration of spatial inhomogeneity improves the simulation accuracy of CLHMS for daily mean streamflow. But the CLHMS still has a limited ability to reconstruct the hydrological processes in the upstream area with complex topography, e.g. in the Wangjiaba subbasin.

Table 2.2 Evaluation of daily simulated streamflow by the CLHMS using old and new parameter database. [Adapted from Table 5 of Li et al. (2015)]

Station	CLHMS with the old parameter database					CLHMS with the new parameter database				
	WBI	PMC	NSI	IOA	NRSE	WBI	PMC	NSI	IOA	NRSE
WJB	1.81	0.68	0.24	0.79	-0.92	1.74	0.70	0.29	0.81	-0.75
LTZ	1.78	0.90	0.30	0.88	-0.25	1.65	0.93	0.46	0.91	-0.07
BB	1.68	0.92	0.44	0.90	-0.06	1.59	0.94	0.60	0.93	0.02

Also, the mean river discharge at the Wangjiaba station in 1980 and the contributing ratios of different component runoff were computed based on the simulations. The calculation results are presented in Table 2.3.

Table 2.3 Simulated annual mean streamflow at the Wangjiaba station in 1980, and annual mean amount of various component runoffs as well as their ratios to annual mean streamflow. [Adapted from Table 6 of Li et al. (2015)]

	CLHMS with old parameter database		CLHMS with new parameter database	
	annual mean water flow (m^3/s)	contributing ratio (%)	annual mean water flow (m^3/s)	contributing ratio (%)
outflowing streamflow	496		478	
surface runoff	143	28.8	198	41.4
groundwater supply	305	61.5	237	49.6
net precipitation	21	4.1	19	4.0

More surface runoff and less underground water flow are simulated by the CLHMS with the new parameter database. The contributing proportion of surface runoff to river discharge increases from 28.8% to 41.4%, while the contribution of groundwater supply decreases from 61.5% to 49.6%. However, it still mismatches with the fact that rainwater is the main recharge of rivers in the Huaihe basin. The river discharge in the southern region of the Huai River is composed by rainwater (accounting for 70–80%) and groundwater supply. In the northern region of the Huai River, rainwater also dominates in the river runoff, although with slightly larger contribution of groundwater supply (Huang, 1992). Hence, Li at al. (2015) believed that the influence of topographic slope on surface runoff should be better represented to improve the ability of the CLHMS.

2.5 Motivation

The water balance cannot be reproduced correctly if LSMs do not involve significant hydrological components, as the parameterization schemes in LSMs are developed based on water balance (Yeh et al., 2005a). To reasonably describe the generation of surface runoff, the VIC model-based runoff formulation and TOPMODEL-based runoff calculation are often used. But these two approaches use empirical or statistical methods to depict the distribution of catchment responses, rather than representing explicitly hillslope runoff processes. With the recognition of the importance of groundwater and its redistribution, the embedment of groundwater and its lateral transport between grid cells are widely implemented. For computationally efficient modelling at regional and global scale, only the hydrological components such as surface runoff and groundwater are described in these low complex models, instead of explicitly tracking surface and subsurface flows.

Recently, some researchers have attempted to incorporate the complete surface and subsurface hydrological processes into the atmospheric models. The three-dimensional variably-saturated subsurface and surface flow model ParFlow is popularly used to describe hydrological processes in the atmospheric models, e.g. ARPS-ParFlow, WRF-ParFlow, COSMO-Noah-ParFlow. Given the computational demands of ParFlow, these high complexity models are more often used for short-term simulations in small watersheds or idealized simulations. Another often used hydrometeorological model is WRF-hydro (Gochis et al., 2015). The WRF-Hydro is designed to enable improved simulation of land surface hydrology and energy states and fluxes at a fairly high spatial resolution (typically 1 km or less) using a variety of physics-based and conceptual approaches.

Hence, a coupled atmospheric and hydrological modelling system with intermediate complexity is required to bridge the gap between the low and high complex coupled models. In this study, a physical-based, mesoscale hydrological model will be two-way coupled with the regional atmospheric model WRF. Furthermore, the influence of slope topography on runoff generation is required to be described in the hydrological model to improve its ability of simulating hydrological processes.

3 Model Description and Study Area Description

The Weather Research and Forecasting (WRF) Model with the Advanced Research WRF dynamic solver solution is used for atmospheric simulations. In which, Land Surface Models (LSMs) predicts heat and moisture fluxes at the land surface as the lower boundary of the atmosphere; the Noah-Multiparameterization Land Surface Model (Noah-MP LSM) is employed in this study. Meanwhile, the mesoscale distributed hydrological model has been improved and used. In this chapter, the coupling of WRF, Noah-MP LSM, and HMS forms a coupled Atmospheric and Hydrological Modelling System (AHMS). The mathematical descriptions of the hydrological physical processes involved in the AHMS and their numerical solutions are exhibited. Lastly, a brief introduction for the Huaihe basin of China is given.

3.1 Model Structure

In the coupled Atmospheric and Hydrological Modelling System (AHMS), a physical-based, spatially distributed hydrological model HMS is integrated into the dynamic regional atmospheric model WRF (version 3.7, Skamarock et al., 2008) via the land surface model Noah-MP LSM by two-way coupling. The schematic diagram of the AHMS is shown in Fig. 3-1.

The WRF model is a non-hydrostatic, mesoscale numerical weather prediction, and atmospheric simulation system. It offers multiple physics options to parameterize subgrid-scale physical processes, e.g. convection, microphysics, radiation, or the planetary boundary layer. The surface atmospheric conditions prognosticated by the WRF, including precipitation, radiation, pressure, wind, etc., are used to drive the Noah-MP LSM. The standard Noah-MP LSM is a four-layer soil temperature and moisture model with canopy moisture and snow cover prediction, describing the interactions of the atmospheric boundary layer, the vegetation, and the soil. The thicknesses of soil layers are 0.1 m, 0.3 m, 0.6 m, and 1.0 m in order.

In the AHMS (as illustrated in Fig. 3-1), the hydrological model has been linked to the Noah-MP LSM, where the hydrological modules can be activated by surface fluxes. In a fully coupled mode, the two-dimensional groundwater model (GW2D) and the two-dimensional terrestrial hydrological model (RT2D) are used to simulate groundwater and terrestrial hydrological processes, respectively, as well as their interaction (GCI).

In turn, the change of hydrological conditions such as water level in lakes and rivers and groundwater table affects soil moisture and surface fluxes, and further feedbacks to atmospheric processes.

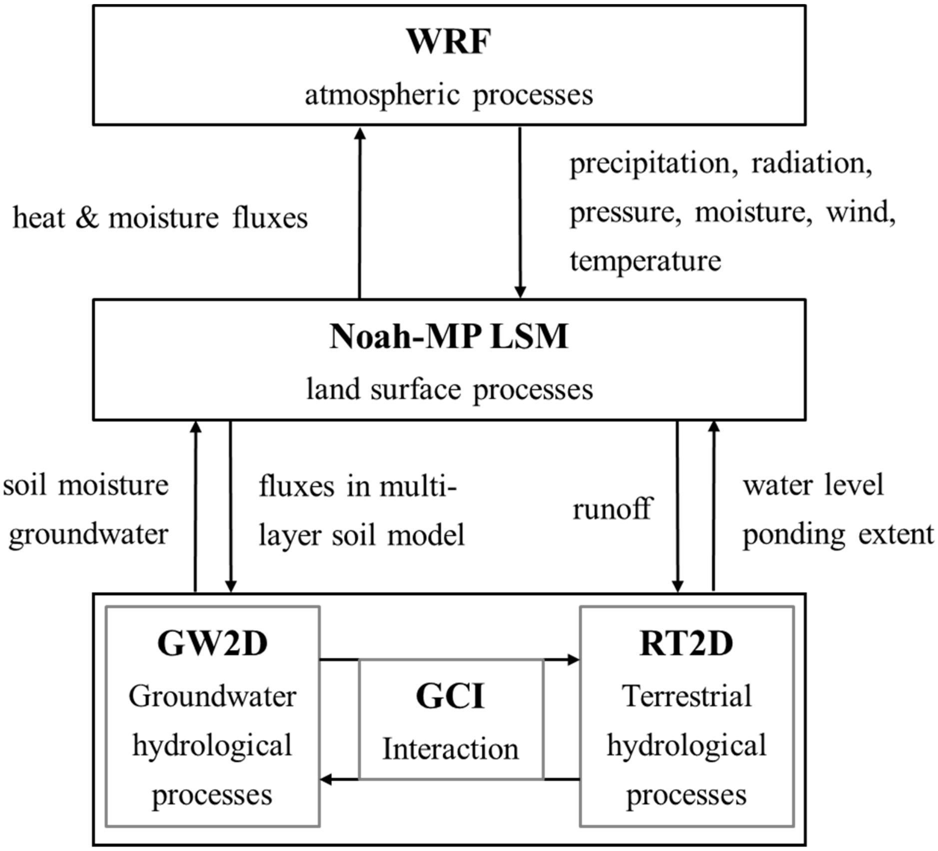

Fig. 3-1 Schematic diagram of the coupled Atmospheric and Hydrological Modelling System (AHMS). WRF: Weather Research and Forecasting Model with the Advanced Research WRF dynamics solver solution, Noah-MP LSM: Noah-Multiparameterization Land Surface Model, GW2D: two-dimensional groundwater model, RT2D: two-dimensional terrestrial hydrological model, GCI: interaction of groundwater and channel water.

The schematic diagram of the terrestrial water cycle in the AHMS is shown in Fig. 3-2, which highlights a full description of the hydrological processes at the land surface and in the subsurface. In addition to the water fluxes at the land surface (evaporation, infiltration, runoff, and so on) and the dynamics of surface soil water, the AHMS enables to simulate the interaction between unsaturated soil water and groundwater, lateral groundwater flows, terrestrial runoff routing, and the exchange of stream water and groundwater. The infiltration and the infiltration-excess runoff (i.e. Horton runoff) can be determined according to the precipitation rate at the land surface and its infiltration capacity, as formulated in Section 3.2. The four-layer soil model (with a soil layer thickness of 0.1, 0.3, 0.6, 1.0 m) in the Noah-MP LSM is used to predict the dynamics of the soil moisture in the surface soil layer (first two meters), as elaborated in Section 3.3. The lateral groundwater movement and the terrestrial hydrological processes are described by two-dimensional groundwater model (see in Section 3.4) and two-dimensional surface water routing model (Section 3.6), respectively. The interactive flux between groundwater and stream water is calculated as in Section 3.5. As elaborated in Section 3.7, the interaction of unsaturated soil water and groundwater, the redistribution of unsaturated soil water in the vadose zone, the dynamics of groundwater table, and the calculation of the saturation-excess runoff (i.e. Dunne runoff) are expressed.

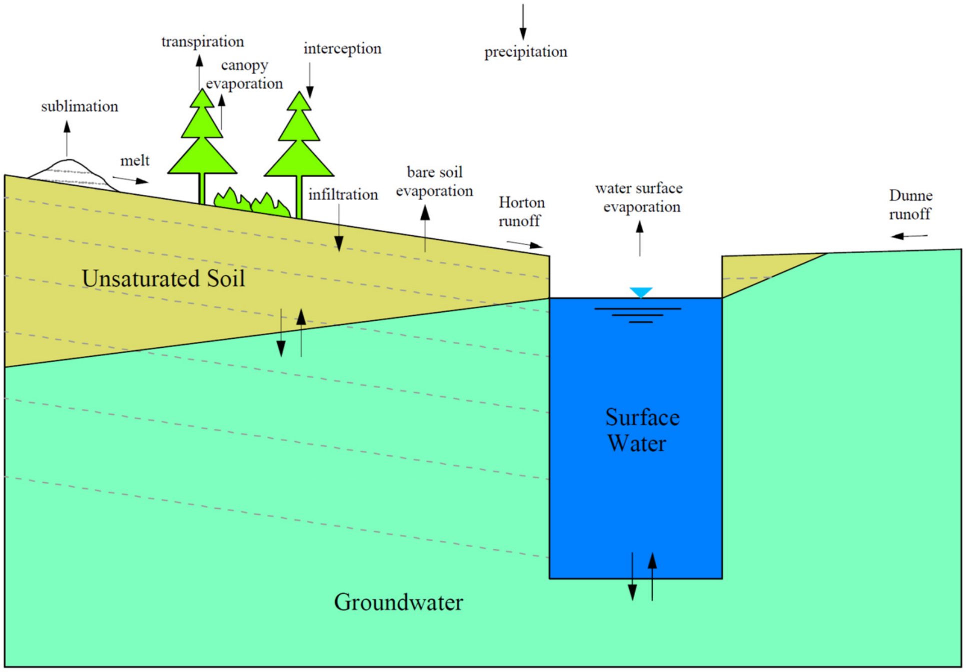

Fig. 3-2 Schematic diagram of the terrestrial water cycle in the AHMS.

3.2 Infiltration and surface runoff scheme

3.2.1 Simplified infiltration scheme

Infiltration is a process occurring at the interface the atmosphere and the ground surface, normally quantified as the rate at which soil can absorb rainfall or irrigation, i.e. infiltration rate. The actual infiltration is determined by different boundary conditions (see in Eq. 3-1): (1) rainfall intensity is less than the capacity of soil to transmit water (infiltration capacity), in which case the infiltration rate is governed by water supply

(supply controlled); (2) precipitation rate exceeds infiltration capacity, thus the infiltration rate is limited by the infiltration capacity of the near-surface soil (surface controlled).

$$I = \begin{cases} p & p \le f^* \\ f^* & p > f^* \end{cases} \qquad 3\text{-}1$$

where I is the actual infiltration rate [m/s], p is the precipitation rate at the soil surface [m/s], f^* is the infiltration capacity [m/s].

Darcy's law is one of the methods to calculate infiltration; Eq. 3-6 shows its calculation formula in detail. In the case of adequate rainfall/irrigation, the near-surface soil is assumed to be wet enough and approach its maximum soil moisture (θ_{max}), and hence the gradient of matric potential can be neglected (i.e. $\frac{\partial \varphi_m}{\partial z} \approx 0$). Consequently, the one-dimensional vertical Darcy's law can be simplified as $f^* = K(\theta_{max})$. In this study, the Clapp and Hornberger model (Clapp and Hornberger, 1978) is used to estimate the hydraulic conductivity at one certain soil moisture (see Eq. 3-8). This maximum infiltration rate is normally called infiltration capacity.

Given enough water rainfall/irrigation to a horizontal soil grid, the near-surface soil is supposed to reach saturation, i.e. $\theta_{max} = \theta_s$. Thus, the infiltration capacity is simplified as the hydraulic conductivity of the near-surface soil at the saturated soil moisture (θ_s), i.e. $f^* = K(\theta_s)$. In the infiltration scheme of the AHMS, it is expressed as the saturated hydraulic conductivity of the top-layer soil (0–10 cm).

3.2.2 Infiltration-excess runoff

In this study, the infiltration-excess runoff is jointly determined by precipitation rate and infiltration capacity. If the precipitation rate (including rainfall, snowmelt, etc.) at the soil surface exceeds the infiltration capacity, that part of precipitation beyond the infiltration capacity becomes runoff, viewed as infiltration-excess runoff; if the precipitation rate is lower than the infiltration capacity, infiltration-excess runoff does not occur. The calculation of infiltration-excess runoff can be formulated as

$$R_{ins} = \begin{cases} 0 & p \le f^* \\ p - f^* & p > f^* \end{cases} \qquad 3\text{-}2$$

where R_{ins} is the infiltration-excess runoff [m/s].

3.3 Multi-layer soil model

3.3.1 Richards equation

The prognostic equation for soil moisture is the one-dimensional Richards equation

$$\frac{\partial \theta}{\partial z} = \frac{\partial}{\partial z}\left(K\frac{\partial \varphi}{\partial z}\right) + S \qquad 3\text{-}3$$

where θ is the volumetric soil water content [m^3/m^3], K is the hydraulic conductivity [m/s], φ is the hydraulic potential [m], z is the vertical coordinate [m], S represents sources and sinks for soil water.

Eq. 3-3 is a convective-diffusive equation derived from the one-dimensional conservation equation of water mass

$$\frac{\partial \theta}{\partial t} = -\frac{\partial q}{\partial t} + S \qquad 3\text{-}4$$

with the substitution of Darcy's Law for vertical water flux

$$q = -K\frac{\partial \varphi}{\partial z} \qquad 3\text{-}5$$

The hydraulic potential in Eq. 3-5 consists of gravitational potential (φ_g) and soil matric potential (φ_m), i.e. $\varphi = \varphi_m + \varphi_g$. Assumed that the reference elevation is the soil surface with positive downwards, then, Eq. 3-5 can be written as

$$q = -K\frac{\partial\left(\varphi_m - z\right)}{\partial z} \qquad 3\text{-}6$$

and Eq. 3-3 can be transformed to

$$\frac{\partial \theta}{\partial z} = \frac{\partial}{\partial z}\left(K\frac{\partial \varphi_m}{\partial z} - K\right) + S \qquad 3\text{-}7$$

Hydraulic conductivity (K) and soil matric potential (φ_m) are highly nonlinear functions of soil moisture, whose closure relationships are essential for the solution of Richards equation. And some researchers, e.g. Brooks and Corey (1964), Clapp and Hornberger (1978), and Van Genuchten (1980), have proposed many different functions for the water retention and hydraulic conductivity curves. The Clapp and Hornberger model, often used in LSMs, is adopted in the Noah-MP LSM. In the Clapp and Hornberger model, the hydraulic conductivity is estimated as

$$K(\theta)=K_s\left(\frac{\theta}{\theta_s}\right)^{2b+3} \tag{3-8}$$

where K_s is the saturated hydraulic conductivity [m/s], θ_s is the saturated soil moisture [m^3/m^3], b is a curve-fitting parameter.

And the water retention function is

$$\varphi_m=\varphi_s\left(\frac{\theta}{\theta_s}\right)^{-b} \tag{3-9}$$

where φ_s is the air-entry matric potential [m].

Additionally, the hydraulic diffusivity is defined as

$$D(\theta)=K(\theta)\frac{\partial\varphi_m(\theta)}{\partial\theta} \tag{3-10}$$

With the expressions of the hydraulic conductivity and soil matric potential, the hydraulic diffusivity can be written as:

$$D(\theta)=-\frac{bK_s\varphi_s}{\theta_s}\left(\frac{\theta}{\theta_s}\right)^{b+2} \tag{3-11}$$

Combining Eq. 3-7 and Eq. 3-8, 3-9, 3-11, the mass conservation-based form of Richards equation (Eq. 3-3) can be formulated in a diffusivity form:

$$\frac{\partial\theta}{\partial z}=-\frac{\partial}{\partial z}\left(D(\theta)\frac{\partial\theta}{\partial z}+K(\theta)\right)+S \tag{3-12}$$

Also, the vertical water flux is expressed as

$$q=-D(\theta)\frac{\partial\theta}{\partial z}+K(\theta) \tag{3-13}$$

The hydraulic properties in Eq. 3-12 and 3-13, including the saturated hydraulic conductivity (K_s), the soil porosity (θ_s), the saturated soil matric potential (φ_s), and the exponent parameter (b), can be determined according to the researches of Clapp and Hornberger (1978) and Cosby et al. (1984), i.e.

$$
\begin{aligned}
K_s &= 10^{-0.884+0.0153(P_{sand})} \times 0.0254/3600 \\
\theta_s &= 0.489 - 0.00126\left(P_{sand}\right) \\
\varphi_s &= -0.01 \times 10^{1.88-0.0131(P_{sand})} \\
b &= 2.91 + 1.59\left(P_{clay}\right)
\end{aligned}
\qquad 3\text{-}14
$$

where P_{sand} and P_{clay} are the percent composition of sand and clay, respectively [kg/kg].

3.3.2 Richards equation with equilibrium soil matric potential

Theoretically, the matric potential of soil in the saturated soil zone varies although soil moisture has little change (saturated). Thus, the numerical solution of the θ-based Richards equation (e.g. Eq. 3-12) only suits the simulation of the soil moisture in the unsaturated zone, not applicable for the saturated zone. Zeng and Decker (2009), therefore, have introduced a hydrostatic equilibrium soil moisture distribution to obtain the steady-state solution of Richards equation, no matter where groundwater table locates. Accordingly, Eq. 3-6 is written as

$$
q = -K \frac{\partial\left(\varphi_m - z - C\right)}{\partial z} \qquad 3\text{-}15
$$

where C is a constant hydraulic potential above the water table z_{∇} with

$$
C = \varphi_E - z = \varphi_S - z_{\nabla} \qquad 3\text{-}16
$$

So that

$$
q = -K \frac{\partial\left(\varphi_m - \varphi_E\right)}{\partial z} \qquad 3\text{-}17
$$

where φ_E is the equilibrium soil matric potential [m], which is estimated by

$$
\varphi_E = -\varphi_S \left(\frac{\theta_E\left(z\right)}{\theta_S}\right)^{-b} \qquad 3\text{-}18
$$

And the equilibrium volumetric water content $\theta_E(z)$ can also be derived as

$$
\theta_E\left(z\right) = \theta_s \left(\frac{\varphi_s + z_{\nabla} - z}{\varphi_s}\right)^{-1/b} \qquad 3\text{-}19
$$

Combining Eq. 3-4 and Eq. 3-17, one can obtain the modified Richards equation with equilibrium soil matric potential

$$\frac{\partial \theta}{\partial t} = \frac{\partial}{\partial z}\left(K \frac{\partial \left(\varphi_m - \varphi_E \right)}{\partial z} \right) + S \qquad \text{3-20}$$

3.3.3 Numerical solution

In the Noah-MP LSM, the partial differential equation for volumetric soil water content, such as Eq. 3-12, is numerically solved by a multi-layer model as shown in Fig. 3-3, with the upper boundary condition at the soil surface ($q_0 = I - e_{soil}$) and the lower boundary condition at the model domain bottom. In the AHMS, the Darcy-flux boundary condition is used to estimate the water flux (i.e. q_n in Fig. 3-3) at the bottom of the multi-layer soil model domain, as

$$\begin{cases} q_n = -D\left(\theta_n\right)\dfrac{\partial \theta}{\partial z} + K\left(\theta_n\right) \\ \dfrac{\partial \theta}{\partial z} = \dfrac{\theta_n - \theta_{n+1}}{z_n - z_{n+1}} \end{cases}$$

where θ_{n+1} is the volumetric soil water content at $z = z_{n+1}$ [$\mathrm{m}^3/\mathrm{m}^3$], and its estimation is related to the location of groundwater table, which is expressed in Eq. 3-39.

The soil water in the soil model domain interacts with deeper unsaturated soil water and/or groundwater by the bidirectional flux calculated by the Darcy-flux boundary condition. In the Noah-MP LSM, the numerical solution with an implicit method by expanding and integrating the diffusivity form of Richards equation (Eq. 3-12) over one layer is produced, as following:

$$\Delta z_i \frac{\Delta \theta_i^{t+1}}{\Delta t} = -\left(q_i^{t+1} - q_{i-1}^{t+1} \right) - e_i \qquad \text{3-21}$$

where t and $t+1$ represent current and next time step, respectively, i means soil layer, Δt is the interval of the time step.

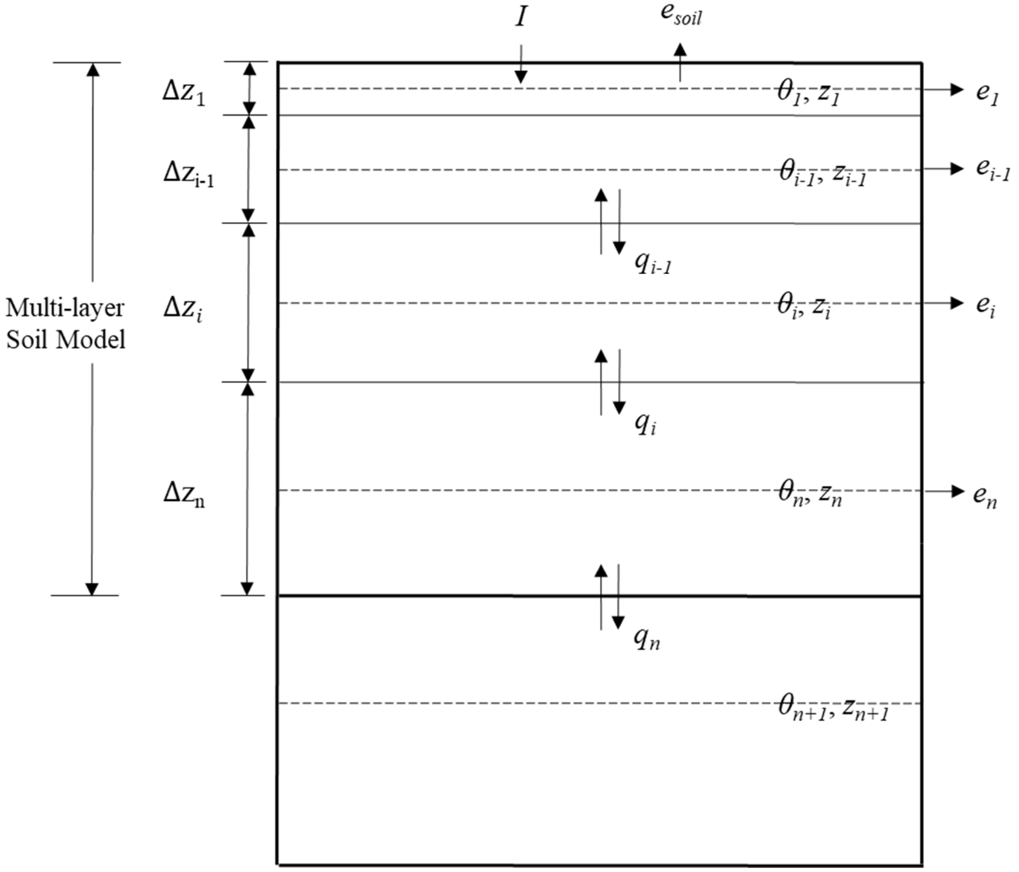

Fig. 3-3 Schematic diagram of the multi-layer soil model. *I*: infiltration at land surface; e_{soil}: soil evaporation from top layer; q_i: vertical flux crossing the bottom of soil layer *i*; e_i: transpiration from soil layer *i*; z_i: *z*-coordinate of the center of soil layer *i*; θ_i: average soil moisture in soil layer *i*; Δz_i: the thickness of soil layer *i*. And *n*: number of soil layers defined by user; *n+1*: unconfined aquifer below the multi-layer soil model domain.

By substitution and transformation, Eq. 3-21 is formulated as a tridiagonal equation:

$$\begin{cases} a_i \Delta\theta_{i-1}^{t+1} + b_i \Delta\theta_i^{t+1} + c_i \Delta\theta_{i+1}^{t+1} = r_i \\ a_i = -\dfrac{D\left(\theta_{i-1}^t\right)}{0.5\left(\Delta z_{i-1} + \Delta z_i\right)} \\ b_i = \dfrac{\Delta z_i}{\Delta t} - a_i - c_i \\ c_i = -\dfrac{D\left(\theta_i^t\right)}{0.5\left(\Delta z_i + \Delta z_{i+1}\right)} \\ r_i = q_{i-1}^t - q_i^t - e_i \end{cases} \tag{3-22}$$

With the solution of this tridiagonal equation set over soil layers, soil moisture within the soil model domain can be updated using $\theta_i^{t+1} = \theta_i^t + \Delta\theta_i^{t+1}$.

3.4 2D groundwater model

3.4.1 Boussinesq equation

The upper groundwater surface in an unconfined aquifer is called water table. The vadose zone locates above the water table, and there is a subsurface layer called a capillary fringe in which groundwater seeps up from water table by capillary action to fill pores. The saturated soil water below the water table in an unconfined aquifer is considered as the unconfined groundwater. The three-dimensional movement of the unconfined groundwater is described by the partial-differential equation (McDonald and Harbaugh, 1988) as

$$\frac{\partial}{\partial x}\left(K_x \frac{\partial H_p}{\partial x}\right) + \frac{\partial}{\partial y}\left(K_y \frac{\partial H_p}{\partial y}\right) + \frac{\partial}{\partial z}\left(K_z \frac{\partial H_p}{\partial z}\right) - W = S_s \frac{\partial H_p}{\partial t} \qquad 3\text{-}23$$

where K_x, K_y, K_z represent the saturated hydraulic conductivity in the direction of x, y, z [m/s], respectively, H_p is the potentiometric head [m], S_s is the specific storage of the porous material [m^{-1}], W is sources and sinks [s^{-1}].

Owing to the complexity of the three-dimensional model and its time-consuming computation, the groundwater simulation is divided into two steps: (1) the horizontal two-dimensional groundwater motion solved by Boussinesq equation (in this section), and (2) the description of groundwater table dynamics (see more details in Section 3.7).

With the Dupuit-Forchheimer assumption, the horizontally two-dimensional groundwater flow equation can be derived from Eq. 3-23 as

$$-\left(\frac{\partial}{\partial x}(q_x) + \frac{\partial}{\partial y}(q_y)\right) = S_s \frac{\partial H}{\partial t} \qquad 3\text{-}24$$

where q *is* the Darcy flux in a saturated condition [m/s], H is the groundwater head [m].

Darcy's law can also be expressed in terms of the transmissivity in unconfined aquifers as

$$\begin{cases} q_x = -\dfrac{T_x}{h}\dfrac{\partial H}{\partial x} \\ q_y = -\dfrac{T_y}{h}\dfrac{\partial H}{\partial y} \end{cases} \qquad 3\text{-}25$$

where T is the transmissivity [m^2/s], the rate at which groundwater flows horizontally through an aquifer, h is the thickness of the unconfined groundwater [m], i.e. the height of free water surface above the bottom of the unconfined aquifer.

Combining Eq. 3-24 and Eq. 3-25 gives

$$\frac{\partial}{\partial x}\left(T_x\frac{\partial H}{\partial x}\right)+\frac{\partial}{\partial y}\left(T_y\frac{\partial H}{\partial y}\right)=\mu\frac{\partial H}{\partial t} \qquad 3\text{-}26$$

where μ is the specific yield [m^3/m^3], also known as the drainable porosity.

This equation is usually called as Boussinesq equation, which governs the saturated flow in unconfined aquifers under the Dupuit-Forchheimer approximation.

3.4.2 Numerical solution

To numerically solve Eq. 3-26 with higher efficiency, the time-implicit Alternating Direction Implicit (ADI) method is adopted, and the specific schemes are shown as following:

Step 1: x-derivative taken explicitly, and y-derivative taken implicitly

$$\frac{T^t_{x_{i-1,j}}\left(\frac{H^t_{i-1,j}-H^{t+1/2}_{i,j}}{\Delta x}\right)-T^t_{x_{i,j}}\left(\frac{H^{t+1/2}_{i,j}-H^t_{i+1,j}}{\Delta x}\right)}{\Delta x}+$$
$$\frac{T^t_{y_{i,j-1}}\left(\frac{H^{t+1/2}_{i,j-1}-H^{t+1/2}_{i,j}}{\Delta y}\right)-T^t_{y_{i,j}}\left(\frac{H^{t+1/2}_{i,j}-H^{t+1/2}_{i,j+1}}{\Delta y}\right)}{\Delta y}=\mu_{i,j}\left(\frac{H^{t+1/2}_{i,j}+H^t_{i,j}}{\Delta t}\right)$$

which is simplified to be a tridiagonal equation set of the form as

$$\begin{cases} a_i H^{t+1/2}_{i,j-1}+b_i H^{t+1/2}_{i,j}+c_i H^{t+1/2}_{i,j+1}=r_i \\ a_i=-T^t_{y_{i,j-1}} \\ b_i=\dfrac{\mu_{i,j}\Delta x\Delta y}{\Delta t}+T^t_{x_{i-1,j}}+T^t_{x_{i,j}}+T^t_{y_{i,j-1}}+T^t_{y_{i,j}} \\ c_i=-T^t_{y_{i,j}} \\ r_i=\dfrac{\mu_{i,j}\Delta x\Delta y}{\Delta t}H^t_{i,j}+T^t_{x_{i-1,j}}H^t_{i-1,j}+T^t_{x_{i,j}}H^t_{i+1,j} \end{cases} \qquad 3\text{-}27$$

Step 2: x-derivative taken implicitly, and y-derivative taken explicitly

$$\frac{T_{x_{i-1,j}}^{t+1/2}\left(\frac{H_{i-1,j}^{t+1}-H_{i,j}^{t+1}}{\Delta x}\right)-T_{x_{i,j}}^{t+1/2}\left(\frac{H_{i,j}^{t+1}-H_{i+1,j}^{t+1}}{\Delta x}\right)}{\Delta x}+$$

$$\frac{T_{y_{i,j-1}}^{t+1/2}\left(\frac{H_{i,j-1}^{t+1/2}-H_{i,j}^{t+1}}{\Delta y}\right)-T_{y_{i,j}}^{t+1/2}\left(\frac{H_{i,j}^{t+1}-H_{i,j+1}^{t+1/2}}{\Delta x}\right)}{\Delta y}=\mu_{i,j}\left(\frac{H_{i,j}^{t+1}-H_{i,j}^{t+1/2}}{\Delta t}\right)$$

which can also be formulated as

$$\begin{cases} a_i H_{i-1,j}^{t+1}+b_i H_{i,j}^{t+1}+c_i H_{i+1,j}^{t+1}=r_i \\ a_i=-T_{x_{i-1,j}}^{t+1/2} \\ b_i=\dfrac{\mu_{i,j}\Delta x\Delta y}{\Delta t}+T_{x_{i-1,j}}^{t+1/2}+T_{x_{i,j}}^{t+1/2}+T_{y_{i,j-1}}^{t+1/2}+T_{y_{i,j}}^{t+1/2} \\ c_i=-T_{x_{i,j}}^{t+1/2} \\ r_i=\dfrac{\mu_{i,j}\Delta x\Delta y}{\Delta t}H_{i,j}^{t+1/2}+T_{x_{i,j-1}}^{t+1/2}H_{i,j-1}^{t+1/2}+T_{x_{i,j}}^{t+1/2}H_{i,j+1}^{t+1/2} \end{cases} \qquad 3\text{-}28$$

where *t* and *t+1* represent separately current and next time step, and *t+1/2* indicates half time step between *t* and *t+1*.

After solving successively the equation sets of 3-27 and 3-28, the groundwater head is then updated to be $H_{i,j}^{t+1}$.

3.5 Interaction of groundwater and channel water

Groundwater and surface water are not isolated components in the hydrological system, instead, they interact. A lot of methods, such as model construction and field measurement, have already been carried out to quantify the stream-aquifer interaction. Osman et al. (2002) pointed out that it is necessary to take the effect of the suction head beneath the streambed layer into account if one needs to calculate the stream-aquifer flux properly. Hence, the deterministic modelling method, MODFLOW (McDonald and Harbaugh, 1988), is implemented to estimate the interactive flux between streams and aquifers.

In the MODFLOW stream package (McDonald and Harbaugh, 1988), the open water in streams is assumed to be separated from the aquifer by a clogging streambed layer with low permeability (as shown in Fig. 3-4 and Fig. 3-5). The interactive flux between them is simplified as a function of streambed conductance and head gradient.

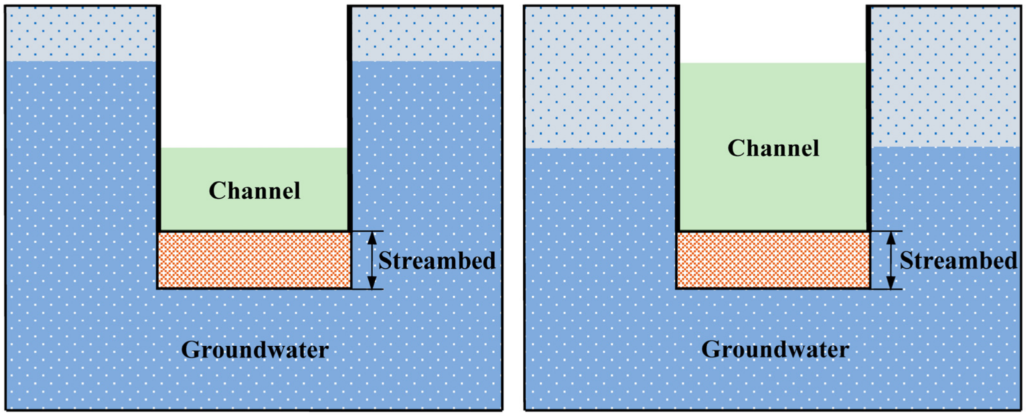

Fig. 3-4 Conceptual representation of direct stream-aquifer interconnection.

As shown in Fig. 3-4, the groundwater is directly connected with surface water, in which case flowing water between them is predominantly through a saturated medium. This interactive flux, q_{cg}, is linearly related to the difference of groundwater head and water level in streams as

$$q_{cg} = \frac{K_b}{M}\left(h_r - h_g\right) = C_s\left(h_r - h_g\right) \qquad \text{3-29}$$

where C_s is the hydraulic conductance of stream-aquifer interconnection [s^{-1}], K_b is the hydraulic conductivity of streambed material [m/s], L is the length of the stream [m], W is the width of the stream [m], M is the streambed thickness [m], h_r is the elevation of water level in the stream [m], h_g is the groundwater head [m].

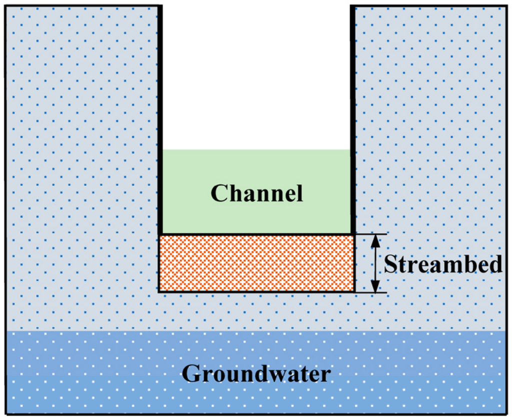

Fig. 3-5 Conceptual representation of indirect stream-aquifer interconnection.

Once the groundwater head falls below the streambed, the direct connection between groundwater and stream water disappears, as shown in Fig. 3-5. In this case, the flow from streams to groundwater is assumed proportional to the depth of water in the channel (detailed in Eq. 3-30).

$$q_{cg} = C_s \left(h_r - h_{bot} \right) \qquad 3\text{-}30$$

where h_{bot} is the elevation of the streambed [m].

McDonald and Harbaugh (1988) have pointed out that the formulation of a single conductance term to account for a three-dimensional flow process is inherently an empirical exercise, and the calibration for it is almost always required.

3.6 2D terrestrial hydrological model

3.6.1 A subgrid channel two-dimensional model

The storage cell approach was first proposed in 1970, and widely used to simulate floodplain inundation; based on this approach, the two-dimensional subgrid channel model (Neal et al., 2012) was developed where each discretized cell is viewed as one storage compartment. To present a hydraulic model for both channel flow and floodplain flow, there are two major extensions in the model: (1) a subgrid channel is given in each grid cell (as shown in Fig. 3-4 and Fig. 3-5); (2) the hydraulic characteristics of the subgrid channel (e.g. channel depth and width, see in Fig. 3-6) are estimated using the hydraulic geometry theory (Leopold and Maddock, 1953).

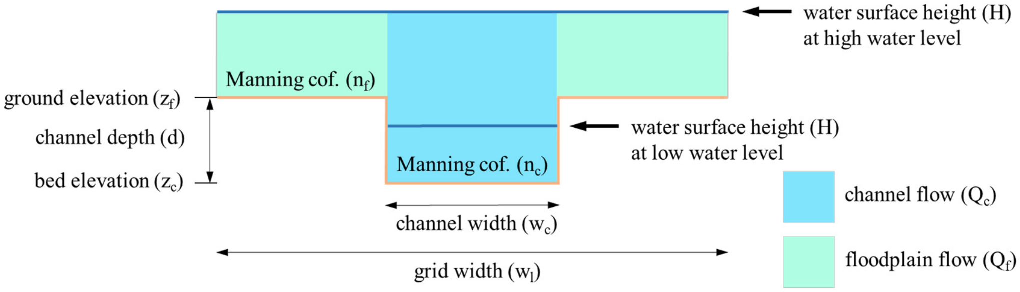

Fig. 3-6 Conceptual diagram of the subgrid cross-section (adopted from Neal et al. (2012), Figure 1)

In the subgrid channel model, the simulation of the water level, wave propagation, and inundation extent in one grid cell is implemented by combining the continuity of mass in cell and the momentum equation between cells. The continuity equation is

$$\frac{\Delta H}{\Delta t} = \frac{\Delta Q}{A} \qquad 3\text{-}31$$

And the momentum equation to calculate the flow between cells is based on Manning's equation:

$$Q = w \cdot h \cdot \frac{m}{n} \cdot R^{\frac{2}{3}} \cdot \left(\frac{dH}{dl}\right)^{1/2} \tag{3-32}$$

where H is the water free surface height [m], Q is the volumetric flow rates into or out of the cell [m^3/s], A is the water surface area [m^2], t is the time [s], h is the water depth [m], w is the width of flowing water [m], m is a constant, n is the Manning roughness coefficient [$s/(m^{1/3})$], l is the length of flowing path [m], R is the hydraulic radius [m], $J = \frac{dH}{dl}$ is the slope of the linear hydraulic head loss along the flowing path [m/m]. For wide and shallow channels, the wetter perimeter approximately equals to the channel width, and thus the hydraulic radius is represented by the depth of water flow.

In the case of low water level, i.e. water level maintains below the ground elevation (as shown in Fig. 3-6), the flow between grids in the continuity equation is supposed to compute as channel flow:

$$\begin{cases} Q_c = W_c \cdot h_c \cdot \frac{m}{n_c} \cdot \left(h_c\right)^{\frac{2}{3}} \cdot \left(\frac{dH}{dl}\right)^{1/2} \\ h_c = H - z_c \end{cases} \tag{3-33}$$

where h_c is the water depth in the channel [m], w_c is the width of the channel [m], n_c is the Manning roughness coefficient of channel flow [$s/(m^{1/3})$], z_c is the streambed elevation [m].

In the case of high water level as shown in Fig. 3-6, the channel flow can be calculated from Eq. 3-33, and the floodplain flow can be calculated from Eq. 3-34. The combination of channel flow and floodplain flow, i.e. $Q = Q_c + Q_f$, provides the cell discharge. The continuity equation (Eq. 3-31) accounts for the conservation of water mass in each grid cell; the water surface area (A) equals to $w_c \cdot \Delta x$ if water flows in the channel and $A = \Delta x^2$ if water is above the channel bank.

$$\begin{cases} Q_f = w_f \cdot h_f \cdot \frac{m}{n_f} \cdot \left(h_f\right)^{\frac{2}{3}} \cdot \left(\frac{dH}{dl}\right)^{\frac{1}{2}} \\ h_f = H - z_f \\ w_f = w_l - w_c \end{cases} \tag{3-34}$$

where w_f is the width of floodplain flow [m], h_f is the water depth of floodplain flow,

[m], w_l is the width of flowing water [m], n_f is the Manning roughness coefficient of floodplain flow [s/(m$^{1/3}$)], z_f is the ground elevation [m], Δx is the width of grid cell [m].

3.6.2 Numerical solution

In the two-dimensional terrestrial hydrological model, the equations are implicitly solved using a finite difference discretization of the time derivative term. Considering the flows in eight directions (see in Fig. 3-7) and sink/source, the continuity equation (Eq. 3-31) for each grid cell(i,j) over a time step Δt is expressed as

$$\begin{aligned}\frac{H_{i,j}^{t+1}-H_{i,j}^{t}}{\Delta t}=&\frac{\left(Q_{(i-1,j)\to(i,j)}^{t+1}+Q_{(i-1,j-1)\to(i,j)}^{t+1}+Q_{(i,j-1)\to(i,j)}^{t+1}+Q_{(i+1,j-1)\to(i,j)}^{t+1}\right)}{A_{i,j}}\\&-\frac{\left(Q_{(i,j)\to(i+1,j)}^{t+1}+Q_{(i,j)\to(i+1,j+1)}^{t+1}+Q_{(i,j)\to(i,j+1)}^{t+1}+Q_{(i,j)\to(i-1,j+1)}^{t+1}\right)}{A_{i,j}}+\frac{S_{i,j}}{A_{i,j}}\end{aligned}\tag{3-35}$$

where $S_{i,j}$ signifies the sink and source item, including the interactive flux between channel water and groundwater, infiltration-excess runoff and saturation-excess runoff.

With predefined flowing directions (k=1 - 8 in Fig. 3-7), Eq. 3-35 is shortened to

$$A_{i,j}\cdot\frac{H_{i,j}^{t+1}-H_{i,j}^{t}}{\Delta t}=\sum_{k=1}^{k=4}Q_{i,j}^{k,t+1}-\sum_{k=5}^{k=8}Q_{i,j}^{k,t+1}+S_{i,j}^{t+1}\tag{3-36}$$

The time implicit term, $Q_{i,j}^{t+1}$, is contributed by the slope item of the momentum equation (i.e. Eq. 3-32), as

$$\left|\left(\frac{dH}{dl}\right)^{t+1}\right|^{\frac{1}{2}}=\left|\left(\frac{dH}{dl}\right)^{t}\right|^{-\frac{1}{2}}\cdot\overline{\left(\frac{dH}{dl}\right)}$$

$$\overline{\left(\frac{dH}{dl}\right)}=\frac{1}{2}\left(\left(\frac{dH}{dl}\right)^{t}+\left(\frac{dH}{dl}\right)^{t+1}\right)$$

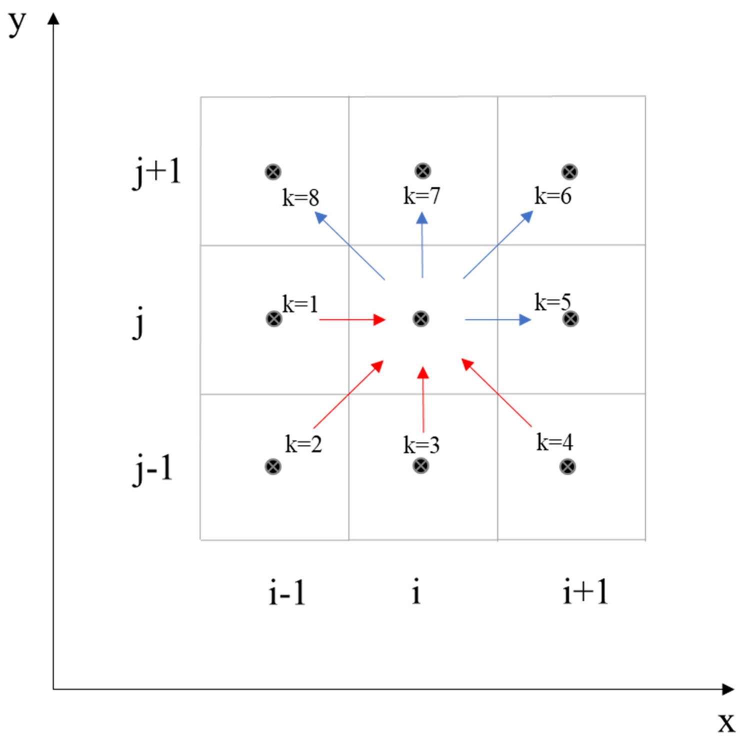

Fig. 3-7 Diagram of flow directions between one cell and its eight neighboring cells. Predefined inflowing direction (red arrows): k = 1–4, from (ik,jk) to (i,j); predefined outflowing direction (blue arrows): k = 5–8, from (i,j) to (ik,jk). For k = 1, water flows from (i-1,j) to (i,j) with $\Delta l = \Delta x$; for k = 2, (i,j-1) to (i,j) with $\Delta l = \sqrt{2\Delta x^2}$; for k = 3, (i,j-1) to (i,j) with $\Delta l = \Delta x$; for k = 4, (i+1,j-1) to (i,j) with $\Delta l = \sqrt{2\Delta x^2}$; for k = 5, (i,j) to (i+1,j) with $\Delta l = \Delta x$; for k = 6, (i,j) to (i+1,j+1) with $\Delta l = \sqrt{2\Delta x^2}$; for k = 7, (i,j) to (i,j+1) with $\Delta l = \Delta x$; for k = 8, (i,j) to (i+1,j-1) with $\Delta l = \sqrt{2\Delta x^2}$.

For the defined inflowing directions (k = 1–4 in Fig. 3-7), the slope of the linear hydraulic head loss at a grid cell (i,j) is written as

$$\left(\frac{dH}{dl}\right)_{i,j}^{k,t} = \frac{H_{ik,jk}^{t} - H_{i,j}^{t}}{\left(\Delta l\right)_{i,j}^{k}}$$

$$\overline{\left(\frac{dH}{dl}\right)_{i,j}^{k}} = \frac{H_{ik,jk}^{t} - H_{i,j}^{t}}{\left(\Delta l\right)_{i,j}^{k}} + \frac{\left(\Delta H\right)_{ik,jk}^{t+1} - \left(\Delta H\right)_{i,j}^{t+1}}{2\left(\Delta l\right)_{i,j}^{k}}$$

and for the defined outflowing directions (k = 5–8 in Fig. 3-7), the slope is expressed as

$$\left(\frac{dH}{dl}\right)_{i,j}^{k,t} = \frac{H_{i,j}^t - H_{ik,jk}^t}{(\Delta l)_{i,k}^k}$$

$$\overline{\left(\frac{dH}{dl}\right)_{i,j}^{k}} = \frac{H_{i,j}^t - H_{ik,jk}^t}{(\Delta l)_{i,j}^k} + \frac{(\Delta H)_{i,j}^{t+1} - (\Delta H)_{ik,jk}^{t+1}}{2(\Delta l)_{i,j}^k}$$

Therefore, the two-dimensional surface water routing scheme can be formulated as

$$\left(1+\frac{\Delta t}{2A_{i,j}}\cdot\sum_{k=1}^{8} f_{i,j}^k\right)\cdot(\Delta H)_{i,j}^{t+1} - \frac{\Delta t}{2A_{i,j}}\cdot\sum_{k=1}^{8}\left(f_{i,j}^k\cdot(\Delta H)_{ik,jk}^{t+1}\right) = \frac{\Delta t}{A_{i,j}}\sum_{k=1}^{8}\left(f_{i,j}^k\cdot\left(H_{ik,jk}^t - H_{i,j}^t\right)\right) + S_{i,j}^{t+1}$$

$$f_{i,j}^k = \frac{1}{(\Delta l)_{i,j}^k}\cdot\left|\frac{H_{ik,jk}^t - H_{i,j}^t}{(\Delta l)_{i,j}^k}\right|^{-\frac{1}{2}}\cdot\left(w_{ci,j}^{k,t}\cdot\frac{m}{n_{ci,j}^{k,t}}\cdot\left(h_{ci,j}^{k,t}\right)^{\frac{5}{3}} + w_{f_{i,j}^{k,t}}\cdot\frac{m}{n_{f_{i,j}^{k,t}}}\cdot\left(h_{f_{i,j}^{k,t}}\right)^{\frac{5}{3}}\right)$$

After solving this equation, one can obtain the change of water level over one time-step for each grid cell (i.e. $(\Delta H)_{i,j}^{t+1}$), and then renew the water level and the inundation extent.

3.7 Coupling of unsaturated soil water and groundwater

The hydrostatic equilibrium soil moisture distribution is usually described by a steady state solution of Richards equation that is deduced from the situation that the hydraulic potential above water table is constant, i.e. $\varphi=\varphi_m+\varphi_g=C$. It is to say that Darcy's law (Eq. 3-5) is in a zero-flux condition where the upward diffusive flux equals to the downward gravitational flux, i.e.

$$-K(\theta)\frac{\partial\varphi_m}{\partial z} = K(\theta)\frac{\partial\varphi_g}{\partial z} \tag{3-37}$$

where K is the hydraulic conductivity [m/s], θ is the volumetric soil water content [m^3/m^3], φ_m is the soil matric potential [m], φ_g is the gravitational potential [m], z signifies the vertical coordinate [m].

With the expressions of φ_m (see in Eq. 3-9) and $K(\theta)$ (see in Eq. 3-8) in Clapp and Hornberger model (Clapp and Hornberger, 1978), Eq. 3-37 is reformulated as

$$\frac{b}{\theta^{b+1}}\cdot\frac{\partial\theta}{\partial z} = \frac{1}{\varphi_s}\cdot\frac{1}{\varphi_s^b}$$

where φ_s is the air-entry matric potential [m], θ_s is the saturated soil moisture [m^3/m^3].

Integrating from the groundwater table, z_g, to one position above the groundwater table (with an elevation of z), gives

$$\frac{\theta(z)}{\theta_s}=\left(1-\frac{z-z_g}{\varphi_s}\right)^{-1/b} \tag{3-38}$$

By substituting the redefinition of the effective saturation into Eq. 3-38, one rearranges the terms to express the equilibrium volumetric water content, θ_E, as

$$\theta_E(z)=\theta_r+(\theta_s-\theta_r)\left(1-\frac{z-z_g}{\varphi_s}\right)^{-1/b} \tag{3-39}$$

where θ_r is the residual water content [m^3/m^3].

Using Eq. 3-39, the equilibrium profile of soil moisture can be determined according to the specified groundwater depth and soil property parameters. This profile is used for the redistribution of the unsaturated soil water content in the near-groundwater-table zone and the dynamics of the groundwater table. When the aquifer is fully saturated, i.e. groundwater table approaches to or reaches the ground surface, saturation-excess runoff occurs. In the model scheme, the soil water exceeding the water storage capacity of the aquifer will be squeezed out, which is viewed as saturation-excess runoff.

As mentioned in Section 3.3, the flux at the bottom of the soil model domain is calculated using Darcy's law (q in Fig. 3-8(a)). But in the case of shallow groundwater (i.e. groundwater table located within the soil model domain), the flux at the domain bottom is zero; instead, the flux at the upper boundary of the layer where groundwater table is located (q in Fig. 3-8(b)) is used in this module.

Therefore, the change of soil water in the near-groundwater-table zone, Δw^{t+1}, is contributed by the interactive flux between unsaturated and saturated soil water (q in Fig. 3-8), the stream-aquifer interactive flux (see in Section 3.5), and lateral groundwater flows (see in Section 3.4). Hence, one can calculate inversely the updated groundwater head, z_{∇}^{t+1}, by balancing

$$w^t+\Delta w^{t+1}=\left(z_{\nabla}^{t+1}-z_{bot}\right)\cdot\theta_s+\int_{z_{\nabla}^{t+1}}^{z_{up}}\theta_E(z)dz$$

where z_{bot} is z-coordinate of the bottom of the unconfined aquifer [m], z_{up} is z-coordinate of the upper boundary of the groundwater-table-located layer [m], w^t is the soil water storage between z_{up} and z_{bot} at current time step [m].

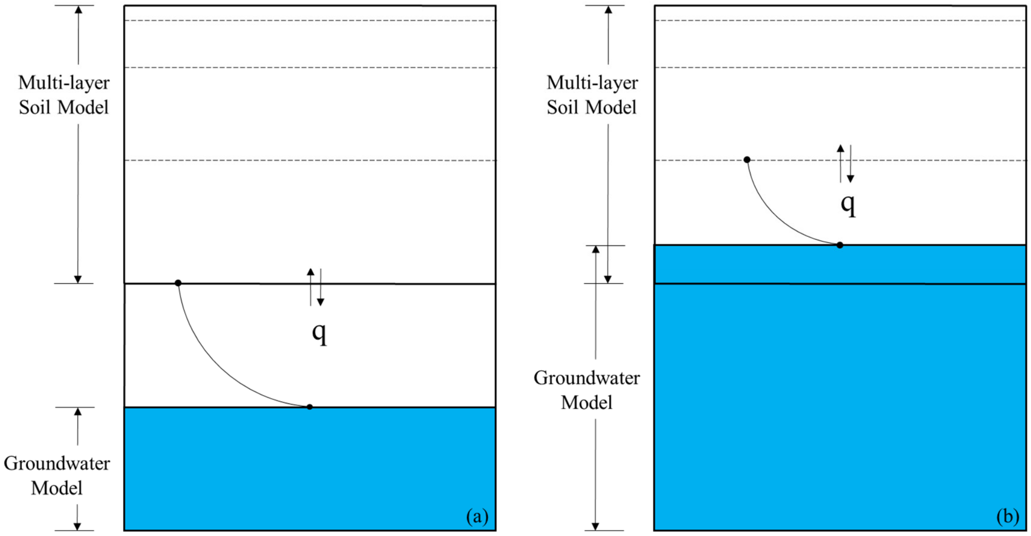

Fig. 3-8 Schematic diagram for unsaturated soil water, groundwater, and their coupling. (a): groundwater table is located below the soil model domain; (b): groundwater table is located within the soil model domain.

3.8 Introduction to the studied basin

3.8.1 Geographical features

The Huaihe basin, situated about the midway between the Yellow River and the Yangtze River (as shown in Fig. 3-9) and located in eastern China (111°55′–121°25′ E, 30°55′–36°36′ N), has a drainage area of 2.7×10^5 km^2. The landforms in the basin are divided into three types: mountains, hills, plains, which account for 9.7%, 6.5%, and 83.8% of the basin area, respectively.

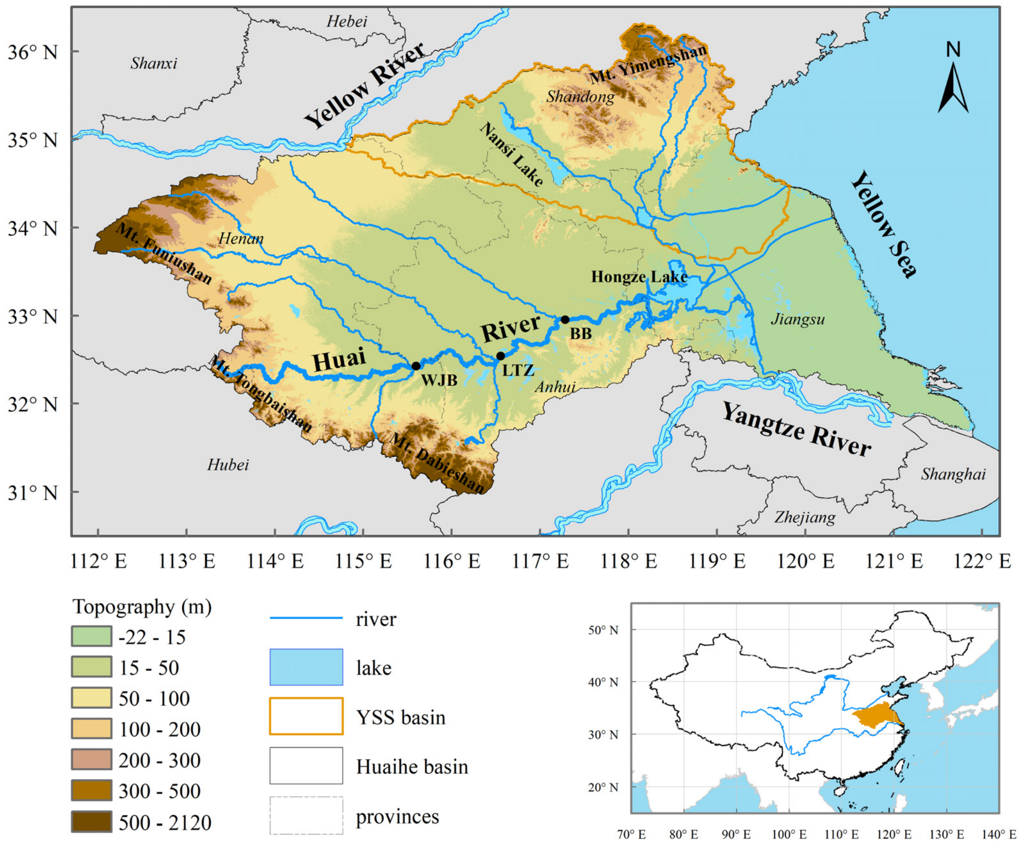

Fig. 3-9 Topography and geomorphology of the Huaihe basin. WJB (Wangjiaba), LTZ (Lutaizi), and BB (Bengbu) are three hydrological station in the Huai River.

The Funiu Mountains are a mountain range in southern Shanxi and western Henan in China (Shanxi and Henan are two provinces in China); the elevation generally ranges from 200 to 300 m, with a top elevation of 2153 m. A part of the Funiu Mountains is in the Huaihe basin (northwestern basin, see in Fig. 3-9). The Tongbai Mountains are a mountain range in Henan Province and Hubei Province in China, part of which are in the western Huaihe basin (see in Fig. 3-9); and these mountains mostly has an elevation from 200 to 300 m, with a maximum elevation of 1140 m. The Dabie Mountains are a major mountain range located in central China, part of which are in the southern Huaihe basin (see in Fig. 3-9). Running northwest-to-southeast, they form the main watershed between the Huai River and the Yangtze River. The elevation in the Dabie Mountains primarily ranges from 300 to 500 m, with the highest peak of 1774 m. The Yimeng Mountains are a mountain range in the Shandong Province of China, and the elevation mostly ranges from 200 to 500 m, with the highest peak at an elevation of 1155 m. The plains are located in the northern region of the Huai River (15–50 m elevation), in the western region of Nansi Lake (15–50 m elevation), and in the downstream area (2–10 m elevation). The hills are mainly situated in the extension of the mountains, with an elevation of 100–200 m in the western basin, 50–100 m elevation in the southern basin, and about 100 m elevation in the northeastern basin.

The Huaihe basin includes two independent catchments: the combined catchment of Yi River, Shu River, and Si River in the northeastern part (the YSS basin in Fig. 3-9) with a drainage area of 0.8×10^5 km^2, and the catchment of the Huai River with a drainage area of 1.9×10^5 km^2 (the Huai River basin, the remaining area in Fig. 3-9). The Huai River, the main stream of the Huai River basin, originates from the Tongbai Mountains and flows into the Yangtze River, and ends up to the ocean, running from west to east. The Huai River is separated to upstream, midstream, and downstream parts. The section of the Huai River above the Honghekou station (2 km to the Wangjiaba hydrological station (WJB in Fig. 3-9)) is defined as the upstream; it has a length of 360 km, a drainage area of 30630 km^2, a gradient of 980 m/360 km. The section from the Honghekou to the Zhongdu (i.e. the outlet of Hongze Lake (see in Fig. 3-9)) is the midstream of the Huai River, with a length of 490 km, a gradient of 16 m/490 km, and a drainage area of 128784 km^2. The remaining part is the downstream with a drainage area of 30660 km^2; the major part of the Huai River's flow via the Hongze Lake enters the Yangtze River along a stream with a length of 150 km and a gradient of 6 m/150 km.

3.8.2 Climatology and hydrology

The Huaihe basin locates in the climate transition zone, where the northern region of the Huai River is in the warm temperature semi-humid zone and the southern region of the Huai River in the subtropical humid zone. The rain band caused by the East Asian summer monsoon is characterized by stepwise northward advance from southern China and the western North Pacific in early-mid May to the Yangtze River valley and southern Japan in mid-June, then to north China and the Yellow Sea as well as the southern Japan Sea in late July. When the monsoon rain band is located in the Yangtze-Huaihe River basin, it is normally called Meiyu (Zhang et al., 2005). Summer monsoon rain band has a coherent physical feature associated with the occurrence of heavy and persistent precipitation. Mainly caused by the geographic difference and largely influenced by the inter-decadal variations of East Asian Summer Monsoon in the eastern China, the precipitation in the basin describes a high spatial and temporal variability (Ye and Li, 2017). The Huaihe basin is prone to extreme events, such as drought and flood.

According to the observed precipitation from meteorological stations (Ye and Li, 2017), the mean annual precipitation from 1961 to 2010 is 896 mm/a in the Huaihe basin. Spatially, it ranges from 600 to 1400 mm/a (see in Fig. 3-10), with a notably decreasing trend from southeast to northwest. There is maximum annual rainfall in the region of the Dabie Mountains (> 1100 mm/a). The rainfall in the Huaihe basin occurs predominantly in summer months (JJA), occupying 52.1% of annual precipitation. The mean precipitation in spring (MAM), autumn (SON), and winter (JJA) are 185, 174, and 70 mm, respectively. Also, the precipitation from 1961 to 2010 shows a high inter-annual variability, with a maximum annual precipitation (1240 mm/a) in 2003 and a minimum annual precipitation (598 mm/a) in 1978.

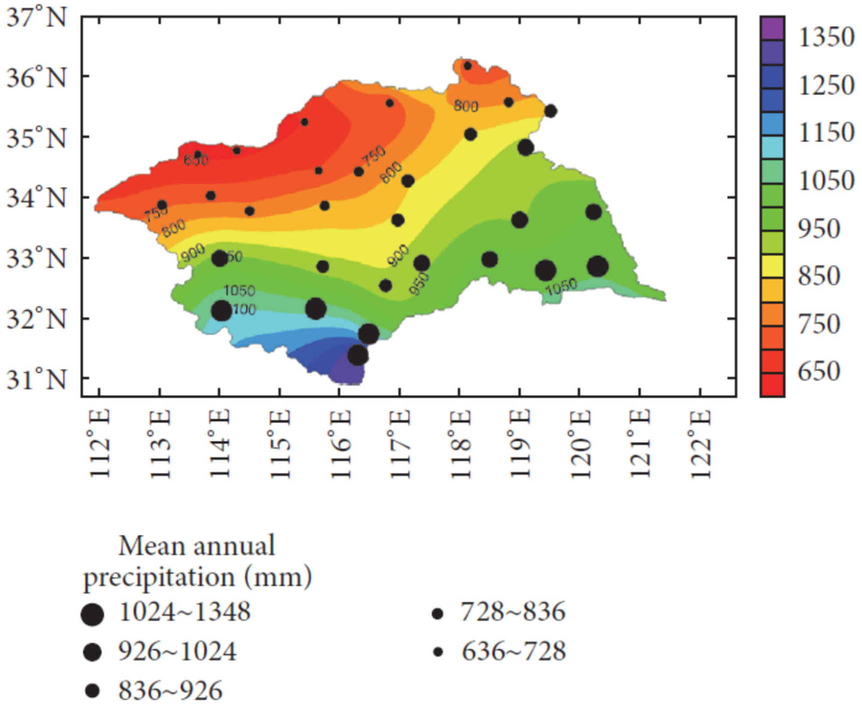

Fig. 3-10 Spatial distribution of the mean annual precipitation observed from 1961 to 2010. [Adopted from Ye and Li (2017), Figure 2(a)]

According to monthly global gridded high-resolution air temperature data (Willmott et al., n.d.), the spatial distribution of the mean air temperature from 1961 to 2010 in the Huaihe basin is depicted as Fig. 3-11. Spatially, the air temperature in the basin gradually decreases from south to north and from coastal to inland. The mean air temperature in the basin is mostly in the range of 13.0 to 16.2 °C, with the highest mean monthly temperature in July (27.7 °C) and the lowest in January (1.0 °C). There is a relatively high mean air humidity (66–81%) in the basin, with the highest value in summer (> 80%) and the lowest in winter (about 65%).

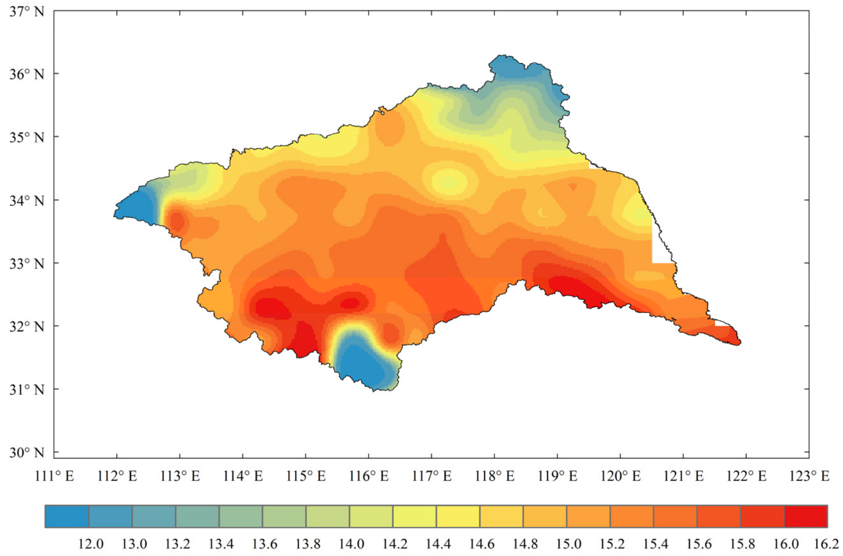

Fig. 3-11 Spatial distribution of the mean air temperature (ºC) in the Huaihe basin observed from 1961 to 2010 (Willmott and Matsuura, n.d.).

According to the measurements from 1956 to 2000, the mean annual runoff in the Huaihe basin is 220 mm/a, with 238 mm/a in the Huai River basin and 181 mm/a in the catchment of the Yi-Shu-Si Rivers. The runoff in the basin shows an uneven spatiotemporal distribution. Benefiting from intense precipitation and the topographic condition, the runoff in the mountainous regions is higher; the mean annual precipitation in the mountains and the southern region of the Huai River exceeds 300 mm/a. Conversely, the runoff in the plains is small; for example, the mean annual runoff in the plains north of the Huai River and west of Nansi Lake (see in Fig. 3-9) is lower than 100 mm/a.

Like the distribution of precipitation in the Huai River basin, the runoff is also concentrated in the flood season (June - September), which accounts for about 60% of the annual runoff. In the basin of Yi-Shu-Si Rivers, this ratio is even higher (70–80%). The inter-annual variability of runoff is more significant than that of precipitation. The ratios of maximum to minimum annual runoff at the observation stations range from 5 to 30, but this ratio is smaller (< 10) in the mountains.

The Wangjiaba, Lutaizi, and Bengbu stations are three important outlets of the Huai River, which are abbreviated as WJB, LTZ, and BB, respectively, in this study. Their specific locations in the basin are shown in Fig. 3-9. The mean annual runoff flowing through these three stations is calculated according to the observed river discharges from 1956 to 2000 and the areas of the subbasins. The results are listed in Table 3.1. The BB subbasin occupies 64% of the total area of the Huai River basin, and the generated runoff in this subbasin contributes 67% of flood water in the Huai River. Whereas, 84% of the river runoff at the BB station stems from the drainage area above the LTZ station.

Table 3.1 The observed mean annual river discharge from 1956 to 2000 at the WJB, LTZ, and BB hydrological stations, and the mean annual runoff in the corresponding subbasin.

hydrological station	mean annual discharge (× 10^4 m^3)	subbasin	drainage area (km^2)	mean annual runoff (mm)
WJB	1018285	WJB subbasin	30630	333
LTZ	2550734	LTZ subbasin	88630	288
BB	3049256	BB subbasin	121000	252
/	/	Huai River basin	190000	238

Note: the mean annual discharges at the three hydrological stations are cited from Yan et al. (2010); the mean annual runoff is calculated based on the mean annual discharges and the drainage areas.

4 Hillslope Runoff Parameterization and its Application

In the previous chapter, the coupling of the Weather Research and Forecasting (WRF) Model, the Noah-Multiparameterization Land Surface Model (Noah-MP LSM), and the distributed hydrological model (HMS) is presented; several coupled models are available, e.g. the coupled land surface and hydrological model NoahMP-HMS that is offline driven by meteorological forcing data. In this chapter, a new parameterization for hillslope runoff is developed, where the influence of hillslope topography on runoff production has been considered. In order to evaluate the effectiveness of the new parameterization and to validate the model, the offline simulations by the NoahMP-HMS with and without this parameterization are compared to the observation. Furthermore, the spatiotemporal variability of the hydrological processes in the Huaihe basin is investigated based on the long-term simulation.

4.1 A new parameterization for hillslope runoff

As mentioned in Chapter 2, the heterogeneity of soil moisture and resulting runoff generation strongly effects the heat and water budget at the land surface. The infiltration and surface runoff scheme shown in Section 3.2 is based on a homogeneous horizontal grid, neglecting the sub-grid soil moisture variability. Whereas, soil moisture is associated with relative elevation and topography, such as slope aspect and position (Qiu et al., 2001). Consequently, it is very necessary to represent the impact of subgrid-scale topography on soil moisture to better describe the generation of surface runoff.

As illustrated in Section 3.2, the actual infiltration and the infiltration-excess runoff are determined by the precipitation rate and the infiltration capacity; the infiltration capacity is simplified as the hydraulic conductivity of the near-surface soil at its maximum wetness, i.e. $f^{*}=K(\theta_{max})$. Based on homogeneous horizontal grids in the original scheme, the maximum soil water volumetric content is the saturated soil moisture (Fig. 4-1(a)). However, significant deviations have been detected between and the observation and the simulation of the original NoahMP-HMS (as elaborated in Section 4.3).

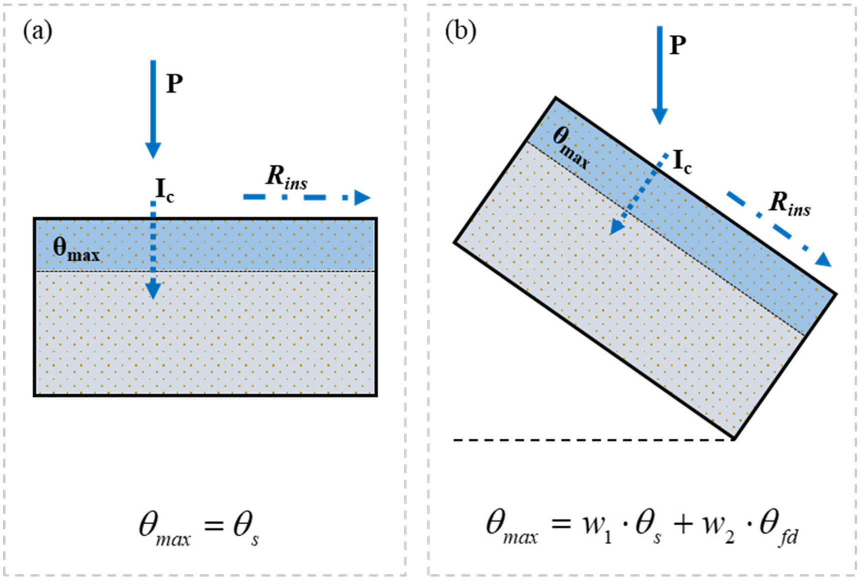

Fig. 4-1 Schematic diagram of infiltration capacity in the original (a) and the modified (b) schemes. In this figure, P represents precipitation intensity, I_c is infiltration capacity, R_{ins} is infiltration-excess runoff.

As any soil water in excess of field capacity drains away due to gravity, the soil water holding capacity is reduced under hillslope topography (as illustrated in Fig. 4-1(b)). Field capacity is the upper limit of storable water in the soil. he maximum soil moisture (θ_{max}) is hence assumed as a weighted average of saturated soil moisture (θ_s) and field capacity (θ_{fd}), i.e.

$$\theta_{max} = w_1 \cdot \theta_s + w_2 \cdot \theta_{fd}$$

By introducing field capacity into the formula of the maximum soil moisture, the infiltration capacity in hillslope topography is weakened, and its ability of generating infiltration-excess runoff is strengthened. As such, the production of hillslope runoff in hillslope topography is parameterized via the infiltration capacity.

Table 4.1 lists the calculation formulas for infiltration capacity and infiltration-excess runoff in the original and the modified scheme. In the original scheme, the infiltration capacity is estimated as the saturated hydraulic conductivity of the top-layer soil, which adopts for the whole basin. The occurrence of infiltration-excess runoff and its amount depend on precipitation intensity and the infiltration capacity.

Table 4.1 The calculation of infiltration capacity and infiltration-excess runoff in the infiltration and surface runoff schemes.

scheme	infiltration capacity f^*		infiltration-excess runoff R_{ins}
original	$f^* = K(\theta_s)$	whole basin	$R_{ins} = \begin{cases} 0 & p \le f^* \\ p - f^* & p > f^* \end{cases}$
modified	$f^* = \begin{cases} K\left(\dfrac{\theta_s + \theta_{fd}}{2}\right) \\ K(\theta_s) \end{cases}$	mountains and hills plains	$R_{ins} = \begin{cases} 0 & p \le f^* \\ p - f^* & p > f^* \end{cases}$

In the modified infiltration and surface runoff scheme, the new parameterization is used to calculate the infiltration capacity under hillslope topography. Hence, the infiltration capacity in mountainous and hilly areas is estimated as the hydraulic conductivity of the top-layer soil at the wetness averaged of saturated soil moisture and field capacity. For plains, the calculation of infiltration capacity is identical to that in the original scheme. The implement of the new hillslope runoff parameterization is expected to improve the runoff simulation in the NoahMP-HMS.

4.2 Model setup of the NoahMP-HMS

To calibrate and validate hydrological parameters and to illustrate the reliability of the new parameterization, the coupled land surface and hydrological model NoahMP-HMS is first applied to the Huaihe basin in China. For the simulation in the Huaihe basin, a domain is selected to cover the whole basin, and the ocean to the east to capture the water flow along the Huai River and Yangtze River and it ends up to the ocean, as shown in Fig. 4-2. The domain consists of 48 × 54 grids with a resolution of 20 km in Lambert conformal conic projection. The time step is 30 minutes for the land surface simulation and the hydrological simulation. Spin-up of decade is required to achieve a quasi-equilibrium condition, when the hydrological variable fields are used as initial conditions for the NoahMP-HMS simulation.

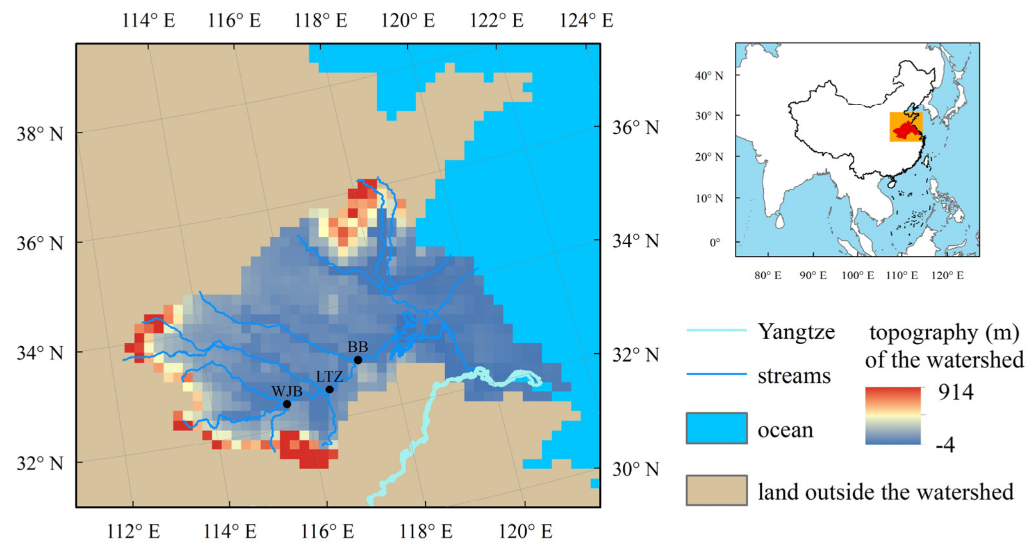

Fig. 4-2 Domain diagram of the simulation for the Huaihe basin.

The NCEP/NCAR reanalysis global datasets, including air temperature, humidity, surface pressure, wind, cloud cover, radiation (No. 1–11 in Table 4.2), are used to drive the NoahMP-HMS. To reduce the uncertainty of input, the gridded precipitation observation (No. 12 in Table 4.2) is used as precipitation input; this dataset is spatially and temporally interpolated from the measured precipitation in 833 meteorological stations in China, with the consideration of the impact of topography on precipitation interpolation (Li et al., 2015). The land surface parameters, e.g. soil type, land use type, etc. (No. 13–20 in Table 4.2) are extracted by the WRF preprocessing

For groundwater modelling, the thickness of unconfined aquifer and drainable porosity are required to characterize subsurface hydrological conditions. In this study, the drainable porosity is represented by porosity. The aquifer thickness (No. 22 in Table 4.2) is deduced according to the geological data of China, based on the known relationship between geological type and hydrological parameters in American (Yang et al., 2011). The average groundwater head at 5' resolution (~ 9 km) (No. 21 in Table 4.2) simulated by global groundwater model (De Graaf et al., 2017) is used to initialize groundwater head.

For terrestrial hydrological modelling, terrain elevation, catchment division, channel depth and width (No. 24–27 in Table 4.2) are in need to characterize surface hydrological conditions. These hydrological characteristic parameters can be obtained with ZB algorithm (Yu et al., 2006), with hydrologically correct DEM (Digital Elevation Model) and flow accumulation data (from USGS geographic database HYDRO1K).

The Manning roughness coefficient (No. 28 in Table 4.2) and the hydraulic conductance of stream-aquifer interconnection (No. 29 in Table 4.2) are important parameters for terrestrial hydrological simulations. But there is a lack of effective ways to collect the spatial distributions of these parameters, and hence calibration and validation for them are required. Li et al. (2015) calibrated the hydraulic conductance of stream-aquifer interconnection in different subbasins according to the hydrogeological characteristics: 10^{-8} s^{-1} in the WJB subbasin, 10^{-6} s^{-1} in the WJB-LTZ subbasin, 10^{-5} s^{-1} in the LTZ-BB subbasin, 10^{-5} s^{-1} in the downstream area. The Manning roughness coefficient in the Huaihe basin is selected as 0.02 on the basis of the studies of Bao and Zhao (2011) and Yu et al (2016). And the approximate Bayesian computation method is used to optimize the Manning roughness coefficient (see details in Appendix 7.3).

The subgrid-average slope is calculated based on the USGS HYDRO1K slope dataset at a resolution of 1 km (No. 23 in Table 4.2). In the Huaihe basin, the grids with average slope higher than 0.10 degree is defined as hillslope topography. It covers the mountainous and hilly areas, which are in the southern, northeastern, and western region of the basin. Fig. 4-3 depicts the distribution of hillslope and plain areas in the basin.

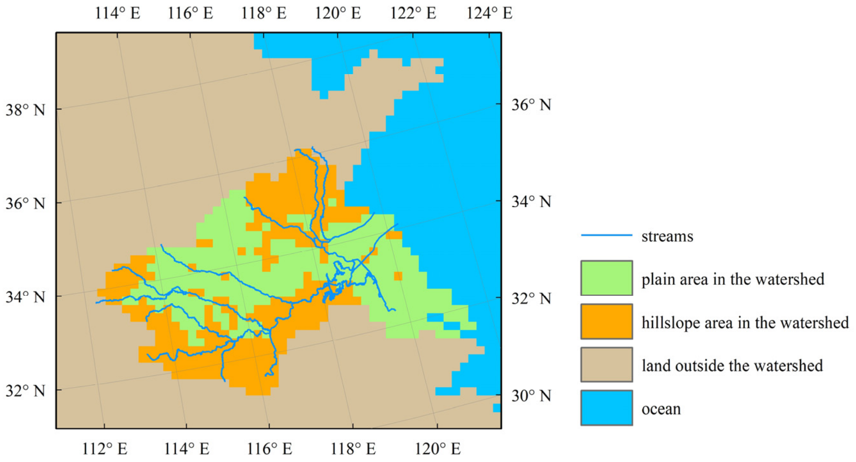

Fig. 4-3 The spatial distribution of hillslope areas and plains within the Huaihe basin.

Table 4.2 Inputs and parameters for the NoahMP-HMS.

No.	Variable	Unit	File/Variable Name	Source
1	air temperature at 2 m	K	air.2m.gauss.#.nc	NCEP/NCAR reanalysis data
2	specified humidity at 2 m	kg/kg	shum.2m.gauss.#.nc	
3	surface pressure	N/m^2	pres.sfc.gauss.#.nc	
4	U-wind at 10 m	m/s	uwnd.10m.gauss.#.nc	
5	V-wind at 10 m	m/s	vwnd.10m.gauss.#.nc	
6	total cloud cover	m^2/m^2	tcdc.eatm.gauss.#.nc	
7	downward longwave radiation flux	W/m^2	dlwrf.sfc.gauss.#.nc	
8	visible beam downward solar flux	W/m^2	vbdsf.sfc.gauss.#.nc	
9	near IR beam downward solar flux	W/m^2	nbdsf.sfc.gauss.#.nc	
10	visible diffuse downward solar flux	W/m^2	vddsf.sfc.gauss.#.nc	
11	near IR diffuse downward solar flux	W/m^2	nddsf.sfc.gauss.#.nc	
12	gridded observation precipitation	m/s	precipitation	833 meteorological sites in China
13	terrain height	m	topo_*	WRF Geographical database
14	top layer soil type	—	soiltype_top_*	
15	bottom layer soil type	—	soiltype_bot_*	
16	deep soil temperature	K	soiltemp_1deg	
17	monthly leaf area index	—	lai_modis_*	
18	monthly green fraction	—	greenfrac_fpar_modis	
19	land use type	—	landuse_*	
20	monthly surface albedo	%	albedo_ncep	
21	groundwater head	m	gw_head_5m_1L.msp	global model (De Graaf, 2017)
22	unconfined aquifer thickness	m	aqthick	geological data, empirical model
23	Subgrid-average slope	degree	slope	USGS HYDR1K
24	hydrological terrain height	m	elevation	USGS HYDR1K
25	channel depth	m	bank	ZB algorithm (Yu et al., 2006)
26	channel width	m	width	
27	drainage basin boundaries	—	maskbasin	
28	The Manning roughness coefficient	s/m$^{1/3}$	rough	calibrated in subbasins
29	The hydraulic conductance of stream-aquifer interconnection	s^{-1}	C_s	

Note: # signifies specified year for data, * represents the spatial resolution of data.

4.3 Performance evaluation and model verification

With the model configurations aforementioned in Section 4.2, the NoahMP-HMS with the original and the modified infiltration and surface runoff scheme are separately used to simulate the hydrological processes of the Huaihe basin from 1980 to 1987. Unlike the original scheme, the modified version includes a new hillslope runoff parameterization where the effect of hillslope topography on the generation of surface runoff is considered. The reliability of this new parameterization is examined, and the performance of the NoahMP-HMS is validated, by comparing both simulations and the observation. The comparisons are carried out concerning streamflow estimates and water budget.

4.3.1 Water budget

The partitioning of precipitation into runoff and infiltration strongly affects regional water balance, and the analysis of water budget is an essential way to improve the parameterization scheme. Therefore, the terrestrial water budget (see details in Appendix 7.1) in the simulations are compared to the observation, including precipitation, evapotranspiration, runoff, and water storage change. The precipitation in the terrestrial water budget only involves the observation precipitation which is used to drive the NoahMP-HMS.

The simulated water budgets in the subbasin of WJB, LTZ, and BB (see their specific locations in Fig. 4-2) are computed separately and listed in Fig. 4-4(a)–(c). Meanwhile, Fig. 4-4(d) shows the partitioning of precipitation to evapotranspiration, runoff, and the change of water storage. It is found that in these three basins, the change of water storage in the watershed is largely contributed by the change of water storage in the aquifer, with ratios exceeding 99%. In addition, Table 4.3 shows the observed and simulated mean annual runoff from 1980 to 1987 in the watershed of WJB, LTZ, and BB.

Table 4.3 The mean annual discharge at the WJB, LTZ, and BB station observed from 1980 to 1987, and the mean annual runoff in the corresponding watersheds.

station	observed mean annual discharge ($\times 10^4$ m^3)	drainage area (km^2)	subbasin	mean annual runoff (mm/a)		
				observed	original scheme	modified scheme
WJB	1071310	30630	WJB	350	102	329
LTZ	2427378	88630	LTZ	274	97	288
BB	3062803	121000	BB	253	89	245

Since the NoahMP-HMS is offline driven by the meteorological forcing data, the amounts of precipitation in the simulation using the original and the modified scheme are identical. The mean annual precipitation from 1980 to 1987 in the WJB, LTZ, and BB subbasin is 1037, 985, and 933 mm/a, respectively. While using the modified scheme, the simulated mean annual runoff increases from 102 to 329 mm/a in the WJB subbasin, from 97 to 288 mm/a in the LTZ subbasin, and from 89 to 245 mm/a in the BB subbasin. As shown in Table 4.3, the observed mean annual runoff from 1980 to 1987 in these three subbasin is 350 (WJB), 274 (LTZ), and 253 (BB) mm/a, respectively.

The comparison shows that using the original scheme, all the simulated runoff in three subbasin are lower than the observation, with relative biases higher than 60%; the simulated runoff with the modified scheme is comparable to the observation, with a relative bias of -6%, 5%, and -3% in the WJB, LTZ, BB subbasin, respectively. This contrast indicates that the implement of hillslope runoff parameterization in the NoahMP-HMS improves the model ability to reproduce the runoff. By this improvement, simulated runoff of the Huaihe basin approaches to the observation.

Table 4.4 shows the mean annual value of different runoff components in the modified simulation and their contributions to total runoff. The total runoff is composed of surface runoff and groundwater supply to streams; surface runoff results from rainfall events, while groundwater supply occurs by groundwater seepage to streams. In the WJB, LTZ, and BB subbasin, the surface runoff accounts for 91.3%, 89.9%, and 89.0% of the total runoff, while the groundwater supply occupies 8.7%, 10.1%, and 11.0%, respectively. It is to say that the runoff resulted from rainfall events is dominated in the river runoff of these three subbasins. This finding agrees to the study of Huang (1992) that rainwater is the main recharge source in the Huai River.

Table 4.4 The mean annual runoff from 1980 to 1987 simulated by the NoahMP-HMS with the modified scheme, and the contributions of various runoff components.

	WJB subbasin		LTZ subbasin		BB subbasin	
	runoff (mm/a)	ratio (%)	runoff (mm/a)	ratio (%)	runoff (mm/a)	ratio (%)
R	329		288		245	
R_{sf}	300	91.3	259	89.9	218	89.0
Q_{cg}	29	8.7	29	10.1	27	11.0

Note: R_{total}: total runoff, R_{sf}: surface runoff, Q_{cg} (+): groundwater supply to streams.

Fig. 4-4(d) shows the partitioning of precipitation to evapotranspiration, runoff, and water storage change in term of percentage. In the simulation with the modified scheme, the runoff which outflows from the subbasin via river discharge accounts for 32%, 29%, and 26% of annual precipitation in the WJB, LTZ, BB subbasin, respectively; in the original simulation, the annual runoff-precipitation ratios in all three subbasins are 10%. A part of annual precipitation returns to the atmosphere through evapotranspiration in the modified simulation, reaching 62%, 64%, and 67% in the WJB, LTZ, and BB subbasin, respectively; while the annual evaporation-precipitation ratios in the original simulation are 72%, 72%, and 75%, respectively. For each of the subbasins only about 1% of precipitation is retained in the watershed in the modified simulation, but a higher proportion of precipitation – 12% (WJB), 11% (LTZ), and 8% (BB) – is stored in aquifers in the original simulation.

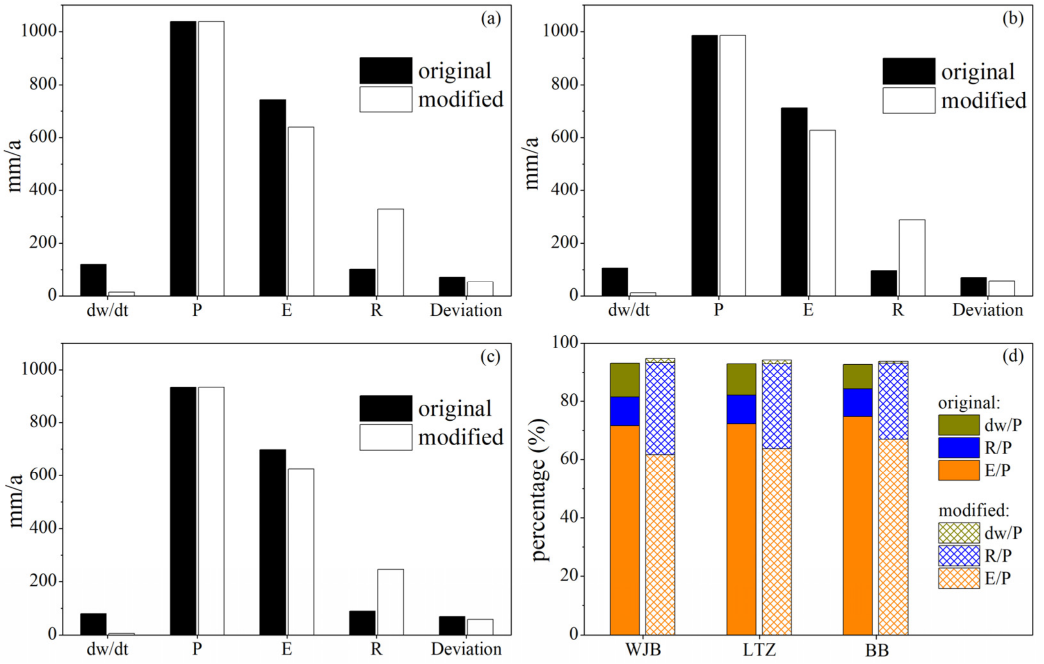

Fig. 4-4 Mean annual terrestrial water budget from 1980 to 1987 simulated by the NoahMP-HMS with the original and the modified scheme – (a) WJB subbasin, (b) LTZ subbasin, (c) BB subbasin – and the partitioning percentage of precipitation (d). P: precipitation, E: evapotranspiration, R: runoff, dw/dt: the change of water storage.

Overall, in the coupled land surface and hydrological simulation with the original scheme, the water storage from 1980 to 1987 presents an unreasonably large increase in three subbasins, while the simulated runoff is significantly lower than the observation. According to the water budget (Fig. 4-4), we know that is mainly because the infiltration in the original scheme is excessively high, which constrains the generation of infiltration-excess runoff. On the contrary, the changes of water storage in the three subbasins are insignificant in the modified simulation, and almost all the precipitation is released from the watershed by river discharge and evapotranspiration. This is in accordance with the long-term water balance dynamic.

4.3.2 Streamflow estimates

Streamflow is an important prognostic variable in the model. In this study, three common statistical indices are used to evaluate the agreement of the simulated streamflow and the observation: (1) Nash-Sutcliffe coefficient of efficiency index (NSI), (2) Pearson product-moment correlation coefficient (PMC), and (3) water balance index (WBI). Their definitions are shown in Appendix 7.2. The efficiency coefficient (NSI) is a measure of fitness for simulated and observed river discharge, in the range of -∞ and 1.0 (a perfect fit), which mainly reflects the ability of the model to simulate the observed peak flow. The NSI value of zero indicates that the model is capable to describe the mean of observed streamflow; the coefficient between 0 and 1 implies that the deviation of simulated and observed streamflow cam be appropriately described. The correlation coefficient (PMC), valued between 0 and 1 (perfect positive correlation), describes the correlation between observed and simulated streamflow in timing. The water balance index (WBI) measures the model ability to reconstruct water balance processes, and a value close to 1 means a high-precision simulation for it.

Fig. 4-5 shows the performance indices between the observed and the simulated daily streamflow at the hydrological station of WJB, LTZ, and BB from 1980 to 1987. Fig. 4-6 shows the time series of the observed and the simulated daily streamflow at these three hydrological stations from 1980 to 1987.

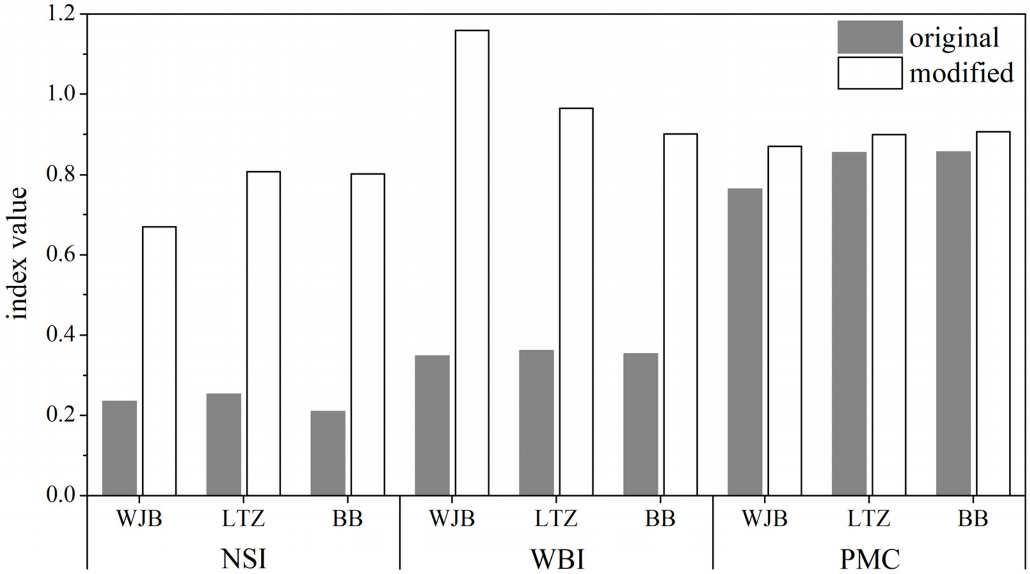

Fig. 4-5 Goodness-of-fit indexes between the observed river discharge and the simulated daily streamflow at the WJB, LTZ, and BB station.

As shown in Fig. 4-5, the correlation coefficients of the simulated daily streamflow using the original scheme are 0.76, 0.85, 0.86 at the WJB, LTZ, and BB station, respectively; while their coefficients in the modified simulation are 0.87, 0.90, and 0.91. These correlation coefficients are high, which indicates a good agreement of temporal variation between the observed and the simulated daily streamflow. And the modified simulation shows a slightly better agreement. As illustrated in Fig. 4-6, the temporal variations of simulated daily streamflow in two simulations are consistent with the corresponding observations at the three hydrological stations.

The efficiency coefficients and water balance indexes of daily streamflow provide further evidences to the improvement by the modified scheme. In the modified simulation, the efficiency coefficients of simulated daily streamflow at the WJB, LTZ, and BB station, are 0.67, 0.81, and 0.80, respectively; while those are about 0.22 in the original simulation. As shown in Fig. 4-6, the daily streamflow simulated by the modified model well matches the observation at three stations, notably better than that of the original simulation; the flood peaks are seriously underestimated in the latter simulation. Accordingly, the NoahMP-HMS with the modified scheme has a great ability to reproduce the peak flow of the hydrograph.

The case of the water balance index is very similar to that of the efficiency coefficient mentioned above. The WBI values at the WJB, LTZ, and BB station with the modified scheme are 1.16, 0.96 and 0.90, respectively, while those with the original scheme are around 0.35. The low WBI value (0.35) illustrates that the river runoff from 1980 to 1987 simulated by the NoahMP-HMS with the original scheme is significantly lower than the observation at three stations. Conversely, the WBI value in the modified simulation is close to 1.0, which means that the NoahMP-HMS with the modified scheme simulates water balance processes well.

Overall, the evaluation indices of daily streamflow show that the performance of the NoahMP-HMS with the modified scheme is better than that with the original scheme. It indicates that the implementation of the hillslope runoff parameterization enables the NoahMP-HMS to behave better in simulating the hydrological processes of the Huaihe basin, especially during the high-flow period. By describing the hillslope runoff, the NoahMP-HMS is able to capture the observed daily river discharge in a high accuracy, with a high precision estimating the occurrence and the intensity of floods. Consequently, the NoahMP-HMS has a greater ability to reproduce the hydrological processes and terrestrial water balance in the Huaihe basin.

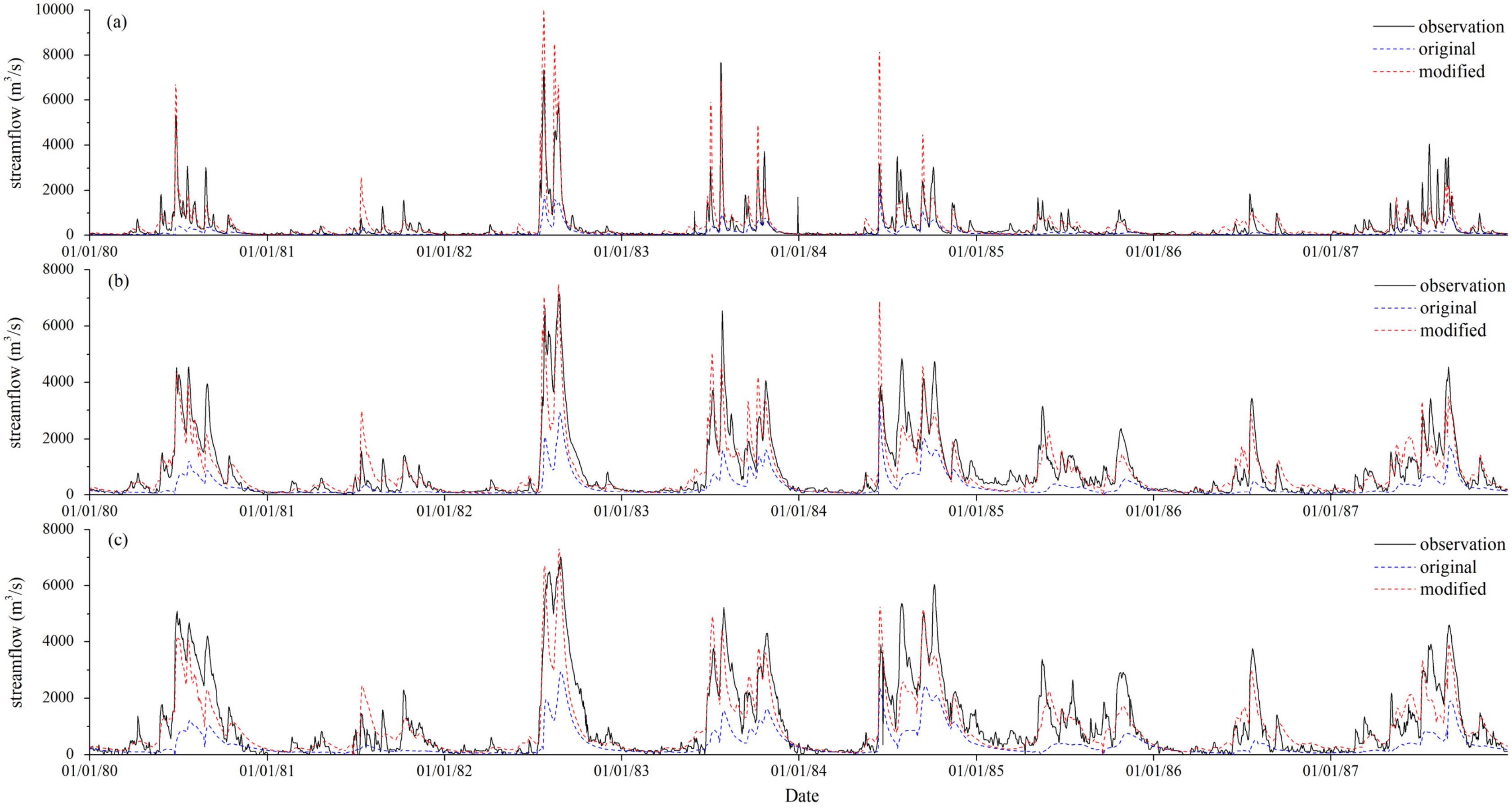

Fig. 4-6 Comparisons of the observed and the simulated daily streamflow from 1980 to 1987 at the hydrological station of WJB (a), LTZ (b), BB (c). Black solid line: the observation, blue dash line: the NoahMP-HMS simulation with the original scheme, red dash line: the simulation with the modified scheme.

4.4 Spatiotemporal variability of hydrological processes

In the previous section, the NoahMP-HMS with the new parameterization of hillslope runoff is validated, and it shows a good agreement with the observation in terms of water budget and streamflow estimates. In this section, the model is used for a long-term land surface and hydrological simulation from 1979 to 2003 in the Huaihe basin at the same temporal and spatial resolution as that of the validation simulation. It is aimed to investigate the spatiotemporal variability of the hydrological processes in the basin, and their response to climate variability.

4.4.1 Precipitation

It is worth to inspect the spatial and temporal pattern of precipitation over the basin because hydrological processes are strongly sensitive to this crucial input. Fig. 4-7 depicts the seasonal mean of observed precipitation from 1979 to 2003 within the Huaihe basin. In Fig. 4-7, Fig. 4-9, Fig. 4-15, millimeters per day is adopted as the unit in order to eliminate the impact of the inconsistency of number of days in four seasons.

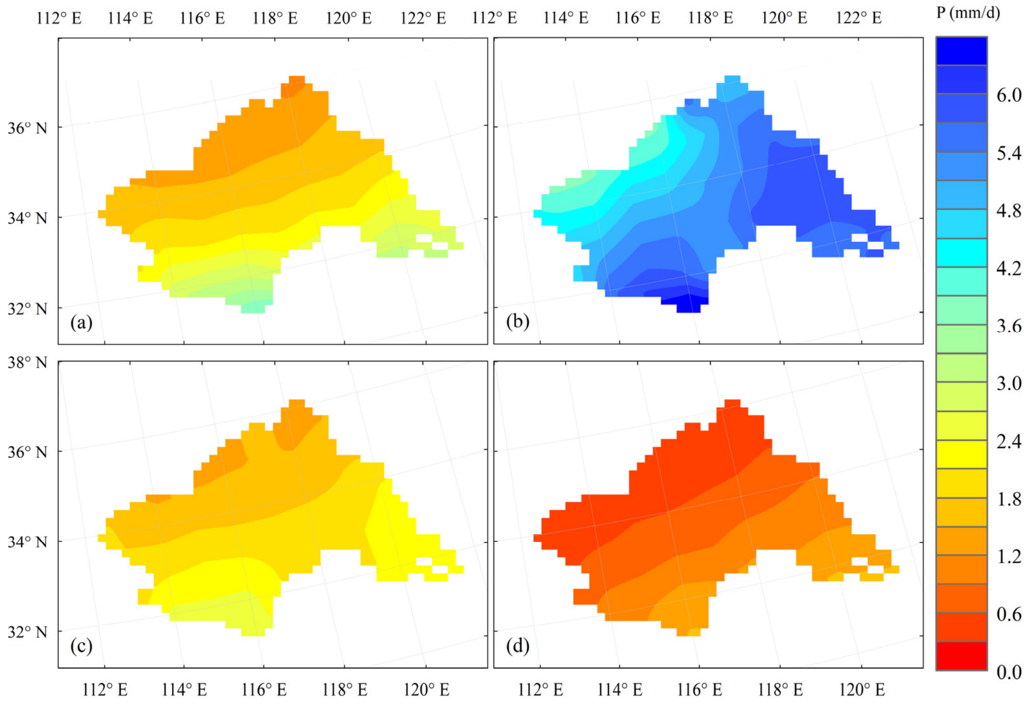

Fig. 4-7 Spatial distribution of the 25-year-averaged seasonal precipitation amount in the Huaihe basin: (a) spring, (b) summer, (c) autumn, and (d) winter.

As shown in Fig. 4-7, the precipitation within the basin generally decreases from southeast to northwest. Throughout four seasons regions with higher precipitation are located in the southern and eastern basin, i.e. the southern region of the Huai River and the downstream plains. An obvious characteristic in the annual pattern of precipitation is that the highest rainfall is found in summer while the least in winter. Meanwhile, the statistical calculation of precipitation intensity (not exhibited herein) shows that intense rainfall (> 25 mm/d) occurs more frequently in summer, while low-intensity rainfall (< 10 mm/d) dominates in winter.

In a similar manner, the monthly mean precipitation observed from 1979 to 2003 are spatially averaged and shown in Fig. 4-8, as well as the corresponding contributions to annual precipitation. The 25-year-averaged annual precipitation is 912 mm/a. In the basin, heavy rainfall is obtained in the Meiyu season due to the associated rain band over eastern China from June to August. Precipitation in summer accounts for 53% of annual precipitation; the precipitation during wet season (i.e. May – September in the Huaihe basin) contributes 70%.

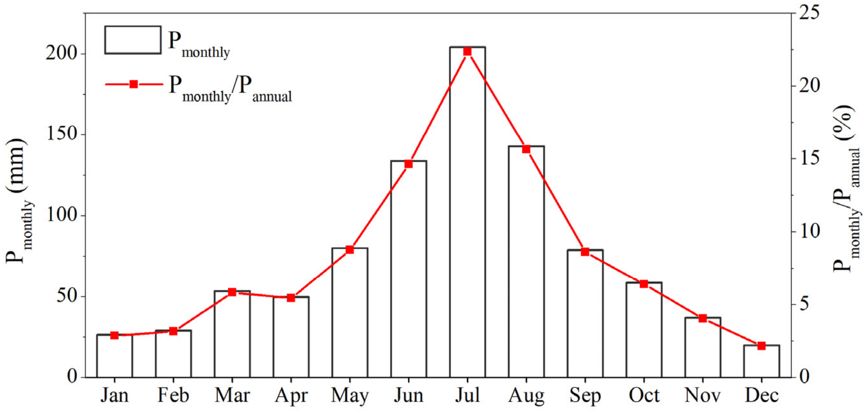

Fig. 4-8 Mean monthly precipitation amount ($P_{monthly}$) in the Huaihe basin from 1979 to 2003, and the corresponding percentage to annual precipitation ($P_{monthly}/P_{annual}$).

4.4.2 Evapotranspiration

Evapotranspiration (ET) is the sum of evaporation and plant transpiration from the land and ocean surface to the atmosphere. In the NoahMP-HMS, the evapotranspiration over land is the sum of the contribution from each of three types of evaporation: direct evaporation from bare soil, plant transpiration, and evaporation of precipitation intercepted by the vegetation canopy (Godfery et al., 2010). In this study, the evaporation over lakes is not calculated using lake model but being equal to the potential evaporation around lakes. The potential evaporation is the maximum possible evaporation that could occur over an open water surface under existing atmospheric condition. The calculation of potential evaporation involves an energy balance approach based on the Penman relationship. Hence, the evaporation of water surface at lakes reflects the evaporation capacity of the regions around them in the NoahMP-HMS simulation.

The simulated evapotranspiration from 1979 to 2003 is averaged in season and their spatial distributions within the basin are depicted in Fig. 4-9. Similar to precipitation, there is the highest evapotranspiration in summer (Fig. 4-9(b)) and the lowest in winter (Fig. 4-9(b)) within the basin. Concerning the spatial distribution of evapotranspiration, the evapotranspiration decreases southeastwards over the Huaihe basin. The region with the lowest evapotranspiration is in the northern mountainous area, i.e. the Yimeng Mountains (see in Fig. 3-9), while the most intense in the downstream plains.

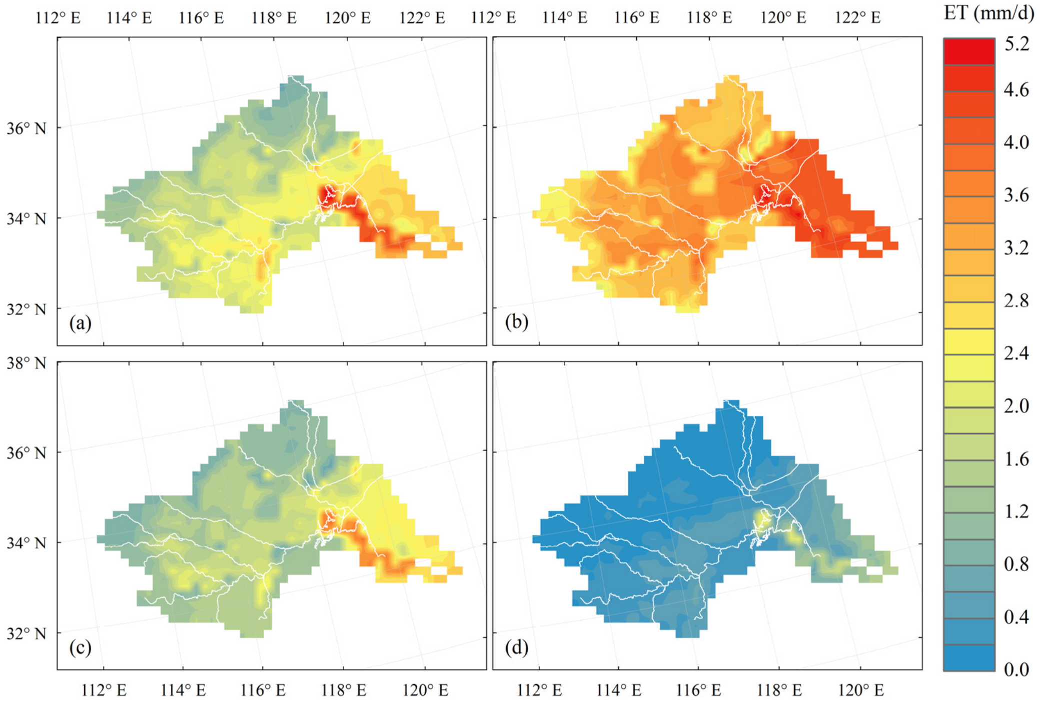

Fig. 4-9 Spatial distribution of 25-year-averaged seasonal evapotranspiration amount in the Huaihe basin: (a) spring, (b) summer, (c) autumn, (d) winter.

As shown in Fig. 4-9, the evaporation at Hongze Lake distinguishes from the evapotranspiration at its surrounding land, especially in spring. The evaporation at Hongze Lake is 4.61 mm/d in spring, which is comparable to that of summer (4.70 mm/d). However, the evapotranspiration in the region around Hongze Lake is obviously lower. It illustrates that in this region the evaporation capacity significantly exceeds the actual evapotranspiration, implying a high risk of drought. Moreover, the simulated mean monthly evapotranspiration from 1979 to 2003 (not shown here) shows that in the region of Hongze Lake this significant disparity mainly occurs from April to June. It is consistent with the fact that this region frequently experienced spring-summer drought (Chen et al., 2013).

The mean monthly evapotranspiration simulated from 1979 to 2003 is spatially averaged over the basin and depicted as Fig. 4-10, composed of bare soil evaporation, canopy interception evaporation, and plant transpiration. The 25-year-averaged mean annual evapotranspiration is 686 mm/a, which matches well the mean annual evaporation (673 mm/a) from 1980 to 2011 estimated by Global Land Evaporation Amsterdam Model (GLEAM). In the study of Yang et al. (2005), the accuracy and applicability of the GLEAM evapotranspiration data has been verified based on the water balance in the Huaihe basin.

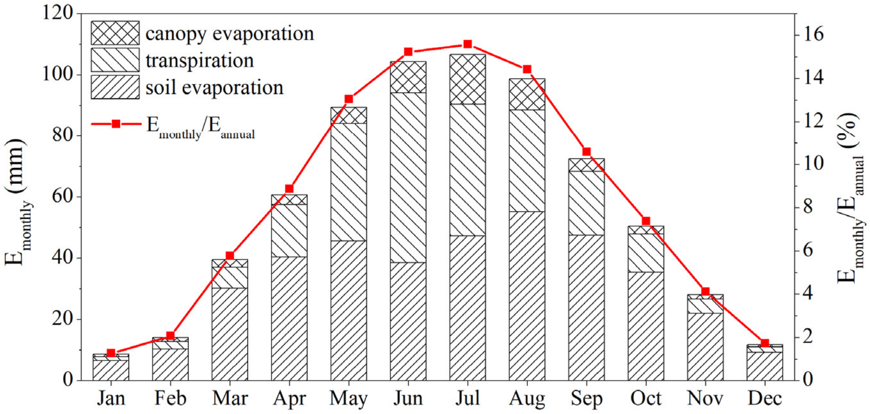

Fig. 4-10 Mean monthly evapotranspiration amount ($E_{monthly}$) in the Huaihe basin from 1979 to 2003 with the detailed amounts for various components, and the percentage of monthly to annual evapotranspiration ($E_{monthly}/E_{annual}$).

As shown in Fig. 4-10, The highest amount of evapotranspiration occurs in summer (June–August), which accounts for 45% of annual evapotranspiration. The evapotranspiration in spring is higher than that in autumn, and they contribute 28% and 22% to annual evapotranspiration, respectively. It slightly differs the GLEAM data (Yang et al., 2015), where the evapotranspiration in summer, spring, autumn, and winter occupies 40.4%, 28.4%, 21.4%, and 9.7%, respectively.

From the height of the bars corresponding to those contributions (Fig. 4-10), it is noticed that the sum of canopy interception evaporation and plant transpiration, which refers to canopy evapotranspiration, shows higher inter-monthly variations than that of soil evaporation. Statistically, the standard deviation of canopy evapotranspiration from March to November is 0.72, which is almost twice that of bare soil evaporation (0.32). This implies that the monthly variability of total evaporation in the Huaihe basin is strongly affected by plant evaporation and canopy interception evaporation. Researches (Bastiaanssen et al., 1998; Yang et al., 2015) illustrates that monthly variability of canopy evapotranspiration is associated with the growth period of vegetation and crops in the Huaihe basin.

4.4.3 Groundwater

Underground hydrological processes are an essential part of water cycling, and the groundwater in aquifers is one of the most important water sources within the watershed. The spatiotemporal variation of groundwater table and the water storage in aquifers affect hydrological processes through altering water balance.

(1) Spatial distribution

Fig. 4-11 shows the height (above the sea level) and the depth (i.e. the distance from the ground surface) of the mean groundwater table from 1979 to 2003 in the Huaihe basin simulated by the AHMS. As depicted in Fig. 4-11(a), there is relatively high groundwater table in the mountainous regions of the basin and relatively low water table in the plains; the groundwater table near rivers is especially lower. This spatial pattern of groundwater height enables it to laterally transport within the basin, gradually converging to rivers and lakes. As shown in Fig. 4-11(b), the groundwater table in the mountains is far below the land surface with a depth exceeding 20 m, while relatively shallow groundwater table is spotted in the downstream plains, at the foothills of the western mountains as well as in its adjacent plains.

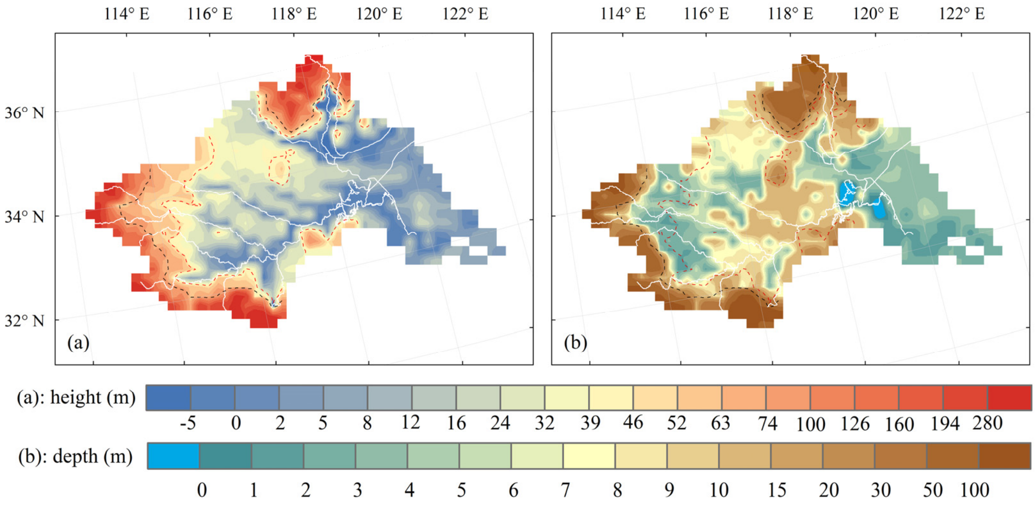

Fig. 4-11 Spatial distribution of the height (a) and the depth (b) of mean groundwater table in the Huaihe basin simulated from 1979 to 2003. Black and red dash isohypses denote the terrain height of 100 and 50 m, respectively.

(2) Temporal variability

The simulated groundwater table from 1979 to 2003 is averaged by season and the whole simulation period, and the differences between the seasonal averages and the mean are shown in Fig. 4-12. In it, the positive (negative) sign of a deviation signifies that the seasonal groundwater table locates above (below) the mean one, and the magnitude represents the distance between them.

As shown in Fig. 4-12, the deviation's extent in the mountains is small, implying that the seasonal variation of groundwater table in the mountains is insignificant. That is because atmospheric and surface hydrological processes rarely involves deep groundwater. On the contrary, pronounced seasonal variability occurs in the plains, and there is highest groundwater table in autumn and the lowest in spring. On the other hand, the groundwater near rivers is frequently recharged or discharged, which is reflected by the strong seasonal fluctuations of the deviation magnitudes in the adjacent-river areas (see in Fig. 4-12).

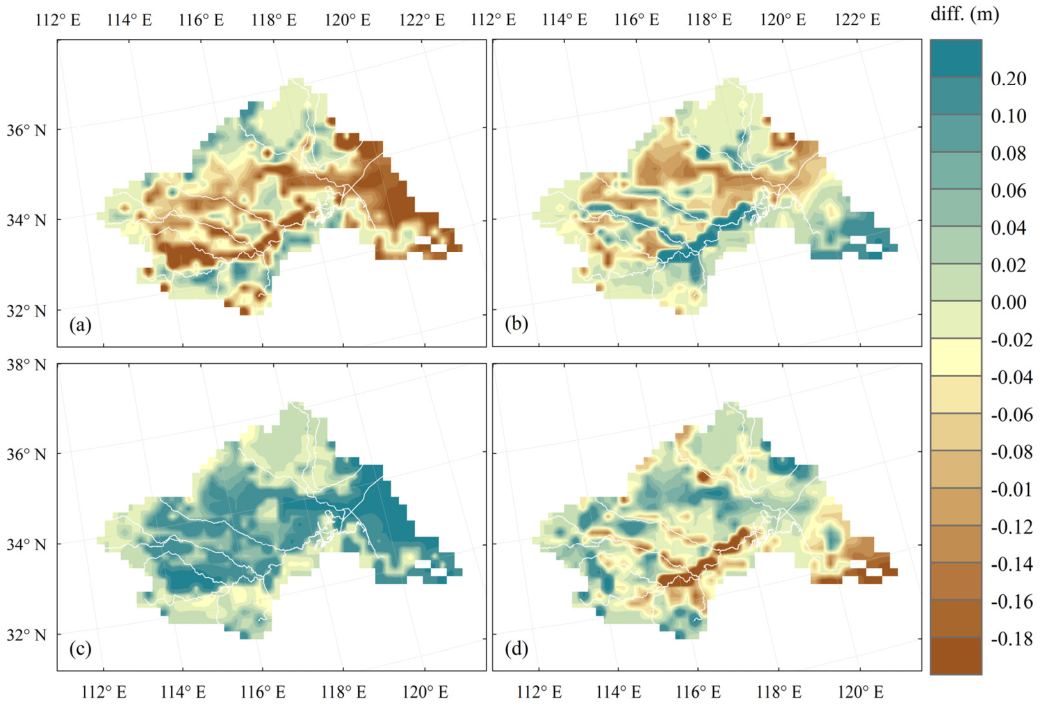

Fig. 4-12 Deviation of the mean seasonal groundwater table from the mean groundwater table: (a) spring, (b) summer, (c) autumn, and (d) winter. Both are taken from the simulation from 1979 to 2003.

The soil water storage in an unconfined aquifer includes the unsaturated soil water in the vadose zone and the saturated soil water below the groundwater table. Fig. 4-13 gives the correlation between monthly net precipitation and the corresponding change of soil water storage in the Huaihe basin estimated from the simulation.

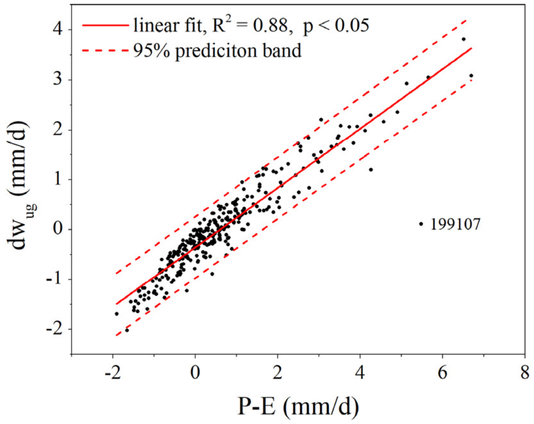

Fig. 4-13 The correlation between monthly net precipitation (P-E) and monthly change of soil water storage in the aquifer (dw_{ug}) in the Huaihe basin simulated from 1979 to 2003.

The result shows that the soil water storage change is highly linear correlated with the net precipitation, with a determination coefficient of 0.88 and a statistical significance less than 0.05. It illustrates that on monthly scale, the net precipitation within the basin largely determines the change of soil water storage in the aquifer.

The monthly mean of the net precipitation, soil water storage change, and groundwater depth are shown in Fig. 4-14. Consistent with the seasonal variability of groundwater table in the non-mountainous regions, the spatially averaged lowest and highest groundwater table occurs in spring and autumn, respectively. The variation of monthly mean soil water storage is associated with the change of monthly mean net precipitation. In July, the soil water storage dramatically increases in response to a large amount of net precipitation; conversely, the water storage decreases in April and May when the corresponding net precipitation is negative. The soil water storage slightly changes in other months when a relatively small amount of net precipitation occurs. It thus can be known that the inter-month variation of soil water storage in the aquifer agrees with that of net precipitation.

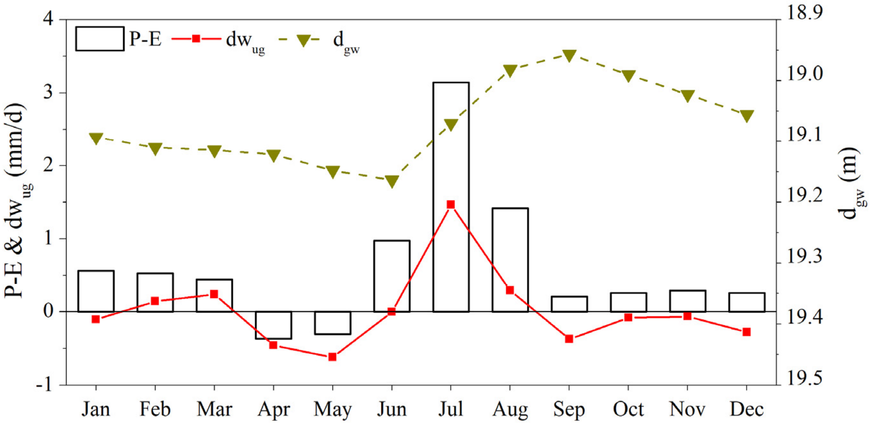

Fig. 4-14 The monthly mean net precipitation (P-E), the change of soil water storage in the aquifer (dw_{ug}), and groundwater depth (d_{gw}) simulated from 1979 to 2003 in the Huaihe basin.

As shown in Fig. 4-14, the change of soil water storage in the aquifer fluctuates with the varying net precipitation. Whereas, the groundwater table shows a gentle variation pattern. Following positive net precipitation from June to August, the groundwater table uplifts from June to September, and then gradually decreases. As a result of it, the groundwater table reaches a maximum in September, and reduces to a minimum in June. Accordingly, the soil water storage in aquifers responses to climate variability timely in the Huaihe basin, while groundwater table varies relatively slowly.

4.4.4 Runoff

In the NoahMP-HMS simulation, total runoff is defined as the sum of surface runoff and the aquifer-channel interactive water flux. The seasonal mean surface runoff (a1–d1), the interactive flux between groundwater and stream water (a2–d2), and the ratio of total runoff to precipitation (a3–d3) are shown in Fig. 4-15. The surface runoff is taken as negative (as shown in Fig. 4-15(a1–d1)) when the evaporation of water surface exceeds the precipitation. The positive interactive flux is taken as the groundwater seepage to streams, while the negative flux is the leakage of river water to groundwater (as shown in Fig. 4-15(a2–d2)).

(1) Spatial distribution

Despite the seasonal changes of runoff amount (will be discussed hereafter), the surface runoff and underground runoff within the Huaihe basin are differently characterized in term of spatial distribution (a1–d1, a2–d2). Surface runoff exists in the whole basin, but particularly high in the southern region of the Huai River and in the mountains (see Column 1 of Fig. 4-15). Groundwater seepage mainly occurs at the foothills of the mountains and in the plains, especially over the adjacent-river regions (see Column 2 of Fig. 4-15).

Fig. 4-15(a3–d3) shows the seasonal change of the ratio of mean runoff to mean precipitation. The ratios in four seasons share a common characteristic: high ratio over the mountains and in the southern region of the Huai River, and low in the remaining areas. On the other hand, in the region along the rivers where groundwater seepage occurs fiercely, the runoff coefficient is high especially in autumn and winter (≥ 0.6). Overall, the runoff coefficient in the southern region of the Huai River is high in summer (0.4–0.5). It can be explained by the intensive precipitation in summer and the runoff over hillslope regions where adequate conditions are provided for its genesis. This high runoff coefficient implies a severe flood risk, especially when extremely intense rainfall occurs in this region.

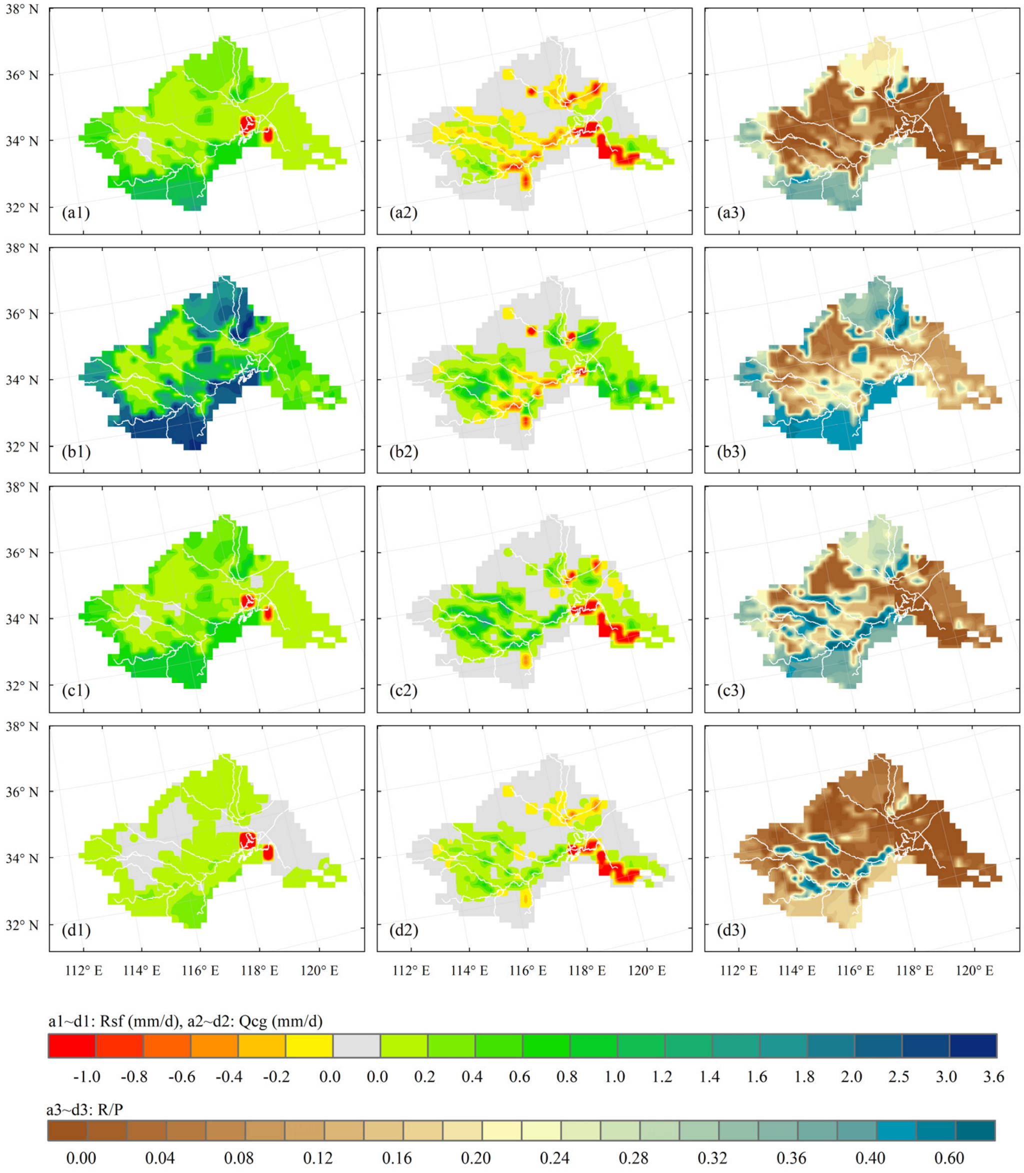

Fig. 4-15 Spatial and temporal distribution of the mean simulated surface runoff (R_{sf}, a1–d1), groundwater-stream water interactive flux (Q_{cg}, a2–d2), and runoff-precipitation ratio (R/P, a3–d3) in spring, summer, autumn, winter from 1979 to 2003 in the Huaihe basin. Positive value in a2–d2 represents the flow from groundwater to stream, or vice versa.

(2) Temporal variability

From Fig. 4-15(a2–d2), it can be known that the groundwater seepage mainly exists in the up-to-middle stream area; and the groundwater seepage itself from the aquifer to rivers is higher in summer and autumn, but lower in winter. In spring, a reverse flux from river to the aquifer dominates due to the lower groundwater table. The groundwater seepage continually happens from summer to winter, which shows a lower seasonal variability compared to surface runoff (see in Fig. 4-15(a1–d 1) and (a2–d2)). However, the magnitude of groundwater seepage is evidently lower than that of surface runoff. Hence, the river runoff in the Huaihe basin majorly stems from the surface runoff resulted from rainfall events.

To visualize the temporal variation of runoff, spatially averaged mean monthly surface runoff and total runoff are calculated and depicted in Fig. 4-16 as well as their contributions to the annual runoff. The surface runoff in summer months (JJA) is significantly higher than those in other seasons, which altogether contributes 66% of annual surface runoff. The generation of surface runoff during winter is limited, only accounting for 3% of annual surface runoff. The surface runoff in spring and autumn are approximately identical, which explains 15% and 16% to the annual surface runoff, respectively. As surface runoff dominates the runoff in the Huaihe basin, its temporal variability largely determines that of total runoff. Similar to surface runoff, a majority of annual runoff occurs in summer months (JJA), secondly in autumn and spring.

In spring, a reverse flux from rivers to the aquifer dominates (see in Fig. 4-14(a2–d2)) due to the lower groundwater table. As a result, the spatially average of total runoff in the basin are smaller than surface runoff in spring months and in June, as shown in Fig. 4-16. In autumn and winter, the river leakage mostly occurs in the river section between Hongze Lake and the mouth of the Yangtze River. And in winter the magnitude of river leakage is comparable to that of surface runoff generated in the upstream areas. On spatially average, the consumption of river leakage exceeds the amount of winter runoff. In this case, the total runoff in winter is negative, as shown in Fig. 4-16.

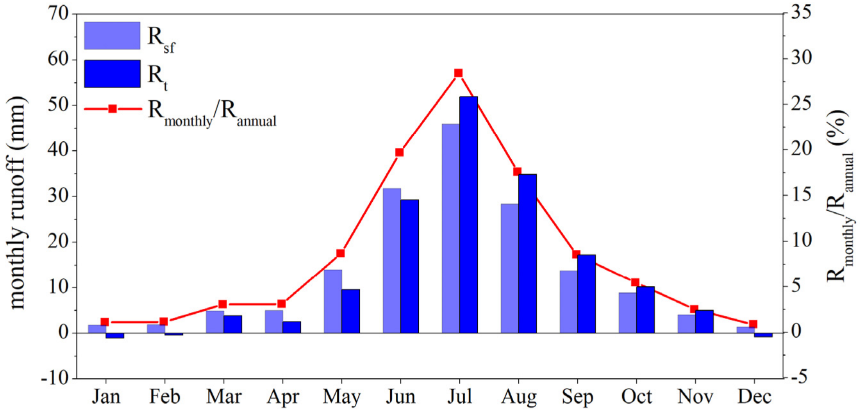

Fig. 4-16 Mean monthly surface runoff (R_{sf}) and total runoff (R_t) simulated from 1979 to 2003 in the Huaihe basin, and the percentage of monthly to annual surface runoff ($R_{monthly}/R_{annual}$).

According to the precipitation and the simulated runoff in the Huaihe basin from 1979 to 2003, the correlation of monthly precipitation and monthly runoff is investigated, as shown in Fig. 4-17(a). A nonlinear relationship is found between monthly mean runoff and monthly mean precipitation, with a determination coefficient of 0.93 and a significance less than 0.05. Mainly because surface runoff varies nonlinearly with the change of precipitation amount and its intensity.

As shown in Fig. 4-17(b), the tendency of monthly runoff is consistent with the precipitation. The standard deviation of monthly-annual ratio of runoff (10.4) is higher than that of precipitation (6.2), which indicates a higher temporal variability of runoff than that of precipitation in the Huaihe basin. The long-term hydrological simulation in the Huaihe basin shows that the mean runoff coefficient is about 0.08, 0.24, and 0.18 in spring, summer, and autumn, respectively (see in Fig. 4-17(b)).

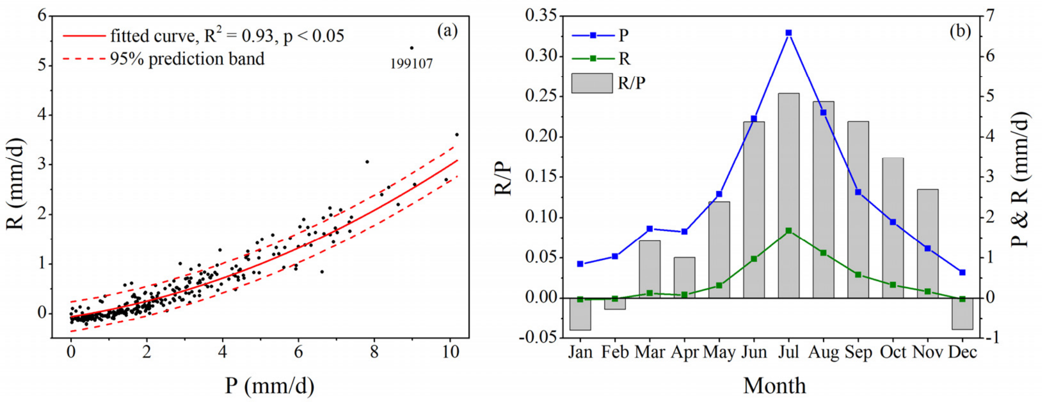

Fig. 4-17 (a) The correlation of monthly precipitation and monthly runoff from 1979 to 2003 in the Huaihe basin; (b) mean monthly precipitation (P) and mean total runoff (R) in the Huaihe basin as well as corresponding runoff-precipitation runoff (R/P).

4.5 Conclusion

In this chapter, the coupled land surface and hydrological model (NoahMP-HMS) is successfully applied to the Huaihe basin in China. The land surface and hydrological simulation is driven by the surface meteorological data from the NCEP reanalysis dataset (except precipitation) and the precipitation observation of meteorological stations.

Based on the formulation of infiltration capacity and infiltration-excess runoff for a homogeneous grid, a new parameterization of hillslope runoff is proposed to take the impact of hillslope topography in runoff into account. The implementation of this new parameterization in the model provides a modified scheme to calculate infiltration and surface runoff. The NoahMP-HMS simulations from 1980 to 1987 using the original scheme and the modified one are compared to the observations. The comparison shows:

1) Using the parameterization developed here, simulated annual runoff in the subbasin of WJB, LTZ, and BB approaches to the observation, with relative biases lower than 6%; the long-term water balance dynamic in the basin is well simulated. Without this parameterization, the NoahMP-HMS underestimates the runoff amounts in these subbasins (their relative biases to the observations exceed 60%); and the soil water storage in the basin is significantly increased, which is unreasonable from the long-term water balance dynamic perspective. It is because the latter neglecting the influence of hillslope topography results in excessively high rainwater infiltration, which thereby constrains the occurrence of infiltration-excess runoff.

2) The incorporation of the hillslope runoff parameterization into the NoahMP-HMS enables it to capture daily observed river discharges in a high accuracy, regarding both intensity and timing. The efficiency coefficients (NSIs) of simulated daily streamflow at the hydrological station of WJB, LTZ, and BB are 0.67, 0.81, and 0.80, respectively, and their water balance indexes (WBIs) are close to 1.0 (0.90–1.16).

3) Consequently, the hillslope runoff parameterization significantly enhances the production of surface runoff. By including this enhancement in runoff estimates, the NoahMP-HMS has a great ability to reproduce the hydrological processes and terrestrial water balance in the Huaihe basin.

The land surface and hydrological processes in the Huaihe basin from 1979 to 2003 are simulated using the validated NoahMP-HMS. According to this long-term simulation, the spatiotemporal variability of the hydrological processes in the Huaihe basin is investigated, as well as the hydrological response to climate variability. Key outcomes are:

4) The precipitation in the Huaihe basin presents a high spatial and temporal variability. The mean annual precipitation from 1979 to 2003 is 912 mm/a in the Huaihe basin. In the Meiyu season, heavy rainfall from June to August is obtained in the Huaihe basin due to the associated monsoon rain band over eastern China, which accounts for 53% of the annual precipitation. The precipitation in the basin decreases from southeast to northwest, with higher precipitation in the southern region of the Huai River and in the downstream plains.

5) The total evaporation increases southeastward over the Huaihe basin, with the

lowest in the northern mountains and the highest in the downstream plains (southeastern part). The 25-year-averaged evapotranspiration in the basin is 686 mm/a, and the evapotranspiration in summer, spring, and autumn accounts for 45%, 28%, and 22%, respectively. The simulated mean annual evapotranspiration and its seasonal distribution match with those deduced from the GLEAM data. The monthly variation of total evapotranspiration is largely attributed by vegetation evapotranspiration, which is associated with the growth period of vegetation and crops in the basin.

6) Over the basin, relatively shallow groundwater table is found at the foothills of the mountains and in the plains. The groundwater in the non-mountainous regions shows a large seasonal variability, with the highest groundwater table in autumn and the lowest in spring. The mean groundwater table in the basin increases from June to September due to a large amount of net precipitation in summer, and then decreases gradually from October to next June. As a result, the mean groundwater table reaches a maximum in September, and reduced to a minimum in June.

7) The river runoff in the Huaihe basin is composed of surface runoff and groundwater seepage to streams, where the surface runoff dominates. A small amount of groundwater seepage continuously and stably occurs at the foothills of mountains and in the plains, while the surface runoff shows a large spatial and temporal variability. The monthly runoff in the basin is largely determined by monthly precipitation, but the runoff shows a larger monthly variation than that of precipitation. The runoff coefficient in the southern region of the Huai River is large in summer, ranging from 0.4 to 0.5, which implies a high flood risk caused by the intense rainfall in this region.

5 Application of the AHMS

In the previous chapter, the coupled land surface and hydrological model (NoahMP-HMS) exhibits its capability of reproducing hydrological processes. The new hillslope runoff parameterization in the model enhance the reliability for the prognostication of hydrological variables which are crucial for describing regional water balance. Hence, this new parameterization and the parameter values used in the NoahMP-HMS simulation are used in this chapter. Herein, the distributed hydrological model HMS is integrated into the Weather Research and Forecasting (WRF) Model to form an integrated model called the coupled Atmospheric and Hydrological Modelling System (AHMS). The evaluation for the performance of the AHMS is carried out, according to the coupled simulation from July to November 1991 in the Huaihe basin. In the AHMS, the hydrological processes can interact with the land surface processes, which further feedbacks to the atmosphere; to investigate its effect on surface fluxes and on atmospheric variables, a comparison is conducted with the stand-alone WRF simulation.

5.1 Model setup and experiment design

The Huaihe basin experienced a severe flood in June and July 1991 (Shi et al., 1992), and followed by a drought in autumn (Bao et al., 2011). A simulation involved atmospheric and hydrological processes by the AHMS is used to reproduce these extreme hydrological events. The coupled simulation uses the same domain setup as in the offline NoahMP-HMS simulation (see in Section 4.2), with a period from July 1 to November 30, 1991. The time resolutions of the WRF and the hydrological simulation are 90 seconds and 30 minutes, respectively. The configuration of the AHMS is mentioned below in detail.

The global reanalysis data from NECP Climate Forecast System Reanalysis (CFSR) is used to provide atmospheric boundary conditions every 6 hours. Numerous studies showed that the performance of the WRF simulation is sensitive to physics parameterization schemes (Berg et al., 2013; Fersch and Kunstmann, 2014). Based on the sensitivity analysis (not demonstrated herein), the following physics schemes are selected for the WRF simulation: the WRF Single-Moment five-class scheme (WSM5) microphysical parameterization, the Betts-Miller-Janjic scheme (BMJ), the Yonsei University (YSU) parameterization for the planetary boundary layer, the MM5-Dudhia shortwave scheme, and the Rapid Radiative Transfer Model (RRTM) longwave radiation scheme. Due to the coupling approach, the Noah-Multiparameterization Land Surface Model (Noah-MP LSM) is used as the land surface parameterization scheme.

In addition to the standard WRF setup, surface and subsurface hydrological conditions are needed to specify in the AHMS. The land surface parameter dataset (No. 13–20 in Table 4.2) and the hydrological characteristic dataset (No. 22–27 in Table 4.2) used in the NoahMP-HMS simulation are also adopted. This AHMS simulation uses identical values of the Manning roughness coefficient (No. 28 in Table 4.2) and the hydraulic conductance (No. 29 in Table 4.2) as in the offline simulation.

The simulated groundwater head and water level on July 1, 1991 in the offline NoahMP-HMS simulation are used to initialize the groundwater head and water level of rivers and lakes in this simulation.

Table 5.1 Model configuration for the coupled atmospheric and hydrological simulation (R_{AHMS}) and the stand-alone atmospheric simulation (R_{WRF})

Run	boundary condition in the multi-layer soil model	hydrological modules		
		GW2D	RT2D	GCI
R_{AHMS}	Darcy-flux	yes	yes	yes
R_{WRF}	free drainage	no	no	no

GW2D: two-dimensional groundwater model, RT2D: two-dimensional terrestrial hydrological model, GCI: interaction of groundwater and channel water.

Apart from the AHMS simulation, a stand-alone WRF simulation is also performed in the Huaihe basin as a control experiment. The model configurations in the coupled atmospheric and hydrological simulation (R_{AHMS}) and the stand-alone atmospheric simulation (R_{WRF}) are presented in Table 5.1. The use of Darcy-flux boundary condition in the multi-layer soil model (in the Noah-Multiparameterization Land Surface Model) and the activation of hydrological modules in the AHMS allows a fully coupled atmospheric and hydrological simulation (R_{AHMS}). The simulation by the WRF (R_{WRF}), uses the free drainage boundary condition (i.e. gravitational drainage) by which the soil water in LSM drains downwards under the effect of gravity. Furthermore, the land surface and atmospheric processes in R_{WRF} is not affected by the hydrological processes.

The R_{AHMS} experiment starts at 0000 UTC on July 1, 1991 and ends at 2400 UTC on November 30, 1991. The simulated groundwater table, water level in rivers and lakes, and soil moisture on July 1, 1991 in the NoahMP-HMS simulation are used for the initial conditions in the AHMS simulation. The R_{WRF} experiment starts at 0000 UTC on July 1, 1991 as a restart run to have the same initial conditions as in the AHMS simulation. The results in the two simulations (i.e. R_{WRF} and R_{AHMS}) from July 3 to November 30, 1991, excluding the spin-up of the first two days, are used for the comparative analysis as following.

5.2 Statistical evaluation

To evaluate the AHMS performance in the coupled atmospheric and hydrological simulation of the Huaihe basin, the model verification is carried out regarding the accuracy of the estimates of temperature, precipitation, and streamflow. For the validation of these variables, some publicly available observational datasets and the reanalysis product are used.

For temperature and precipitation, monthly global precipitation and air temperature at 0.5^{o} resolution from University of Delaware (UDel; Willmott and Matsuura, n.d.) are used. For precipitation, global monthly precipitation with a spatial resolution of 0.5^{o} from the Global Precipitation Climatology Centre (GPCC; Schneider et al., 2011) are additionally used. Regarding rainfall, it was found that GPCC as well as UDel represents the mean and variability of rainfall throughout the series from 1979 to 2000; in relation to the air temperature standards, the precision of UDel was low, but the accuracy was moderate (Tostes et al., 2017). For air temperature, 6-hourly NCEP/NCAR reanalysis global dataset with T62 Gaussian grid is used. Moreover, the observed daily river discharge over the period of July to November 1991 at the hydrological station of WJB, LTZ, and BB are employed to compare with the simulated daily streamflow by the AHMS. The locations of these hydrological stations in the Huai River are shown in Fig. 4-2.

5.2.1 Precipitation estimates

The simulated precipitation in the Huaihe basin from July to November 1991 in R_{AHMS} and R_{WRF} are spatially and monthly averaged, and the results are shown in Table 5.2(top). Monthly precipitation observation from the UDel and the GPCC are spatially averaged and used for statistical evaluation. In Table 5.2(top), the observed precipitation from meteorological stations in the period of July to November 1991 is also included, as well as their anomaly to the mean monthly precipitation from 1979 to 2003.

As listed in Table 5.2(top), the monthly precipitation in July 1991 is obviously higher than the mean precipitation of July, with an anomaly percentage of 36.5%; in comparison to the 25-year-averaged monthly precipitation, there is a significantly lower amount of precipitation in October and November 1991, with an anomaly percentage of -94.0% and -67.4%, respectively.

Table 5.2(bottom) presents the statistical evaluation for simulated total precipitation in the period of July to November 1991. Both the AHMS and the stand-alone WRF overestimate the amount of total precipitation over the period by 1–5% upon the validation dataset. For instance, the relative bias of total precipitation of the AHMS simulation to the UDel is 4.33%, and 4.27% for the WRF simulated precipitation. Their relative biases to the GPCC dataset are about 1.0%, and about 1.5% relative to the meteorological observation. This shows that the WRF itself fairly describes the amount of precipitation in the basin over the period.

The monthly precipitation simulated by the AHMS are generally higher than its counterpart in the UDel during the period, i.e. 21.7 mm (9%) in July, 4.4 mm (3%) in August, -6.8 mm (-7%) in September, 0 mm in October, and 2.0 mm (19%) in November. When comparing to the GPCC monthly precipitation, the AHMS underestimates the precipitation by 17.4 mm (-6.2%) in July, but overestimates the precipitation by 23.4 mm (26.3%) in August; from September to November, simulated monthly precipitation fluctuates around the observation. Comparing to the precipitation observation from meteorological sites, there is a bias of -15.5 mm (-5.6%) in July and 26.3 mm (21.6%) in August in the R_{AHMS}, while the absolute bias is small from September to November.

In addition, the difference of simulated monthly precipitation in the AHMS and the WRF simulation is -1.6, 0.8, 0.5, 0.1, and 0.4 mm/month from July to November, respectively. Obviously, the simulated monthly precipitation amount by the AHMS and the WRF are nearly identical in the Huaihe basin during the period.

Table 5.2 (top) Monthly precipitation (mm) in the AHMS simulation (R_{AHMS}), the WRF simulation (R_{WRF}), the UDel dataset, the GPCC dataset, and the observation; (bottom) total precipitation bias in the period of July to November 1991 in the Huaihe basin.

Month	R_{AHMS} (mm)	R_{WRF} (mm)	UDel (mm)	GPCC (mm)	P_{obs} (mm)	P_{mean} (mm)	anomaly (%)
July	263.1	264.7	241.4	280.5	278.6	204.1	36.5
Aug	148.1	147.3	143.7	120.1	121.8	142.6	-14.6
Sep	91.4	90.9	98.2	96.3	93.8	78.8	19.0
Oct	1.7	1.6	1.7	3.0	3.5	58.4	-94.0
Nov	12.4	12.0	10.4	11.4	11.3	36.9	-67.4

P_{obs}: monthly precipitation observation of meteorological sites, P_{mean}: mean monthly precipitation observation from 1979 to 2003, anomaly = $(P_{obs} - P_{mean})/P_{mean}*100\%$.

	abs. bias	rel. bias		abs. bias	rel. bias
	mm/month	%		mm/month	%
R_{AHMS}-UDEL	4.29	4.33	R_{WRF}-UDEL	4.23	4.27
R_{AHMS}-GPCC	1.10	1.08	R_{WRF}-GPCC	1.04	1.02
R_{AHMS}-Obs	1.55	1.52	R_{WRF}-Obs	1.49	1.46

5.2.2 Air temperature estimates

The near-surface air temperature is treated in the same way as the precipitation in the section above, but compared to the UDel dataset and the NCEP reanalysis dataset. Table 5.3(top) lists the monthly mean air temperature from July to November 1991 simulated by the AHMS and the WRF, and the monthly mean temperature in the UDel dataset and in the NCEP reanalysis product. Table 5.3(bottom) presents the statistical evaluation for simulated mean air temperature in the period of July to November. Over the period, the simulated mean temperature by the AHMS and the WRF are lower than the measured temperature of the UDel data, with an absolute bias of -1.22 and -0.95 °C, respectively, while higher than the NCEP temperature, with an absolute bias of 0.55 and 0.82 ºC. It shows that the selected WRF setup is able to predict mean air temperature.

Since the NECP reanalysis data is used to provide atmospheric boundary conditions, the simulated monthly mean temperature is further compared to the NCEP data (see in Table 5.3). Both the AHMS and the WRF overestimate air temperature from July to November while comparing to the NCEP monthly mean temperature. In these five months, the bias ranges from 0.1 to 0.8 ºC in the AHMS simulation, while those are in the range of 0.4 to 1.2 ºC in the WRF simulation (as shown in Table 5.3(top)). It illustrates that the AHMS performs better in simulating near-surface air temperature in the Huaihe basin.

Table 5.3 (top) Monthly mean air temperature (ºC) of the AHMS simulation (R_{AHMS}), the WRF simulation (R_{WRF}), the UDel data set, the NECP reanalysis data; (bottom) the bias of monthly mean air temperature in the Huaihe basin over the period of July to November 1991.

Month	R_{AHMS}	R_{WRF}	UDel	NCEP	R_{AHMS}-NCEP	R_{WRF}-NCEP
July	26.4	26.5	28.1	25.8	0.6	0.7
Aug	24.9	25.1	26.0	24.5	0.4	0.6
Sep	21.1	21.4	22.2	21.0	0.1	0.4
Oct	15.3	15.7	16.3	14.5	0.8	1.2
Nov	8.7	9.0	9.7	7.8	0.9	1.2

	abs. bias	rel. bias		abs. bias	rel. bias
	ºC	%		ºC	%
R_{AHMS}-UDEL	-1.22	-5.97	R_{WRF}-UDEL	-0.95	-4.66
R_{AHMS}-NCEP	0.55	2.92	R_{WRF}-NCEP	0.82	4.36

5.2.3 Streamflow estimates

Fig. 5-1 depicts the observed daily river discharge and the simulated daily streamflow at the hydrological station of WJB, LTZ, and BB from July 1 to November 30, 1991, as well as the daily precipitation in the corresponding subbasins.

According to the observation (red solid line in Fig. 5-1), there are two flood peaks during the period. The first flood peak occurs at the WJB station on July 8, 1991 with a peak discharge of 5790 m^3/s, and reaches the LTZ station on July 11 with a discharge of 7350 m^3/s, and then arrives at the BB station on July 13 with a discharge of 7750 m^3/s. In the R_{AHMS} (blue solid line of Fig. 5-1), the flood occurring at the WJB station in July is not well captured. On July 3, the simulated streamflow (3110 m^3/s) at the WJB station almost equals to the observed river discharge (3160 m^3/s). Subsequently, the latter river discharge increases to a peak value of 5790 m^3/s on July 8, while the former decreases gradually. In the AHMS simulation, the timing of the flood at the station of LTZ and BB in July are well captured, however, the simulated flood discharge is lower.

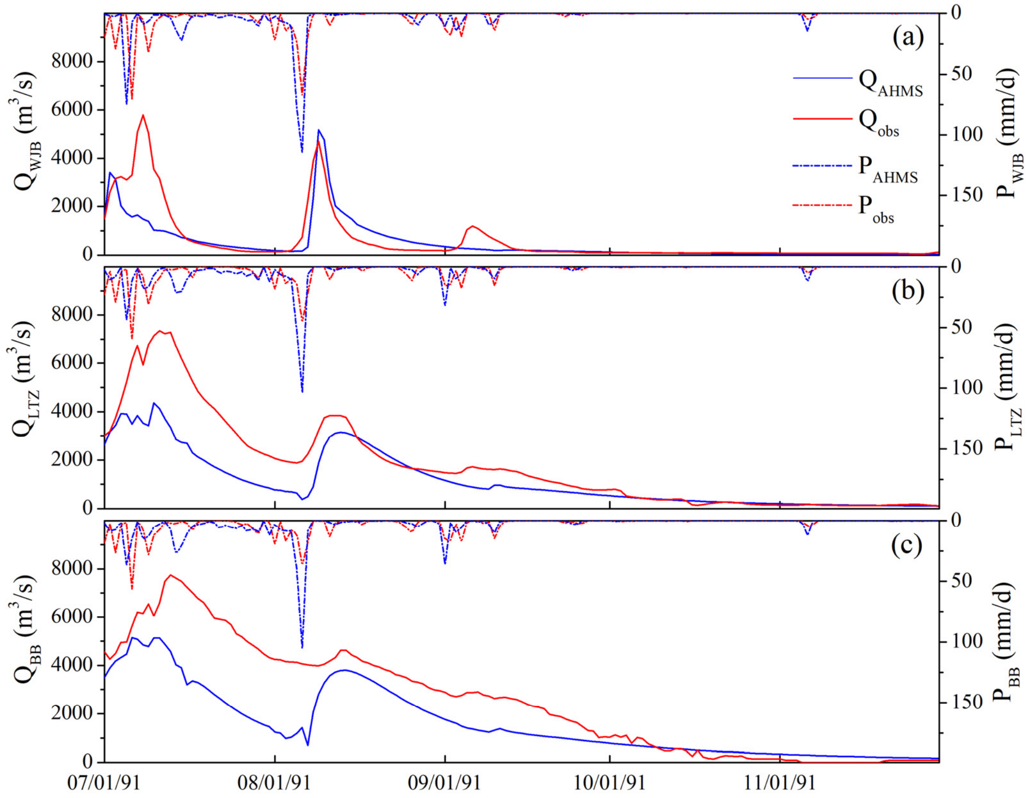

Fig. 5-1 Time series of observed (Q_{obs}) and simulated (Q_{AHMS}) daily streamflow by the AHMS from July 1 to November 30, 1991 at the hydrological station of WJB (a), LTZ (b), BB (c), as well as the simulated daily precipitation by the AHMS (P_{AHMS}) and the observed daily precipitation of the meteorological sites (P_{obs}) in the corresponding basins.

As shown in Fig. 5-1 (red solid lines), the second flood peak occurs at the WJB station on August 9, 1991 with a 4710 m^3/s discharge, and arrives at the LTZ station on August 12 with a 3840m^3/s discharge, and then reaches the BB station on August 13 with a 4630 m^3/s discharge. As a whole, the second flood in August 1991 is well simulated by the AHMS. The simulated flood peak also occurs on August 9 with a discharge of 5179 m^3/s (with a relative bias of 10% to the observation). Although slightly lower than the observation, the simulated daily streamflow in August at the LTZ and BB station match the observed hydrograph. In addition, the simulated daily streamflow by the AHMS during the low flow periods shows a good agreement with the observations at the three hydrological stations, as depicted in Fig. 5-1.

With the observation and the simulation, the performance of AHMS in simulating daily streamflow is evaluated using the Nash-Sutcliffe coefficient of efficiency index (NSI), the Pearson product-moment correlation coefficient (PMC), and the Water Balance Index (WBI), as shown in Table 5.4. The definitions and calculation formulations for these statistical indices are shown in Appendix 7.2.

Table 5.4 Statistical evaluation of simulated daily streamflow by the AHMS

Station	R_{AHMS}		
	NSI	PMC	WBI
WJB	0.57	0.76	0.79
LTZ	0.59	0.90	0.63
BB	0.54	0.88	0.63

Table 5.4 shows that the correlation coefficients (PMC) between the simulated and the observed daily streamflow are 0.76, 0.90, and 0.88 at the WJB, LTZ, and BB station, respectively. It illustrates that the simulated daily streamflow and the observation at the station of LTZ and BB is highly correlated in timing; as shown in Fig. 5-1, the AHMS captures the temporal variation of observed daily river discharge at the station of LTZ and BB. At the WJB, LTZ, and BB station, the water balance index (WBI) values between the simulated and the observed daily streamflow are 0.79, 0.63, and 0.63, and the efficiency coefficients (NSI) are 0.57, 0.59, and 0.54, respectively. Accordingly, the AHMS has an ability of reasonably modelling daily hydrological processes in the Huaihe basin.

5.3 Influence on surface soil hydrological processes

In the AHMS, the hydrological model is integrated into the WRF via the land surface model (Noah-MP LSM). Specifically, the four-layer soil model in the Noah-MP LSM (the thickness is 0.1m, 0.3m, 0.6m, and 1.0m, respectively) is coupled with the groundwater model by Darcy-flux boundary condition and soil water characteristic curve (see details in Section 3.7). Thus, the surface soil water of the soil model domain (i.e. 0–2 m from the land surface) in the Noah-MP LSM can interact with deeper unsaturated soil water and groundwater. It can then be argued that the surface soil hydrological processes are supposed to be impacted by hydrological processes, and the influence is associated with its relative location of groundwater table.

In general, groundwater table changes slowly. As illustrated in Fig. 4-12, the seasonal variation of groundwater table in the Huaihe basin is insignificant, mostly ranging from -0.18 m to 0.20 m. Therefore, the location of groundwater table in the AHMS simulation is determined principally by initial conditions, and it fluctuates slightly over the simulation period. Fig. 5-2 shows the height (relative to the sea level) and the depth (the distance from the surface) of mean groundwater table in the period of July to November 1991 within the Huaihe basin simulated by the AHMS.

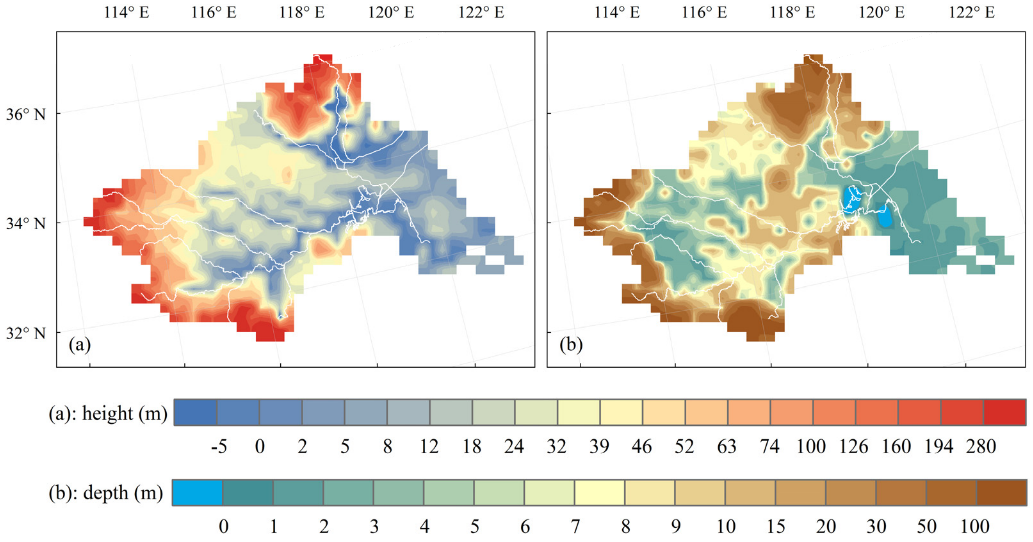

Fig. 5-2 Spatial distribution of the height (a) and the depth (b) of mean groundwater table over the period of July to November 1991 in the Huaihe basin simulated by the AHMS.

As shown in Fig. 5-2(b), the depth of groundwater table in the mountains is obviously higher than other regions, which is thus categorized as deep groundwater region. To highlight the influence of shallow groundwater, regions with shallow groundwater table are investigated individually. In this study, shallow groundwater is a condition where the groundwater table is less than 2 meters from the land surface, i.e. the groundwater table is located within the LSM soil model domain. In addition, once the groundwater depth exceeds 10 m, the upward capillary flux rarely occurs at the bottom boundary of LSM soil domain in the AHMS simulation. Hence, regions with groundwater depth between 3 and 10 m are treated as relatively deep groundwater region. The groundwater depth of 3 m is selected as the lower limit to ensure that the groundwater table is located below the LSM soil model domain over the simulation period.

Therefore, the comparison of surface soil hydrological processes in the AHMS simulation (marked as RAHMS in the following contents) and in the WRF simulation (RWRF) is conducted, respectively, in the deep groundwater region, in the relatively deep groundwater region, and in the shallow groundwater region. The fluxes at the top and the bottom of LSM soil model domain are the upper and the lower boundary conditions for simulating the dynamics of surface soil moisture. The flux at its lower boundary is called recharge flux with positive downwards. A positive recharge value means a drainage (downwards) from LSM soil layers to deeper soil column; a negative recharge is a capillary moisture flux (upwards) into LSM soil layers from deeper soil column. At the upper boundary (i.e. ground surface), the sum of infiltration, soil evaporation, and plant transpiration is called net infiltration (positive downwards). A positive value of net infiltration is the net amount of water infiltrated into soil from the upper boundary, while a negative value is the net amount of water evaporated from soil.

5.3.1 In the deep groundwater region

Fig. 5-3 shows the spatially averaged monthly mean fluxes at the upper (a, i.e. net infiltration) and the lower boundary (b, i.e. recharge flux) of LSM soil model domain for the deep groundwater region, and the change of surface soil water (c) in RAHMS and RWRF, as well as the deviation between RAHMS and RWRF. As shown in Fig. 5-3(b), the monthly mean recharge fluxes from July to November and daily mean recharge fluxes (not shown) are positive in both simulations. It demonstrates that in the deep groundwater region downward drainage occurs at the bottom of LSM soil model domain, no matter which boundary condition is used. Owing to the free drainage boundary condition in RWRF, downward gravitational drainage happens regardless of soil moisture and groundwater depth. In RAHMS, the Darcy-flux boundary condition in the LSM soil model allows for bidirectional flux at the lower boundary, but only minor upward flux (about -0.02 mm/d) is spotted in a small percentage (6%) of the deep groundwater regions. It implies that deep groundwater seldomly moisten surface soil by capillary rise.

For regions with deep groundwater table, the dynamics of surface soil moisture in LSM soil model domain is determined by net infiltration at its upper boundary and recharge flux at its lower boundary. Besides in September, the surface soil water storage decreases from July to November (as shown in Fig. 5-3(c)), which results from a larger amount of soil drainage than net infiltration in these four months. In September, net infiltration slightly exceeds soil drainage, leading to a small increment in surface soil water. Overall, the surface soil water storage exhibits a decreasing trend during the simulation period. It is demonstrated in Fig. 5-4, which shows the time series of mean soil moisture of LSM soil model domain (i.e. four soil layers) in the deep groundwater region for RAHMS and RWRF.

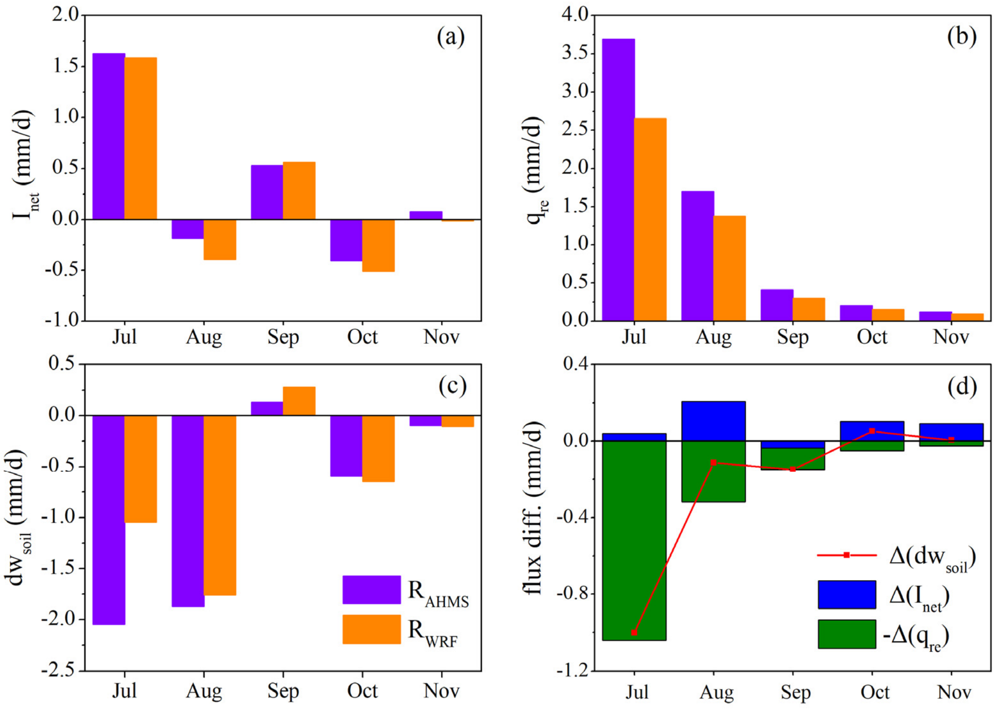

Fig. 5-3 Comparisons of spatially averaged monthly mean net infiltration (a, denoted by I_{net}), recharge flux (b, q_{re}), and the change of soil water in the LSM soil model domain (c, dw_{soil}) in the deep groundwater region for RAHMS and RWRF, as well as the difference between RAHMS and RWRF (d, marked as Δ).

As shown in Fig. 5-4, the soil moisture in RAHMS and RWRF decreases markedly during the first two months (i.e. July and August), and the soil moisture in RAHMS declines more rapidly. As a result, the soil moisture in RAHMS (0.25 m^3/m^3) becomes apparently lower than RWRF (0.27 m^3/m^3) at the end of August. In the following months, the soil moisture in RAHMS and RWRF changes gradually, with a stable deviation between them (about 0.02 m^3/m^3). As the initial conditions are identical in RAHMS and RWRF, it can be argued that the difference of soil moisture between them mainly stems from surface soil hydrological processes, especially in July and August.

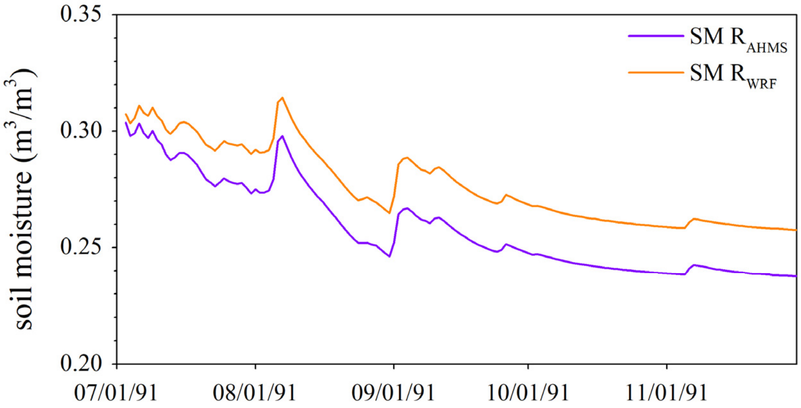

Fig. 5-4 Time series of mean soil moisture of four soil layers in the deep groundwater region for R_{AHMS} and R_{WRF}.

The combination of water balance equations (see in Appendix 7.1) in LSM soil model domain for R_{AHMS} and R_{WRF} gives $\Delta(dw_{soil}) = \Delta(I_{net}) - \Delta(q_{re})$, where Δ means the difference of R_{AHMS} and R_{WRF}, dw_{soil} is the change of surface soil water storage, I_{net} is the net infiltration, q_{re} is the recharge flux. This equation illustrates that the difference of soil water change between R_{AHMS} and R_{WRF} can be explained by their difference in net infiltration (at the upper boundary) and recharge flux (at the lower boundary), as shown in Fig. 5-3(d).

According to Fig. 5-3(c), the surface soil water in R_{AHMS} is reduced by 2.05 and 1.87 mm/d in July and August, and reduced by 1.05 and 1.76 mm/d in R_{WRF}. It is to say that the reduction of surface soil water in R_{AHMS} is higher than in R_{WRF} in July (e.g. $\Delta(dw_{soil}) = -1.0$ mm/d) and August (e.g. $\Delta(dw_{soil}) = -0.11$ mm/d). As shown in Fig. 5-3(a), the difference of net infiltration between R_{AHMS} and R_{WRF} is positive in July ($\Delta(I_{net}) = 0.04$ mm/d) and August ($\Delta(I_{net}) = 0.21$ mm/d), which indicates a larger amount of water into soil from the upper boundary in R_{AHMS}. The comparison of recharge flux in Fig. 5-3(b) demonstrates that the soil drainage of LSM soil model domain is more intense in R_{AHMS} in comparison to R_{WRF} (e.g. $\Delta(q_{re}) = 1.05$ mm/d in July and 0.13 mm/d in August).

Based on the detailed data above, it can be known that the proportion of recharge flux difference to the surface soil water change difference exceeds 100%, i.e. $-\Delta(q_{re})/\Delta(dw_{soil}) > 100\%$, in July and August. This is to say that more substantially reduced soil moisture in R_{AHMS} compared to R_{WRF}, is caused by the more intense soil drainage that occurs at the lower boundary of LSM soil model domain.

5.3.2 In the relatively deep groundwater region

The surface soil processes are not directly impacted by relatively deep groundwater (3–

10 m depth) that is located beneath the LSM soil model domain. And in R_{AHMS}, only a small amount of saturation-excess runoff (0.01 mm/d) occurs in August in the relatively deep groundwater regions. Therefore, the soil water dynamics in the LSM soil model domain is determined by net infiltration at its upper boundary and recharge flux at its lower boundary. Fig. 5-5 depicts the spatially averaged monthly mean net infiltration (a), recharge flux (b), and the change of surface soil water (c) in the relatively deep groundwater region.

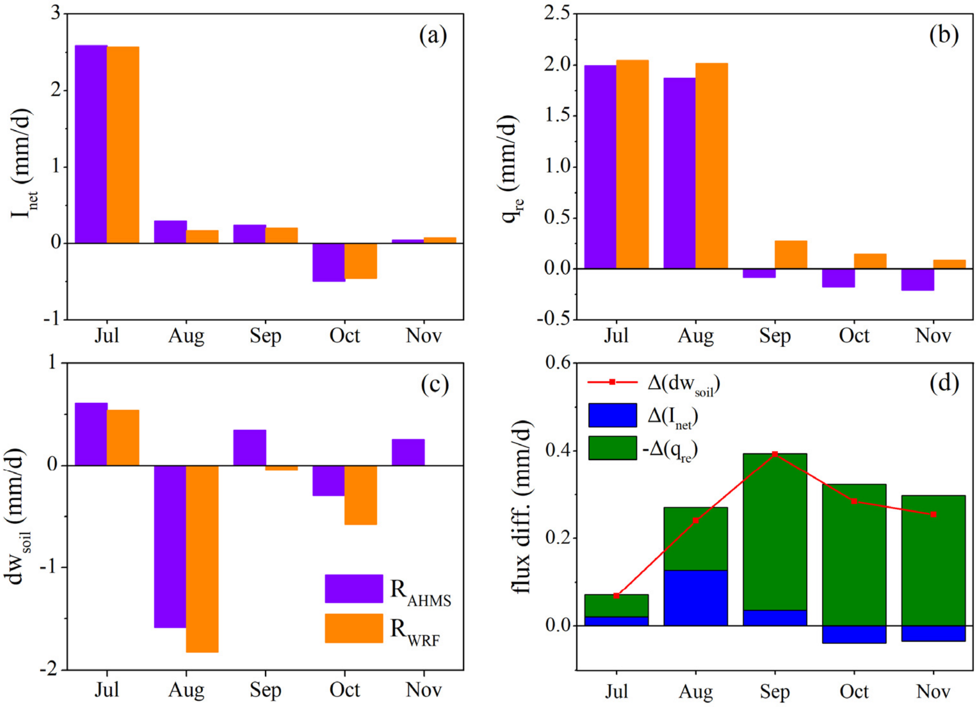

Fig. 5-5 Comparisons of spatially averaged monthly mean net infiltration (a, denoted as I_{net}), recharge flux (b, q_{re}), and the change of soil water in LSM soil model domain (c, dw_{soil}) in the relatively deep groundwater region for R_{AHMS} and R_{WRF}, as well as the difference of R_{AHMS} and R_{WRF} (d, marked as Δ).

Monthly recharge flux remains positive (downwards) in R_{WRF} from July to November owing to the free drainage boundary condition, while negative recharge fluxes (upwards) are spotted in R_{AHMS}. Their detailed statistics are listed in Table 5.5. The negative flux at the bottom of LSM soil model domain means that deep soil water and/or groundwater move upwards by capillary rise, and recharge surface soil moisture. As shown in Table 5.5, in R_{AHMS} upward recharge flux occurs in the relatively deep region, especially from September to November; due to their wide occurrence, the monthly recharge in this region is negative (upwards) in these three months. It illustrates that the soil water in the LSM soil model domain can be sufficiently recharged by capillary fluxes from groundwater or deep soil, when groundwater table is relatively deep.

Table 5.5 Statistical calculation for monthly recharge in the relatively deep groundwater region.

Year-Month	RAHMS		RWRF
	area percentage (%) with negative recharge flux	upward flux (mm/d)	area percentage (%) with negative recharge flux
1991-07	42	-0.3324	0
1991-08	33	-0.3335	0
1991-09	65	-0.3234	0
1991-10	78	-0.2889	0
1991-11	85	-0.2632	0

Fig. 5-6 shows the time series of mean soil moisture of four soil layers and mean soil moisture of the bottom layer in the relatively deep groundwater region for RAHMS and RWRF. As shown in Fig. 5-6, the soil moisture in RAHMS and RWRF almost overlaps in July and August: it increases from 0.29 m^3/m^3 on July 3 to 0.34 m^3/m^3 on August 7, and drastically decreases to 0.27 m^3/m^3 on August 31, 1991. From September, the soil moisture remains stable (about 0.27 m^3/m^3) in RAHMS, while still declines slowly in RWRF. Hence, the soil moisture in RAHMS is increasingly higher than that in RWRF, and their difference enlarges gradually from 0.005 to 0.018 m^3/m^3 from September to November. This amplification of soil moisture deviation exists more evidently in the bottom soil layer (see dashed line in Fig. 5-6).

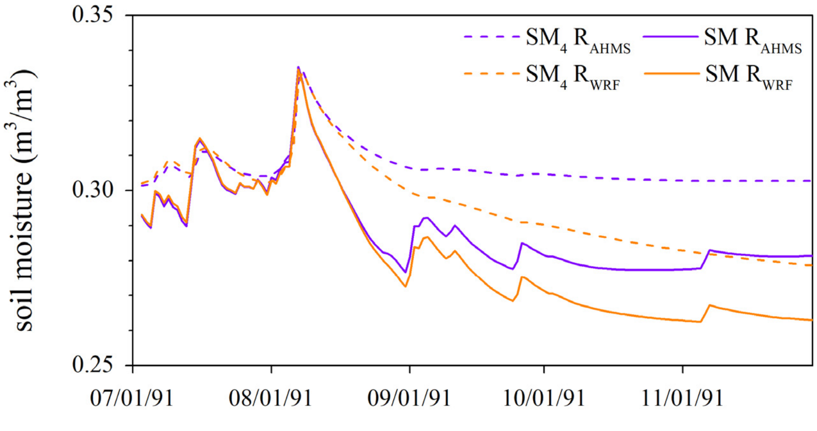

Fig. 5-6 Time series of mean soil moisture of four soil layers (SM) and of bottom layer (SM4) in relatively deep groundwater region for RAHMS and RWRF.

As shown in Fig. 5-5(c), in RWRF the surface soil water (i.e. in LSM soil model domain) is reduced by 0.05 mm/d in September, 0.58 mm/d in October, and increased by 0.002 mm/d in November; in RAHMS the surface soil water is increased by 0.34 and 0.26 mm/d in September and November, and reduced by 0.30 mm/d in October. Thus, the difference of the change of surface soil water between RAHMS and RWRF is positive from September to November, i.e. $\Delta(dw_{soil})$ is 0.392, 0.284, and 0.254 mm/d, respectively. As shown in Fig. 5-5(d), from September to November monthly net infiltration differs slightly in RAHMS and RWRF, e.g. $\Delta(I_{net})$ is 0.036, -0.039, and -0.035 mm/d, respectively. As depicted in Fig. 5-5(b), from September to November monthly recharge fluxes are positive (downwards) in RWRF, while they are negative (upwards) in RAHMS. By contrast, the difference of recharge flux between RAHMS and RWRF is negative in these three months, e.g. $\Delta(q_{re})$ is -0.358, -0.323, and -0.297 mm/d, respectively.

Accordingly, the calculation of $-\Delta(q_{re})/\Delta(dw_{soil})$ shows that the difference of recharge flux explains 91% of the change of surface soil water change in September, and more than 100% in October and November. It implies that the higher soil moisture in RAHMS from September to November results from the upward fluxes at the bottom of LSM soil model domain, while only downward gravitational drainage occurs in RWRF.

5.3.3 In the shallow groundwater region

Fig. 5-7 shows the time series of mean soil moisture of four soil layers in the LSM soil model domain in the shallow groundwater region for RAHMS and RWRF, as well as the time series of mean groundwater depth in RAHMS. The mean groundwater depth is constantly less than 2 m, indicating that the groundwater table in this region is mostly located within the LSM soil column.

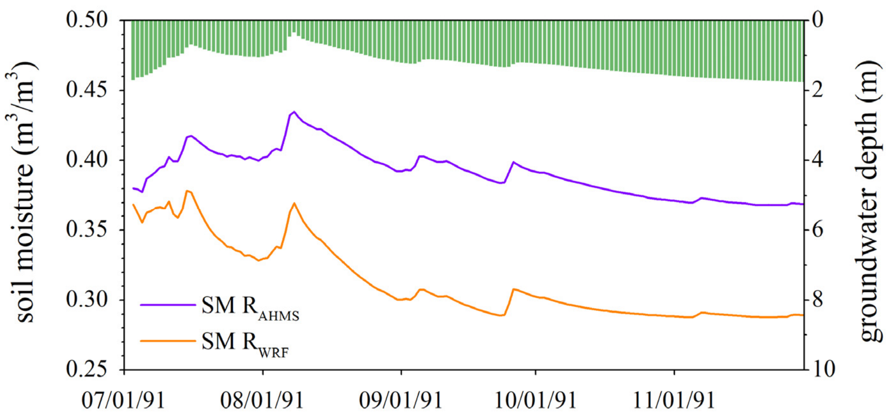

Fig. 5-7 Time series of mean soil moisture of four soil layers in the relatively shallow groundwater region for RAHMS and RWRF, as well as the mean groundwater depth in RAHMS.

As shown in Fig. 5-7, the soil moisture increases before early August and slightly decreases in mid-to-late August in RAHMS, while in RWRF it shows an obviously decreasing trend in July and August. In this case, their difference increases to 0.09 m^3/m^3 at the end of August, despite the soil moisture in RAHMS and RWRF are more or less same on July 3, 1991. Afterwards, the soil moisture declines slowly in both simulations. On spatially and temporally average, the soil moisture is 0.31 and 0.39 m^3/m^3 in RWRF and RAHMS, respectively, which shows an increased soil moisture by 26% in RAHMS. It can thus be assumed that the simulations of surface soil water in RAHMS and RWRF are strongly differentiated for shallow groundwater region.

In RAHMS, surface soil hydrological processes involve groundwater, and groundwater can interact with water in rivers and lakes. Especially when the groundwater table is shallow (depth < 2 m), surface soil water in the LSM soil model domain can be directly impacted by groundwater. Thus, the unsaturated and saturated soil water in aquifers is viewed as a whole in RAHMS, impacted by net infiltration, saturation-excess runoff, and interactive flux between groundwater and channel water. In RWRF groundwater is not involved, and hence the dynamics of surface soil water is determined by net infiltration at its upper boundary and recharge flux at its lower boundary. Fig. 5-8 depicts the spatially averaged monthly means related to the water balance of the LSM soil model domain in RWRF (a) and that related to the water balance of the aquifer in RAHMS (b).

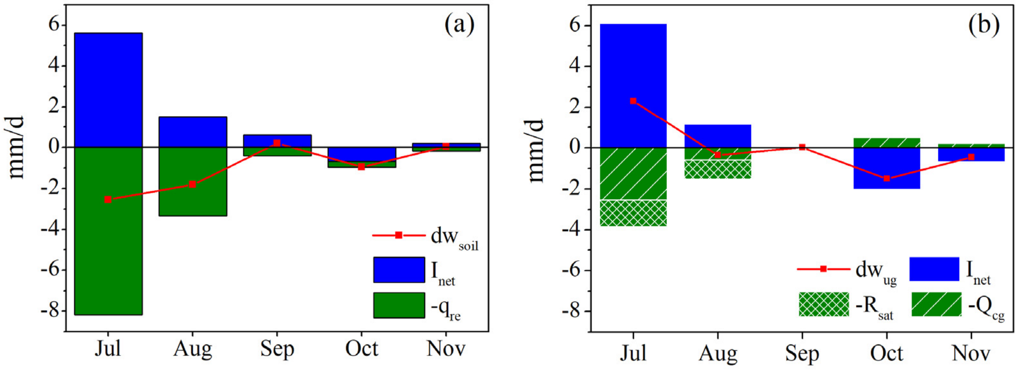

Fig. 5-8 (a) Water budget of the LSM soil model domain in RWRF, including net infiltration (I_{net}), recharge flux (q_{re}), and the change of soil water (dw_{soil}), (b) water budget of the unconfined aquifer in RAHMS, including net infiltration (I_{net}), saturation-excess runoff (R_{sat}), groundwater-channel water interactive flux (Q_{cg}), and the change of soil water in the aquifer (dw_{ug}).

In RWRF, the soil drainage at the bottom of the LSM soil model domain exceeds the net infiltration at its top in July and August, as shown in Fig. 5-8(a). It must lead to a reduction of surface soil water in the LSM soil model domain, which explains why the soil moisture in RWRF shows a decreasing trend in these two months (see in Fig. 5-7).

Compared to R_{WRF}, there is slightly different net infiltration in July and August for R_{AHMS}, but significantly less water drained from the aquifer. Specifically, the recharge flux in R_{WRF} is 8.16 and 3.33 mm/d, respectively; in R_{AHMS}, the sum of saturation-excess runoff and groundwater seepage is 3.83 and 1.53 mm/d (see in Fig. 5-8(b)). Consequently, the soil water storage of aquifers in R_{AHMS} is increased by 2.30 mm/d in July and decreased by 0.36 mm/d in August, while the surface soil water in R_{WRF} is significantly decreased in July (-2.53 mm/d) and August (-1.81 mm/d). It can be known that with a large amount of net infiltration, the surface soil hydrological processes in the shallow groundwater region are differentiated in R_{AHMS} and R_{WRF}. In R_{WRF}, intense soil drainage is simulated at the lower boundary of the LSM soil model domain at the same time. Different from R_{WRF}, infiltration water accumulates in the aquifer and laterally flows in R_{AHMS}; if the aquifer is fully saturated, saturation-excess runoff occurs during the rainfall events.

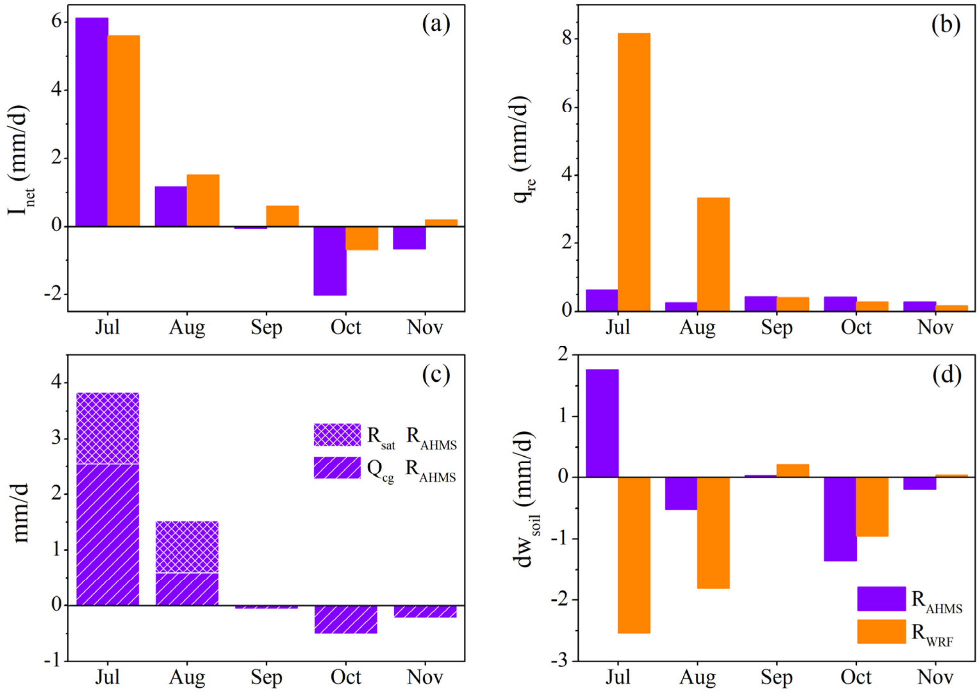

Fig. 5-9 Comparisons of spatially averaged monthly mean net infiltration (a, signified as I_{net}), recharge flux (b, q_{re}), saturation-excess runoff (R_{sat}) and groundwater-surface water interactive flux (c, Q_{cg}), and the change of surface soil water (d, dw_{soil}) in the shallow groundwater region for R_{AHMS} and R_{WRF}.

Fig. 5-9 depicts the spatially averaged monthly means for various components in the water budget of the LSM soil model domain for R_{AHMS} and R_{WRF}, including net infiltration at its upper boundary (a), recharge flux at its lower boundary (b), and the change of surface soil water (d), and saturation-excess runoff and interactive flux between groundwater and channel water (c). In July and August, the monthly recharge flux is 0.64 and 0.26 mm/d in RAHMS, while 8.16 and 3.33 mm/d in RWRF, respectively. The contrast suggests that the drainage at the bottom of the LSM soil model domain in RAHMS is considerably confined in comparison to RWRF. It is because when groundwater table is located above the bottom of the LSM soil model domain, the gravitational drainage at its bottom ceases. In July and August, therefore, the change of surface soil water is 1.76 and -0.52 mm/d in RAHMS, respectively, while -2.53 and -1.81 mm/d in RWRF, respectively. This also elaborates why the surface soil moisture of July and August increases in RAHMS, however, decreases in RWRF.

Accordingly, it can be known that in RWRF the drainable water can be released from the LSM soil model domain under gravity. Apparently, it is unreasonable in the case of shallow groundwater table. The embedment of groundwater in the AHMS enables soil water to accumulate above groundwater table, which results in significantly higher soil moisture in the shallow groundwater region.

5.3.4 Section Conclusion

The analysis mentioned above shows that the surface soil hydrological processes is affected by the hydrological processes, in which case the simulation of soil moisture is altered in RAHMS. The influence of the coupled atmospheric and hydrological simulation on soil moisture is manifested by compared to RWRF, as shown in Table 5.6.

Table 5.6 Comparison of simulated soil moisture in RAHMS and RWRF for regions with various groundwater depths.

Year-Month	Deep groundwater			Relatively deep gw.			Shallow groundwater		
	RAHMS m^3/m^3	RWRF m^3/m^3	diff. %	RAHMS m^3/m^3	RWRF m^3/m^3	diff. %	RAHMS m^3/m^3	RWRF m^3/m^3	diff. %
1991-07	0.29	0.30	-4.19	0.30	0.30	-0.16	0.40	0.35	13.14
1991-08	0.27	0.29	-6.24	0.30	0.30	0.41	0.41	0.33	24.34
1991-09	0.26	0.28	-7.62	0.28	0.28	2.82	0.39	0.30	31.49
1991-10	0.24	0.26	-7.75	0.28	0.27	4.69	0.38	0.29	29.53
1991-11	0.24	0.26	-7.72	0.28	0.26	6.31	0.37	0.29	28.04
mean	0.26	0.28	-6.66	0.29	0.28	2.69	0.39	0.31	24.95

Note: Relative difference (%) = (RAHMS - RWRF)/RWRF × 100

In RAHMS, simulated soil moisture by the AHMS shows a reduction of 4–8% in the deep groundwater region, and an augment of 13–31% in the shallow groundwater region. For the relatively deep groundwater region, the mean soil moisture in RAHMS and RWRF is nearly the same in July and August, and in R_{AHMS}, the soil moisture from September to November is increased by 3–6%. The change of soil moisture in R_{AHMS} differs significantly in regions with various groundwater depths. It demonstrates that the impact of hydrological processes on soil moisture is associated with groundwater depth.

5.4 Influence on surface fluxes and atmospheric states

According to the previous section, the simulation for surface soil hydrological processes by the WRF and the AHMS differs, which must lead to altered soil moisture in two simulations. The change of surface soil moisture affects the processes at the land surface, and further feedbacks to atmospheric variables. In this section, the comparison between the AHMS and the WRF simulations within the Huaihe basin is undertaken, regarding soil moisture, evapotranspiration, near-surface air temperature, and precipitation.

5.4.1 Soil moisture

Fig. 5-10 shows the spatial distribution of mean soil moisture of four soil layers over the period of July 3 to November 30, 1991 in the Huaihe basin simulated by the AHMS (a, R_{AHMS}) and the WRF (b, R_{WRF}), as well as the corresponding difference of R_{AHMS} and R_{WRF}. The mean soil moisture that is averaged over the basin and over the period is increased by 6.7% in R_{AHMS}, from 0.29 (R_{WRF}) to 0.31 m^3/m^3 (R_{AHMS}). But, the soil moisture difference shows a large spatial variability, as shown in Fig. 5-10(c).

In a large portion of the basin (besides in the mountains), higher soil moisture is observed in R_{AHMS}. Combined with the spatial distribution of groundwater depth (Fig. 5-2(b)), it can be found that the soil moisture is obviously higher for R_{AHMS} in regions where groundwater depth is less than 3 m (red solid line in Fig. 5-10(c)). Spatially averaged over the downstream area with shallow groundwater (black dashed line in Fig. 5-10(c)), for example, the soil moisture difference of R_{AHMS} and R_{WRF} is 0.08 m^3/m^3, from 0.32 m^3/m^3 in R_{WRF} (the relative saturation is 70%) to 0.40 m^3/m^3 in R_{AHMS} (the relative saturation is 86%). The mean soil moisture in R_{AHMS} is increased by 25%. It is because in R_{AHMS}, in shallow groundwater regions the soil water can accumulate in the LSM soil model domain (above the groundwater table), instead of being drained downwards. As discussed in Section 5.3.1, higher soil drainage (in R_{AHMS}) than gravitational drainage (in R_{WRF}) occurs in the deep groundwater region, which results in drier soil conditions in the mountains in R_{AHMS}.

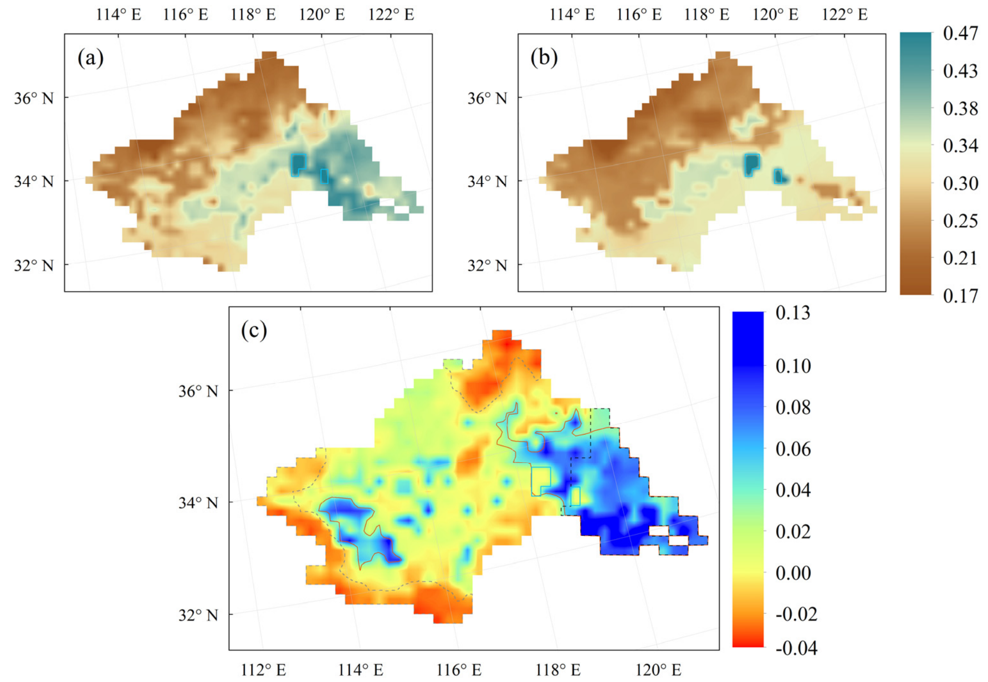

Fig. 5-10 Spatial distribution of mean soil moisture (m^3/m^3) over the period of July 3 to November 30, 1991 simulated by AHMS (a) and the WRF (b), and the corresponding difference (c) between RAHMS and RWRF. In this figure, the area framed by grey dashed line, red solid line, and black dashed line represents the mountainous regions, the regions with groundwater depth less than 3 m, and the downstream area of the Huai River, respectively.

5.4.2 Evapotranspiration

Fig. 5-11 shows the spatial distribution of mean evapotranspiration over the period of July 3 to November 30, 1991 within the Huaihe basin simulated by the AHMS (a) and the WRF (b), and the difference of RAHMS and RWRF. It can be seen from Fig. 5-11(a) and (b) that the evapotranspiration in RWRF shows a smaller spatial variation, while the spatially distributed evapotranspiration in RAHMS significantly differs within the Huaihe basin. Statistically, the evapotranspiration in RAHMS has a spatial standard deviation of 0.43, spatially varying in the range of 1.19 to 3.72 mm/d; apart from the evaporation of water surface (over lakes), the evapotranspiration in RWRF is less than 2.67 mm/d, with a spatial standard deviation of 0.21. It demonstrates that the simulated evapotranspiration by the AHMS shows a larger spatial variability.

On average, the simulated evapotranspiration by the WRF and the AHMS is 2.29 and 2.47 mm/d, respectively, indicating that evapotranspiration is increased by 8% (0.18 mm/d) in RAHMS. Similar to that of soil moisture difference, there is higher evaporation in RAHMS in a large part of area in the basin (see in Fig. 5-10(c)). Especially in the regions with groundwater depth less than 3 m, the difference mainly ranges from 0.23 (0.1 quantile) to 1.01 mm/d (0.9 quantile). In the downstream area with shallow groundwater, the spatially averaged evapotranspiration is increased by 35% (0.8 mm/d) in RAHMS. Conversely, the spatially averaged evapotranspiration in the mountains decreases from 2.28 mm/d in RWRF to 2.19 mm/d in RAHMS, showing a reduction of 0.09 mm/d (-4%) in RAHMS.

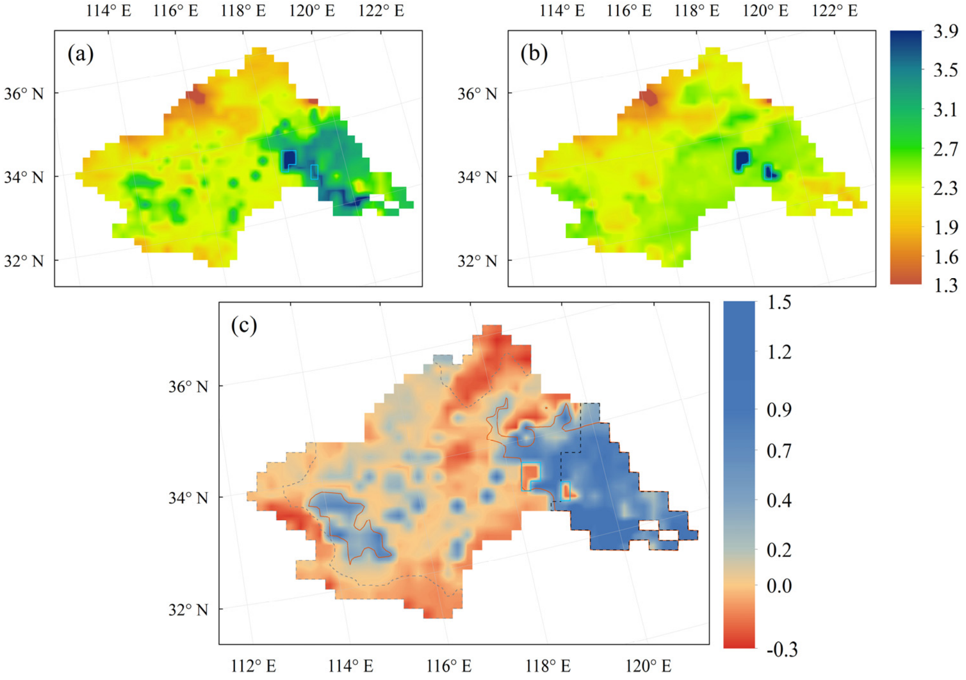

Fig. 5-11 Spatial distribution of mean evapotranspiration (mm/d) over the period from July 3 to November 30, 1991 simulated by the AHMS (a) and the WRF (b), and the corresponding difference (c) between RAHMS and RWRF. The representations of the lines in this figure are same as Fig. 5-10.

5.4.3 Air temperature

Fig. 5-12 shows the spatial distribution of mean air temperature over the period of July 3 to November 30, 1991 for the Huaihe basin simulated by the AHMS (a) and the WRF (b), and the corresponding difference (c) between RAHMS and RWRF. In RAHMS and RWRF, the mean air temperature that is averaged over the basin and over the period is 19.31 and 19.50 ºC, respectively, indicating that the air temperature in RAHMS is reduced by -0.19 ºC (0.96%). As shown in Fig. 5-12(c), a lower air temperature of RAHMS than RWRF is observed in 85% of the basin, especially in the regions with groundwater depth less than 3 m. It matches with the change of soil moisture and evapotranspiration. As same atmospheric boundary conditions are used in RWRF and RAHMS, the amounts of incoming radiation in both simulations are supposed to be identical. In RAHMS, higher soil water content in shallow groundwater regions enhances soil evapotranspiration, which consumes more heat energy. In the downstream areas, for instance, the spatially averaged air temperature decreases from 19.47 ºC in RWRF to 18.74 ºC in RAHMS, with a reduction of 0.73 ºC (-4%). Whereas, the spatially averaged air temperature in the mountains simulated by the AHMS (19.05 ºC) approximately equals to that in RWRF (19.06 ºC).

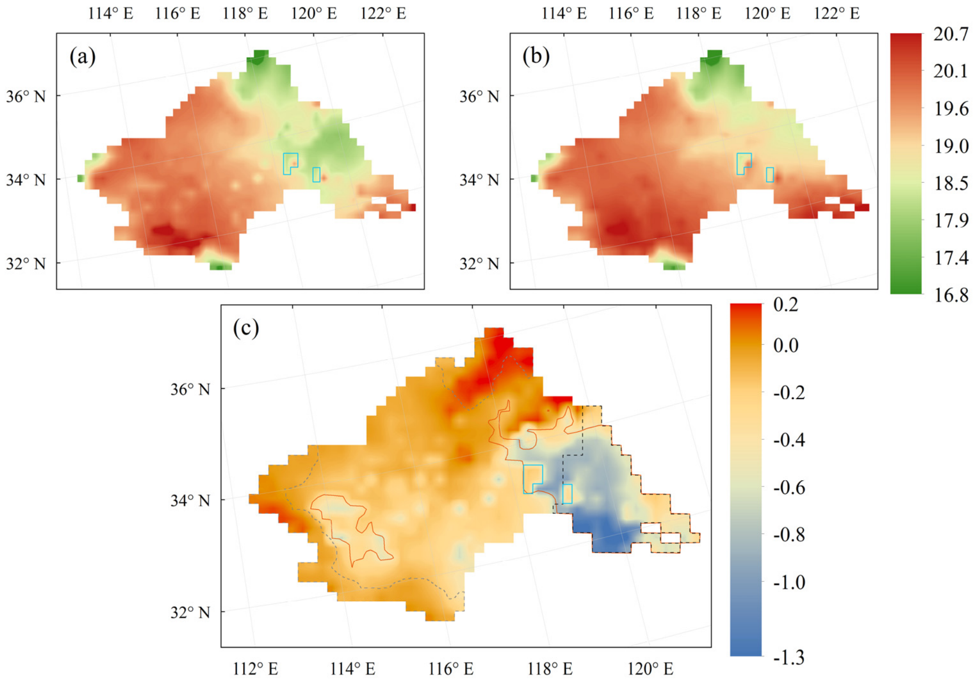

Fig. 5-12 Spatial distribution of mean air temperature (ºC) over in the period from July 3 to November 30, 1991 simulated by the AHMS (a) and the WRF (b), and the corresponding difference (c) between RAHMS and RWRF. The representations of the lines in this figure are same as Fig. 5-10.

5.4.4 Precipitation

Fig. 5-13 shows the spatial distribution of simulated precipitation over the period of July 3 to November 30, 1991 for the Huaihe basin in RAHMS (a), RWRF (b), and the corresponding difference (c) between RAHMS and RWRF. The amounts of mean precipitation over the basin from July to November are almost identical for RAHMS and RWRF, only with a difference of 0.06 mm/d. On monthly scale, this difference is also small, e.g. -1.6 mm in July, 0.8 mm in August, 0.5 mm in September, 0.1 mm in October, and 0.4 mm in November (see in Table 5.2). This indicates that the impact of hydrological processes on basin-averaged precipitation is minor.

In both simulations, intense precipitation occurs in the regions along the mainstream of the Huai River, while a relatively small amount of precipitation exists in the northern basin. But, as shown in Fig. 5-13(c), the spatially distributed differences between RAHMS and RWRF indicate regional changes up to ± 0.9 mm/d (± 30%). Hence, the spatial pattern of precipitation within the basin is redistributed in a certain extent in RAHMS compared to RWRF. But there is no general tendency of higher or lower precipitation amounts in RAHMS. Due to the fact that the initial conditions and the inflow of moisture at the domain boundaries is the same for both simulations, the spatial redistribution of precipitation within the basin can be attributed to the hydrological processes in RAHMS.

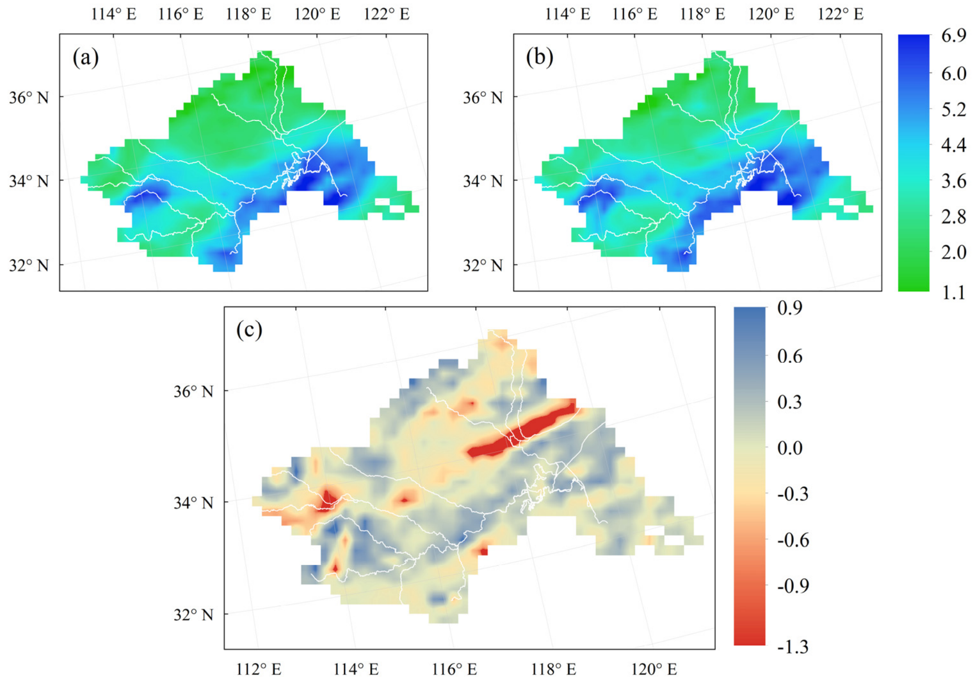

Fig. 5-13 Spatial distribution of mean precipitation (mm/d) over the period of July 3 to November 30, 1991 simulated by the AHMS (a) and the WRF (b), and the corresponding difference (c) between RAHMS and RWRF. The representations of the lines in this figure are same as Fig. 5-10.

5.5 Conclusion

The AHMS is applied to the Huaihe basin for a coupled atmospheric and hydrological simulation in the period of July 1 to November 30, 1991. In the fully coupled simulation, the AHMS enables surface and subsurface hydrological processes in the watershed to affect surface fluxes, and further feedbacks to atmospheric variables; whereas, this influence is not simulated in the atmospheric simulation of the stand-alone WRF. The evaluation with the observation dataset shows that the AHMS can performance well in the atmospheric modelling. The statistical evaluation indices for simulated daily streamflow at three hydrological stations (NSIs ≈ 0.55, PMCs = 0.76–0.90, WBIs = 0.63–0.79) demonstrate that the AHMS has an ability of reasonably reconstructing daily river discharge within the Huaihe basin.

The simulation of surface soil hydrological process in the LSM soil model domain in R_{AHMS} and R_{WRF} are discussed seperately. Furthermore, their water budgets are compared to quantitively analyze the impact of hydrological processes in the coupled simulation. It is worth noted that the surface soil hydrological processes in two simulations behaves differently, and the influence of surface and subsurface hydrological processes on it varies with groundwater depth. In details,

1) Deep groundwater, mainly located in the mountains, rarely supplies moisture to surface soil layers. Conversely, under suction of deep unsaturated soil and gravity effect, soil drainage occurring at the bottom of LSM soil model domain is higher than gravitational drainage (in WRF). It results in drier soil conditions in the mountains.

2) In the AHMS simulation, groundwater is capable of moistening overlaying soil layers by capillary rise. In relatively deep groundwater regions (3–10 m), upward capillary fluxes are widely spotted from September to November. After experiencing a dramatic decline in mid-to-late August, the soil water content simulated by the WRF continues to decrease slowly in the following three months, while the soil moisture in the AHMS simulation remains stable (about 0.27 m^3/m^3). It is mainly because of the wide occurrence of capillary fluxes, which efficiently provides moisture for surface soil layers in dry soil conditions.

3) The surface soil hydrological processes in shallow groundwater regions (0–2 m) strongly differs in both simulations. In the WRF simulation, gravitational drainage occurs at the bottom of soil model domain regardless of groundwater depth. In the AHMS, the description of groundwater in aquifers enables gravitational soil water to accumulate above the groundwater table. As a consequence, the simulated soil moisture of this region is significantly higher (by 26%) in the AHMS simulation.

The impact of the coupled atmospheric and hydrological simulation on soil moisture presents a large spatial variability, due to the spatial variation of groundwater depth in the basin. The change of soil moisture alters surface fluxes and atmospheric variables, e.g. evapotranspiration and air temperature; their shifts show a similar spatial pattern as that of soil moisture. For instance, soil moisture and evaporation in the downstream plains are increased by 25% and 35%, respectively, and near-surface air temperature is reduced by 0.73 ºC (4%). On average, the embedment of hydrological processes into the AHMS results in higher soil moisture (by 7%) and evaporation (by 8%), as well as lower air temperature (-0.2 ºC) in the Huaihe basin. Their effect on basin-averaged precipitation is insignificant, but results in a spatial redistribution of precipitation in the basin, with local changes up to ± 30%.

6 Discussion, Summary and Outlook

6.1 Discussion

The evaluation of the coupled Atmospheric and Hydrological Modelling System (AHMS) has been conducted in Chapter 5, while the validation of the coupled land surface and hydrological model (NoahMP-HMS) has been achieved in Chapter 4. The hydrological processes within the Huaihe basin in July 1991 have been simulated respectively by the AHMS (see in Section 5.2) and the NoahMP-HMS (see in Section 4.4).

In the NoahMP-HMS simulation and in the AHMS simulation, the setups for the land surface module and the hydrological module, and the values of the hydrological parameters are identical. Hence, Their difference results from the atmospheric conditions. The NoahMP-HMS is driven by 6-hourly NCEP reanalysis dataset (except precipitation) and the precipitation from meteorological stations, while in the AHMS simulation the WRF dynamic downscaling provides surface meteorological conditions. The simulated daily streamflow by both models at the BB station in the period of July 1 to July 31, 1991 are depicted in Fig. 6-1, as well as the observations.

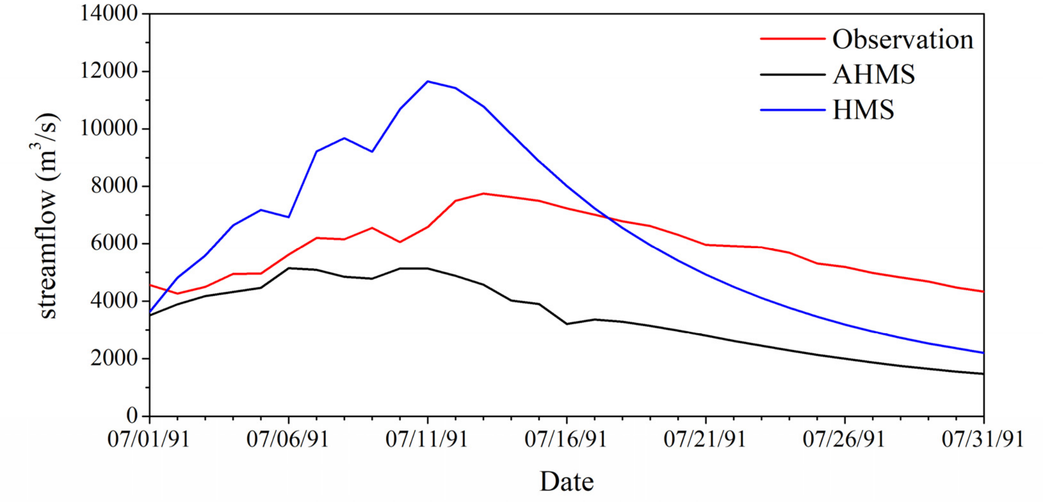

Fig. 6-1 Time series of observed and simulated daily streamflow by the NoahMP-HMS and the AHMS at the BB hydrological station.

According to the observed flood hydrograph (red line in Fig. 6-1) of the BB station, the river discharge gradually increases from July 1 to July 13 and then slowly decreases.

The simulated daily streamflow by the AHMS (black line in Fig. 6-1) is obviously lower than the observation. The water balance index is 0.59. It can be argued that the AHMS underestimates the amount of runoff in the BB subbasin in July 1991. As shown in Fig. 6-1 (blue line), the simulated streamflow by the NoahMP-HMS differs from the observed flood hydrograph. But its water balance index is 1.08, compared to the observation. It can be seen that the runoff amount in the BB subbasin during July 1991 is well simulated by the NoahMP-HMS. Therefore, combined with the NoahMP-HMS simulation, the underestimation of flood peak and river runoff in July 1991 by the AHMS is discussed in the following.

The monthly precipitation, evaporation, net infiltration, and runoff in July 1991 in both simulations are spatially averaged over the BB subbasin and listed in Table 6.1. There is almost the same amount of monthly net precipitation in two simulations, and even more precipitation in the AHMS simulation. But compared to the NoahMP-HMS simulation, the runoff generated in the BB subbasin is obviously lower in the AHMS simulation, with a difference of 73.4 mm/month.

Also, Table 6.1 shows the monthly runoff amount for various components in both simulations, including infiltration-excess runoff, saturation-excess runoff, and groundwater supply to streams. The difference of infiltration-excess runoff is -68.5 mm/month, explaining 93% of their total runoff difference. It demonstrates that the shortage of infiltration-excess runoff in the AHMS simulation leads to the large difference of total runoff.

Table 6.1 Monthly precipitation, evapotranspiration, net precipitation, net infiltration, and runoffs in July 1991 in the BB subbasin in the AHMS and the NoahMP-HMS simulation.

	P (mm)	E (mm)	P-E (mm)	I_{net} (mm)	R (mm)	R_{ins} (mm)	R_{sat} (mm)	Q_{cg} (mm)
R_{AHMS}	244.0	141.3	102.7	77.0	46.5	25.4	0.2	20.9
$R_{NoahMP\text{-}HMS}$	204.7	99.2	105.5	11.8	119.5	93.9	3.4	22.6
difference	39.3	42.1	-2.8	65.2	-73.4	-68.5	-3.2	-1.7

Note: P: precipitation, E: evapotranspiration, P-E: net precipitation, I_{net}: net infiltration, R: total runoff, R_{ins}: infiltration-excess runoff, R_{sat}: saturation-excess runoff, Q_{cg} (+): groundwater supply to streams, difference = R_{AHMS} - $R_{NoahMP\text{-}HMS}$.

The 25-year offline simulation shows that the amount of monthly runoff in the Huaihe basin is largely determined by monthly precipitation (see Section 4.4). Furthermore, infiltration-excess runoff occurs only when precipitation intensity exceeds infiltration capacity in the scheme (see Section 3.2). Consequently, the analysis focus on the spatial distribution of precipitation and its intensity. Fig. 6-2(a) depicts the spatial distribution of monthly mean precipitation in July 1991 simulated by the AHMS, and Fig. 6-2(b) presents the observed precipitation used in the NoahMP-HMS simulation. According to the observation (Fig. 6-2(b)), a large amount of precipitation occurs in the mountains of southern BB subbasin and in the downstream plains in July 1991. The spatial pattern of rainfall that occurs in July 1991 is captured by the AHMS, as illustrated in Fig. 6-2(a).

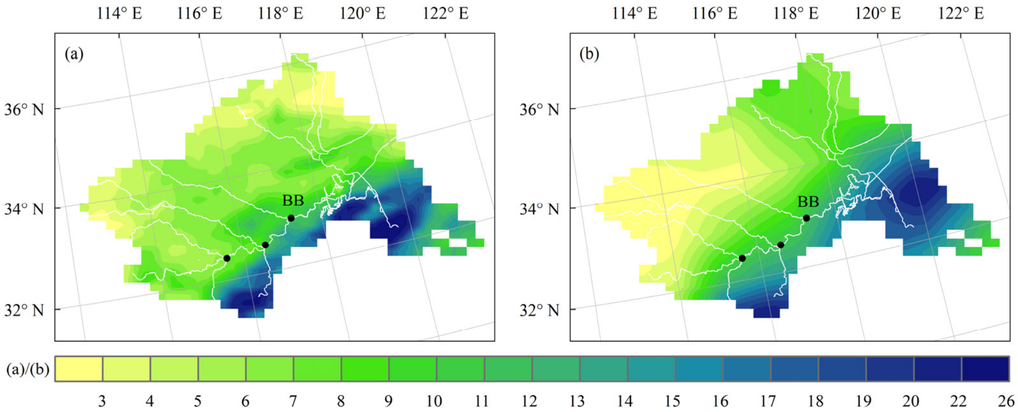

Fig. 6-2 Spatial distribution of monthly mean precipitation (mm/d) in July 1991 in the AHMS (a) and the NoahMP-HMS (b) simulation.

Given that the runoff coefficient is significantly higher in the southern region of the Huai River (illustrated in Section 4.4), the statistical calculation are carried out separately for the northern and the southern parts of the Huai River in the BB subbasin (Table 6.2). For comparison, all the values in Table 6.2 are spatially averaged over the area of the BB subbasin.

In the northern subbasin, the precipitation simulated by the AHMS is higher than in the WRF simulation, with a 37.4 mm/month difference (averaged over the BB subbasin). But the occurrence of infiltration-excess runoff in this region is limited in the AHMS simulation (8.6 mm/month) and the NoahMP-HMS simulation (19.4 mm/month). In the southern part, the monthly precipitation amounts approximately equal in the two simulations, however, the infiltration-excess runoff by the AHMS is lower, with a difference of 57.6 mm/month.

The combination of Table 6.1 and Table 6.2 reveals that the difference of infiltration-excess runoff in the BB subbasin south of the Huai River accounts for 84% of the infiltration-excess runoff difference and 79% of total runoff in the BB subbasin. Hence, the underestimation of flood flow in July 1991 at the BB station in the AHMS simulation is mainly caused by inadequately generated infiltration-excess runoff in the southern region of the Huai River.

Table 6.2 Monthly precipitation, evapotranspiration, net infiltration, and infiltration-excess runoff in July 1991 in the BB subbasin southern and northern of the Huai River, as well as their percentage to monthly precipitation.

		P (mm)	R_{ins} (mm)	E (mm)	I_{net} (mm)	R_{ins}/P (%)	E/P (%)	I_{net}/P (%)
southern	R_{AHMS}	115.3	16.8	47.3	51.1	15	41	44
	$R_{NoahMP\text{-}HMS}$	113.4	74.4	32.2	6.9	66	28	6
	difference	1.9	-57.6	15.1	44.2	/	/	/
northern	R_{AHMS}	128.7	8.6	94	26	7	73	20
	$R_{NoahMP\text{-}HMS}$	91.3	19.4	67	4.9	21	73	5
	difference	37.4	-10.8	27	21.1	/	/	/

Note: all the values in this table are spatially averaged over the BB subbasin;

The precipitation intensity in the BB subbasin south of the Huai River from July 1 to July 31 is statistically calculated and depicted in Fig. 6-3(a). The amount of infiltration-excess runoff resulted from the corresponding rainfall events are shown in Fig. 6-3(b). In the NoahMP-HMS simulation, 85% of the precipitation in July is contributed by rainstorms, especially the rainfall events with intensity higher than 50 mm/day; and these intense rainfall events contributes a majority of infiltration-excess runoff (as shown in Fig. 6-3(b)). On the contrary, the simulated precipitation by the AHMS is distributed more evenly regarding intensity (see in Fig. 6-3(a)), which negatively affects the generation of infiltration-excess runoff. Therefore, in July 1991, the infiltration-excess runoff amount by the AHMS is 16.8 mm, while it is 74.4 mm in the NoahMP-HMS simulation.

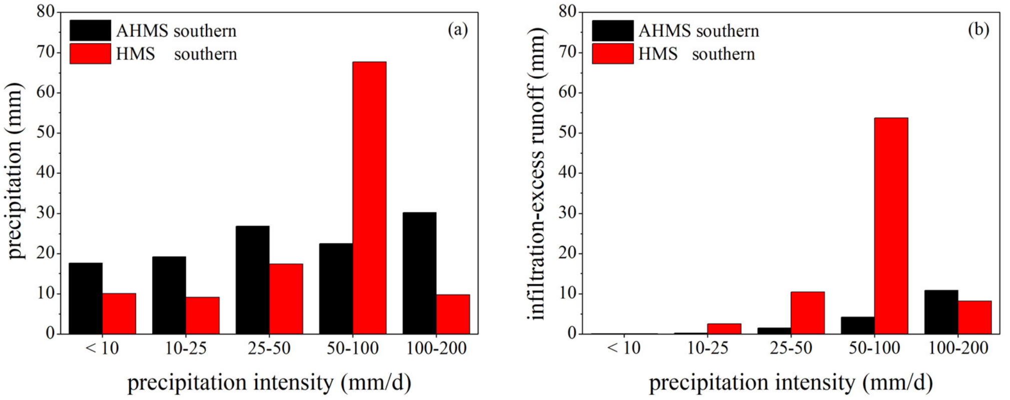

Fig. 6-3 Statistical calculation for precipitation in July 1991 in the BB subbasin southern of the Huai River, as well as the amount of infiltration-excess runoff resulted from the corresponding rainfall events.

In summary, the AHMS underestimates the river discharge at the BB station in July 1991. On the contrary, the runoff amount in the BB subbasin is well estimated by the NoahMP-HMS. According to the aforementioned analysis, the underestimation by the AHMS is mainly caused by the inadequately generated infiltration-excess runoff in the mountains of the southern subbasin. The infiltration-excess runoff results from rainstorms, and its occurrence and quantity are dependent on the characteristics, i.e. intensity, duration and spatial distribution. The amount of precipitation in the mountainous regions are nearly identical in both simulations. The precipitation simulated by the AHMS is distributed more evenly regarding intensity, in comparison to the precipitation observation that is used to drive the NoahMP-HMS. Whereas, a larger proportion of low-intensity rainfall affect adversely the occurrence of infiltration-excess runoff.

6.2 Summary

In this study, a coupled Atmospheric and Hydrological Modelling System (AHMS) is developed, which consists of the Weather Research and Forecasting (WRF) Model, the Noah Multi-parameterization Land Surface Model (Noah-MP LSM), and the distributed hydrological model HMS. Meanwhile, the coupled land surface and hydrological model (NoahMP-HMS) that can be driven by meteorological forcing data is available.

A new parameterization of hillslope runoff is achieved based on the calculation of infiltration capacity under hillslope topography. This new parameterization is first used in the NoahMP-HMS, for the land surface and hydrological simulation in the Huaihe basin of China. According to the simulation of the Huaihe basin from 1980 to 1987, the effectiveness of this new parameterization is assessed, and the NoahMP-HMS is validated. The results show that the relative bias of simulated annual runoff to the observation decreases from -60% to 6%, when using the new hillslope runoff parameterization; including it, the NoahMP-HMS has a great ability of reproducing hydrological processes and terrestrial water balance. Specifically, the Nash-Sutcliffe efficiency coefficients (NSIs) of the simulated daily streamflow at the three hydrological stations of the main stream are 0.67, 0.81, and 0.80, respectively; their water balance indexes (WBIs) are close to 1.0. Furthermore, the spatiotemporal variability of the hydrological processes in the basin is investigated based on the long-term simulation from 1979 to 2003. The findings are shown in the conclusion section of Chapter 4.

The AHMS with the new parameterization is used to simulate the coupled atmospheric and hydrological simulation in the Huaihe basin from July to November 1991. The performance of the AHMS is evaluated in terms of the accuracy in estimating precipitation, air temperature, and daily streamflow. The NSIs of the simulated daily streamflow are about 0.55, and their WBIs ranges from 0.63 to 0.79. It demonstrates that the AHMS can appropriately simulate the daily streamflow in the Huaihe basin. In addition, the impact of the fully coupled atmospheric and hydrological simulation is investigated by comparison with the stand-alone atmospheric simulation (by WRF). The more outcomes are presented in the conclusion section of Chapter 5.

6.3 Outlook

Based on the results of this study, it is proposed to focus future work on:

1) Regional atmospheric and hydrological simulation at a finer resolution and in different regions. The nesting technique of WRF enables the AHMS to simulate atmospheric and hydrological processes at higher resolution, e.g. 10 km, 5 km. With a finer resolution, the geographical features can be better captured, and the atmospheric processes may be more precisely predicted, which potentially improves hydrological forecasts.

2) Further improvement for the hillslope runoff parameterization. In this study, the infiltration capacity is simplified as the hydraulic conductivity at the maximum soil wetness. The maximum soil moisture under the hillslope topography is presumed as the average of the saturated soil moisture and field capacity. The topography position index (TPI) can be used to categorize the topography in a more detailed way. Using the TPI, the landscape is classified into discrete slope position classes, including low slope (flat), moderate slope, high slope (cliff), very positive slope (ridge), and very negative slope (valley).

3) This AHMS can be used to simulate the spatial distribution of water resource at catchment- or continental scale, to assess the availability of regional water resources, and to predict the effects of future climate change on the sustainable development of ecosystem, as well as their interaction.

7 Appendix

7.1 Water balance equation

The water balance involved in the coupled land surface and hydrological model (NoahMP-HMS) and in the coupled Atmospheric and Hydrological Modelling System (AHMS) are as shown as following:

(1) Water balance in the multi-layer soil model domain (i.e. LSM soil model domain)

$$\frac{dw_{us}}{dt} = I_{net} - q_{re}$$

$$I_{net} = I_{soil} - E_{soil} - E_{trans} - R_{sat}$$

(2) Water balance in the aquifer

$$\frac{dw_{ug}}{dt} = I_{net} - Q_{cg}$$

(3) Water balance in rivers and lakes

$$\frac{dw_{sf}}{dt} = R_{inf} + R_{sat} + Q_{cg} - Q_{out}$$

(4) Water balance at the land surface

$$P = E + I_{net} + R_{sf} + \frac{dw_{snow}}{dt} + \frac{dw_{can}}{dt}$$

$$R_{sf} = R_{ins} + R_{sat}$$

$$E = E_{can} + E_{soil} + E_{trans} + E_{snow}$$

(5) Terrestrial water balance

$$\frac{dw_{ug}}{dt} + \frac{dw_{snow}}{dt} + \frac{dw_{can}}{dt} = P - E + R$$

$$R = R_{ins} + R_{sat} + Q_{cg}$$

$$\frac{dw_{trr}}{dt} = \frac{dw_{ug}}{dt} + \frac{dw_{snow}}{dt} + \frac{dw_{can}}{dt}$$

(6) Total water balance in the catchment

$$\frac{dw_t}{dt} = P - E - Q_{out}$$

$$\frac{dw_t}{dt} = \frac{dw_{ug}}{dt} + \frac{dw_{sf}}{dt} + \frac{dw_{snow}}{dt} + \frac{dw_{can}}{dt}$$

$\frac{dw_t}{dt}$: the change of water storage in the catchment [m/s];

$\frac{dw_{us}}{dt}$: the change of unsaturated soil water in the LSM soil model domain [m/s];

$\frac{dw_{ug}}{dt}$: the change of soil water storage in the aquifer [m/s];

$\frac{dw_{sf}}{dt}$: the change of water storage in rivers and lakes [m/s];

$\frac{dw_{snow}}{dt}$: the change of snow storage [m/s];

$\frac{dw_{can}}{dt}$: the change of canopy stored water [m/s];

P: the precipitation [m/s];

I_{soil}: the total infiltration which is calculated in the land surface model [m/s];

E: the evapotranspiration [m/s];

Q_{out}: the outflowing water flow from the catchment [m/s];

R: the total runoff [m/s];

I_{net}: the net infiltration [m/s];

q_{re}: the flux at the bottom of the LSM soil model domain [m/s];

E_{soil}: the direct evaporation from bare soil [m/s];

E_{trans}: the plant transpiration extracted from soil layers [m/s];

E_{can}: the evaporation of precipitation intercepted by vegetation canopy [m/s];

R_{sf}: the surface runoff [m/s], including infiltration-excess runoff and saturation-excess runoff;

R_{sat}: the saturation-excess runoff [m/s];

R_{ins}: the infiltration-excess runoff [m/s];

Q_{cg}: the interactive flux between groundwater and channel water [m/s], positive Q_{cg} represents the flow from groundwater to streams.

7.2 Evaluation indexes for streamflow estimates

In hydrology, some statistical indices are used to measure the goodness of fit between two series dataset, e.g. simulated streamflow and measured discharge. The water balance index (WBI) represents the ability of model to reconstruct water balance processes. Pearson product-moment correlation coefficient (PMC) describes the correlation of two time series. Nash-Sutcliffe coefficient of efficiency index (NSI) is frequently used to reflect the ability to simulate the peak of time series. The index of agreement (IOA) represents the similarity degree of two time series. Normalized root-mean-square error (NRSE) measures the differences between two time series. Their detailed formulas are:

$$PMC = \frac{\sum_{i=1}^{N}\left(Q_s^i - \overline{Q}_s\right)\left(Q_o^i - \overline{Q}_o\right)}{\sqrt{\sum_{i=1}^{N}\left(Q_o^i - \overline{Q}_s\right)^2}\sqrt{\sum_{i=1}^{N}\left(Q_o^i - \overline{Q}_o\right)^2}}$$

$$WBI = \frac{\sum_{i=1}^{N} Q_s^i}{\sum_{i=1}^{N} Q_o^i}$$

$$NSI = 1.0 - \frac{\sum_{i=1}^{N}\left(Q_s^i - Q_o^i\right)^2}{\sum_{i=1}^{N}\left(Q_o^i - \overline{Q}_o\right)^2}$$

$$IOA = 1.0 - \frac{\sum_{i=1}^{N}\left(Q_s^i - Q_0^i\right)^2}{\sum_{i=1}^{N}\left(\left|Q_0^i - \overline{Q}_0\right| + \left|Q_s^i - \overline{Q}_0\right|\right)^2}$$

$$NRSE = \sqrt{\frac{1}{N}\sum_{i=1}^{N}\left(\frac{Q_s^i - Q_o^i}{\overline{Q}_o}\right)^2}$$

where Q_s^i and Q_o^i signify time series of simulated and observed daily streamflow [m^3/s], $\overline{Q}_s$ and $\overline{Q}_o$ denote time-averaging streamflow [m^3/s], N is the number of samples in the time series.

7.3 Automatic calibration using ABC-DREAM algorithm

Based on the sensitivity analysis for the hydrological parameters of the sub-basins, the Manning roughness coefficients in the WJB subbasin and the WJB-LTZ subbasin are automatically calibrated using the differential evolution adaptive Metropolis (DREAM) algorithm. The DREAM algorithm is one algorithm of approximate Bayesian computation (ABC) methods which is usually used to optimize the model parameters. Its detailed algorithm is elaborated in Section 7.4.

For calibrating Manning roughness coefficients, the Nash-Sutcliffe coefficient of efficiency index (NSI) of daily streamflow at the LTZ station is selected as the optimization target. Hence, the observed daily streamflow in 1980 at the LTZ station is viewed as a reference time series for the ABC-DREAM automatic calibration program. Using the Manning roughness coefficient values determined by the ABC-DREAM algorithm, the coupled land surface and hydrological model (NoahMP-HMS) simulates the hydrological processes of the Huaihe basin in 1980. When all the parameters converge to a stable scope, the iteration in the ABC-DREAM algorithm stops. The samples in the second half of the iterations are used to estimate the posterior distribution for parameters, as shown in Fig. 7-1.

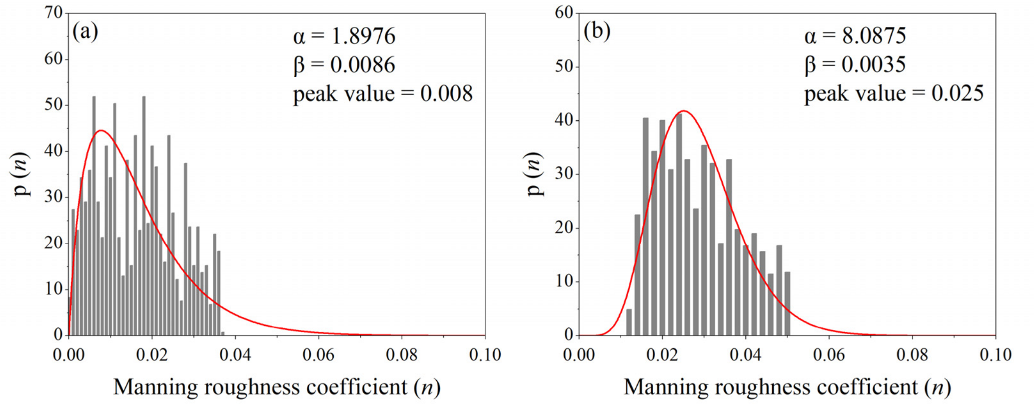

Fig. 7-1 Probability density function for the Manning roughness coefficient in the WJB subbasin (a) and in the WJB-LTZ subbasin (b).

The peak value in the probability distribution function of Fig. 7-1 is selected as the parameter value of the Manning roughness coefficient, i.e. 0.008 for the WJB subbasin and 0.025 for the WJB-LTZ subbasin. The peak value in the probability distribution function of parameters is selected as the value for the Manning roughness coefficient, i.e. 0.008 for that in the WJB subbasin (Fig. 7-1(a)) and 0.025 for that in the WJB-LTZ subbasin (Fig. 7-1(a)). Using these automatically calibrated parameter values, the NoahMP-HMS is used to simulate the hydrological process of the Huaihe basin in 1980.

The simulated daily streamflow by the NoahMP-HMS using the automatically calibrated parameter values are compared with the observation, as shown in Fig. 7-2; meanwhile, the simulated daily streamflow by the NoahMP-HMS using the default Manning roughness coefficient (0.02 in the Huaihe basin) is also included in Fig. 7-2. The Nash-Sutcliffe coefficient of efficiency index (NSI), Pearson product-moment correlation coefficient (PMC), and Water Balance Index (WBI) of simulated daily streamflow at the hydrological station of WJB, LTZ, and BB are calculated and presented in Table 7.1.

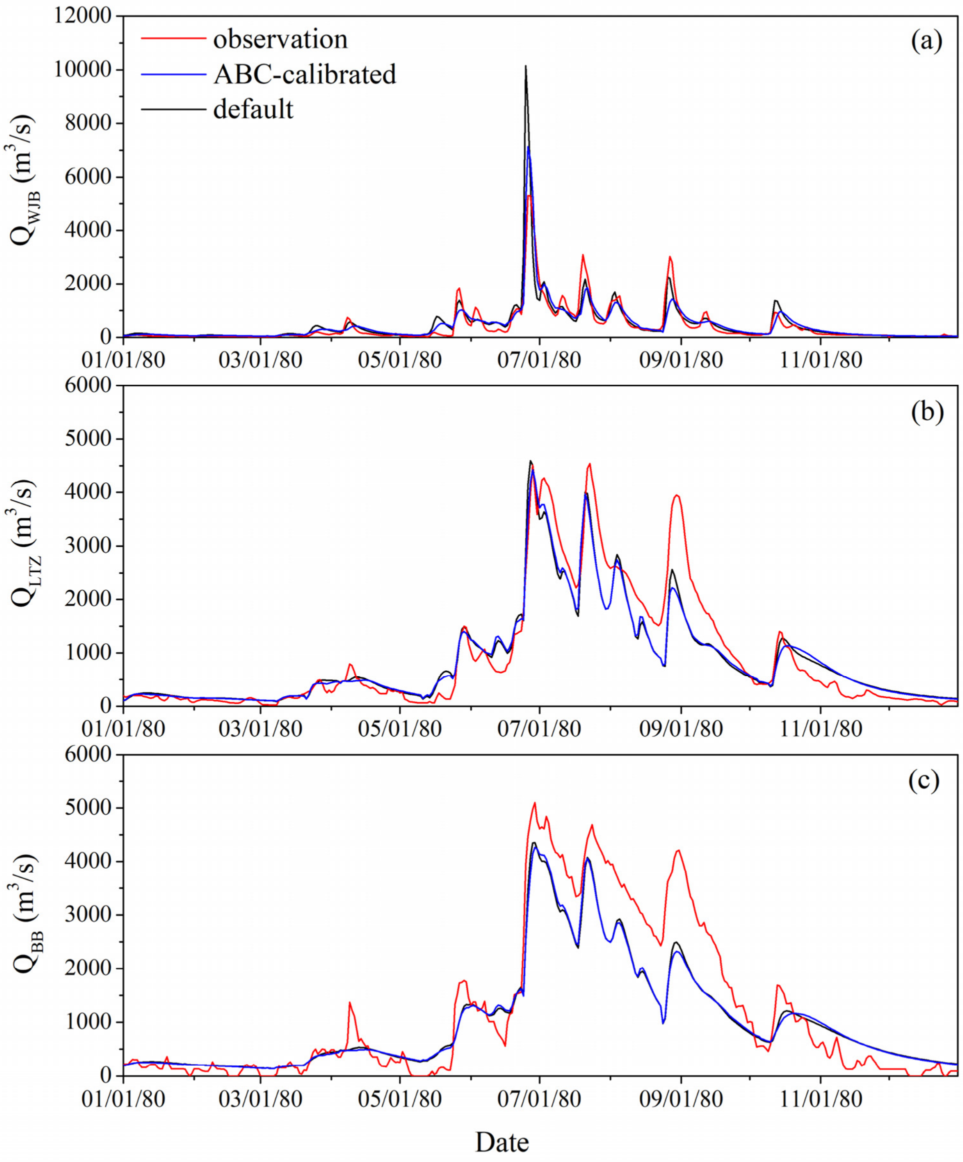

Fig. 7-2 Comparison of observed and simulated daily streamflow by the NoahMP-HMS at the hydrological station of WJB (a), LTZ (b), and BB (c).

As shown in Fig. 7-2, using the automatically calibrated Manning roughness coefficient, the simulated daily streamflow at the LTZ and BB station matches well with the observed river discharge in term of both intensity and timing. And there are very high efficiency coefficient values (NSI, 0.872 and 0.828) and the correlation coefficient values (PMC, 0.947 and 0.957) at these two stations. It illustrates that the ABC-DREAM algorithm works well in automatically calibrating the Manning roughness coefficient in the hydrological model.

Table 7.1 Evaluation indices of simulated daily streamflow at the WJB, LTZ, and BB station by the NoahMP-HMS with the ABC-calibrated Manning roughness coefficient and other default parameter values.

station	ABC-calibrated parameter $n_{WJB} = 0.008$, $n_{WJB\text{-}LTZ} = 0.025$			default parameter $n = 0.02$		
	NSI	PMC	WBI	NSI	PMC	WBI
WJB	0.569	0.841	1.121	0.818	0.913	1.084
LTZ	0.872	0.947	0.926	0.868	0.946	0.927
BB	0.828	0.957	0.837	0.823	0.954	0.836

Compared with the default values, the NoahMP-HMS using the ABC-calibrated parameter values behaves slightly better in reproducing streamflow at the LTZ and the BB stations. The efficiency coefficient (NSI) and the correlation coefficient (PMC) at two stations are slightly higher (see in Table 7.1). But the efficiency coefficient (NSI) of simulated daily streamflow at the WJB station decreased from 0.82 to 0.57, when using the ABC-calibrated Manning roughness coefficient.

According to the measured hydrograph (red line in Fig. 7-2(a)), the first flood peak reaches at the WJB station on June 26, 1980, with flood peak flow of 5300 m^3/s. In the NoahMP-HMS simulation with default parameter values, the simulated first flood peak flow at the WJB station is 7126 m^3/s, which take places on June 26, 1980. In the NoahMP-HMS simulation with calibrated parameter values, the first flood peak arrives on June 25, with peak flow of 10150 m^3/s. Obviously, because of the lower Manning roughness coefficient in the WJB subbasin, the runoff congregates to the outlet more quickly and results in higher flood peak.

Accordingly, it can be known that when the LTZ station is selected as the optimization target, the simulated streamflow of this station after the calibration by the ABC-DREAM algorithm matches well with the observation. But it is less beneficial to the simulation at the WJB station. The usage of multi-target optimization in the ABC-DREAM algorithm (e.g. the efficiency coefficients at more stations) probably improves the effectiveness of the calibration.

7.4 ABC-DREAM algorithm

In common, hydrological models are calibrated by optimizing model parameters to enable the model outputs to match an observed reference time series (e.g. river discharge) as closely as possible. Two methods are usually used for the calibrating hydrologic models. One is a user-guide trial and error procedure, where the user controls the change of parameter values and determines whether the calibration target has been met by comparing simulation and observation. The user is supposed to have adequate knowledge about the model and know how each parameter affects the simulation. The second is automatic calibrations, in which the simulation is iteratively carried out with parameter values calculated using one certain algorithm. The iteration stops only when the statistical results meet the calibration requirement. This automatic method mainly depends on the algorithm for sampling parameter values and statistical assessment for determining the simulation accuracy.

Traditionally, the parameters are manually tuned by comprehensive comparison of simulated and observed time series. But this approach is subjective, labor-intensive, and difficult to extend. Instead, automatic calibration techniques have the advantages of efficiency, effectiveness, and extensibility, which results in a broad application and great progress. The automatic calibration method mainly includes three categories, data assimilation technique, optimization algorithm, and probability distribution function (PDF) method. The PDF method is the only one that aims to obtain an estimation of the posterior distributions for uncertain parameters based on Bayesian statistics and a likelihood function.

During recent years, a likelihood-free inference using Markov Chain Monte Carlo (MCMC) technique has been widely used. This method is especially useful for cases where the likelihood is intractable, too expensive to be evaluated, or impossible to be formulated explicitly. The likelihood-free method is also referred to Approximate Bayesian Computation (ABC).

7.4.1 Approximate Bayesian Computation

In a common calibration problem, one expects to estimate the parameter values of a model given an observation of system behavior. The observation, $\widetilde{\boldsymbol{Y}} = \left\{\widetilde{y_1},\ldots,\widetilde{y_n}\right\}$, is recorded from the physical system, $\tilde{\varsigma}$, related to the unknown system parameters $\boldsymbol{\theta}^{*} = \left\{\theta_1^*,\ldots,\theta_d^*\right\}$ in reality:

$$\widetilde{\boldsymbol{Y}} \leftarrow \tilde{\varsigma}\left(\boldsymbol{\theta}^{*}\right) + \boldsymbol{\varepsilon}$$

where $\boldsymbol{\varepsilon} = \{\varepsilon_1, ..., \varepsilon_n\}$ is a vector of measurement errors; d is the dimension of unknown parameters.

With a model, H, representing the physical process, one can simulate the response of the system to forcing data $\tilde{\boldsymbol{u}} = \{\widetilde{u_1}, ..., \widetilde{u_n}\}$ at an initial state $\widetilde{\boldsymbol{x_0}}$, and obtain the corresponding results $\boldsymbol{Y} = \{y_1, ..., y_n\}$ over simulation period $\boldsymbol{t} = \{t_1, ..., t_n\}$:

$$\boldsymbol{Y} \sim \mathrm{H}\left(\boldsymbol{\theta}, \tilde{\boldsymbol{u}}, \widetilde{\boldsymbol{x_0}}\right)$$

where $\boldsymbol{\theta} = \{\theta_1, ..., \theta_d\}$ is proposal parameter values.

The difference between the observed system behavior and the simulated model results is defined as an error residual:

$$\boldsymbol{e} = F\left[\widetilde{\boldsymbol{Y}}\right] - F\left[\boldsymbol{Y}\right]$$

where $F[\cdot]$ allows for a transformation of the observation and the simulation; $\boldsymbol{e} = \{e_1, ... e_n\}$ signifies the residual vector. The residual originates from a variety of error sources, including inadequate knowledge about system parameters ($\overset{*}{\boldsymbol{\theta}}$), incorrect information in inputted forcing data ($\tilde{\boldsymbol{u}}$), initial states ($\widetilde{\boldsymbol{x_0}}$), numerical error, spatial discretization, and improper model formulation (Vrugt and Sadegh, 2013).

Assumed that model parameters ($\boldsymbol{\theta}$) are the only source of uncertainty, the posterior parameter distribution can be estimated by Bayes theorem:

$$p\left(\boldsymbol{\theta} \middle| \widetilde{\boldsymbol{Y}}\right) = \frac{p(\boldsymbol{\theta})\, p\left(\widetilde{\boldsymbol{Y}} \middle| \boldsymbol{\theta}\right)}{p\left(\widetilde{\boldsymbol{Y}}\right)}$$

For convenience, which is written as the un-normalized density

$$p\left(\boldsymbol{\theta} \middle| \widetilde{\boldsymbol{Y}}\right) \propto p(\boldsymbol{\theta})\, L\left(\boldsymbol{\theta} \middle| \widetilde{\boldsymbol{Y}}\right)$$

where $p\left(\boldsymbol{\theta} \middle| \widetilde{\boldsymbol{Y}}\right)$ signifies the posterior parameter distribution, $p(\boldsymbol{\theta})$ is the prior parameter distribution, $L\left(\boldsymbol{\theta} \middle| \widetilde{\boldsymbol{Y}}\right) \equiv p\left(\widetilde{\boldsymbol{Y}} \middle| \boldsymbol{\theta}\right)$ denotes the likelihood function that describes the probability of the data given parameter values.

Rooted in Bayesian theory, Approximate Bayesian Computation (ABC) method approximates the likelihood function by the comparison between the observation and the simulation, which is considered as a "likelihood-free" inference. Another point behind ABC is that the trial parameter value (**θ**) becomes a sample of the posterior parameter distribution as long as the distance between observed data and simulated data, $\rho\left(\widetilde{\boldsymbol{Y}},\boldsymbol{Y}\left(\boldsymbol{\theta}\right)\right)$, is smaller than a small positive value, i.e. $\rho\left(\widetilde{\boldsymbol{Y}},\boldsymbol{Y}\left(\boldsymbol{\theta}\right)\right)\leq\varepsilon$. The sampled distribution converges to the true posterior distribution, $p\left(\boldsymbol{\theta}\middle|\widetilde{\boldsymbol{Y}}\right)$, in the limit situation of $\varepsilon\rightarrow 0$ (Beaumont et al., 2002).

The sampling algorithms of the approximate Bayesian computation (ABC) method can be classified into three categories: the rejection sampling algorithm, the sequential Monte Carlo method, and the Markov chain Monte Carlo method. The Markov chain Monte Carlo sampling method is easily embedded to Approximate Bayesian Computation being the ABC-MCMC algorithm, which has sufficient advantages in both computational efficiency and estimation accuracy.

7.4.2 Markov chain Monte Carlo method

The basic point of the Markov chain Monte Carlo method is a Markov chain that generates a transition from one state to another state throughout the search space using the random-walk Metropolis algorithm. Given that the current state is $\boldsymbol{X^t}$ and the previous states are signified by $\boldsymbol{X}=\left\{\boldsymbol{X}^0,\boldsymbol{X}^1,...,\boldsymbol{X}^t\right\}$, the random-walk Metropolis algorithm intends to create a Markov chain by sampling candidate parameter values (**θ**) from the proposal distribution based on sampled states, i.e.

$$\boldsymbol{\theta}\sim q\left(\cdot\middle|\boldsymbol{X}\right)$$

With Markov property that the probability distribution of parameter at next state depends that on current state instead of all the previous states, the proposal parameter distribution can be simplified as

$$q\left(\boldsymbol{\theta}|\boldsymbol{X}\right)=q\left(\boldsymbol{\theta}|\boldsymbol{X}^t\right)$$

In the Metropolis-Hasting algorithm (Hasting, 1970), the acceptance probability of the candidate vector **θ** at current state $\boldsymbol{X^t}$ is given by

$$\alpha\left(\boldsymbol{X}^t,\boldsymbol{\theta}\right)=min\left(1,\frac{\pi\left(\boldsymbol{\theta}\right)q\left(\boldsymbol{X}^t|\boldsymbol{\theta}\right)}{\pi\left(\boldsymbol{X}^t\right)q\left(\boldsymbol{\theta}\middle|\boldsymbol{X}^t\right)}\right)$$

where $\alpha\left(\boldsymbol{X}^t,\boldsymbol{\theta}\right)$ is the probability to accept the trial parameter vector, $\boldsymbol{\theta}$, from current state, $\boldsymbol{X}^t$; $\pi(\cdot)$ denotes the probability density function of the target distribution; $q\left(\cdot|\cdot\right)$ is the conditional proposal distribution to perform a trial jump from current state to another state.

For cases with a non-symmetrical jumping distribution, i.e. $q\left(\boldsymbol{X}^t|\boldsymbol{\theta}\right) \neq q\left(\boldsymbol{\theta}|\boldsymbol{X}^t\right)$, we calculate the acceptance probability by

$$\alpha\left(\boldsymbol{X}^t,\boldsymbol{\theta}\right) = max\left(I\left(f\left(\boldsymbol{\theta}\right) \geq f\left(\boldsymbol{X}^t\right)\right), I\left(f\left(\boldsymbol{\theta}\right) \geq \varphi - \varepsilon\right)\right)$$

and the fitness between the observation and the simulation is defined as

$$f\left(\boldsymbol{\theta}\right) = \varphi - \rho\left(\tilde{\boldsymbol{Y}} - \boldsymbol{Y}\left(\boldsymbol{\theta}\right)\right)$$

where φ is a threshold coefficient; $f\left(\boldsymbol{\theta},\varphi\right)$ is defined as the fitness of the observed data ($\tilde{\boldsymbol{Y}}$) and the simulated data ($\boldsymbol{Y}$) using proposal parameter values ($\boldsymbol{\theta}$); $I\left(\cdot\right)$ is an indicator function; $\rho\left(\tilde{\boldsymbol{Y}},\boldsymbol{Y}\left(\boldsymbol{\theta}\right)\right)$ is a function to quantify the distance between the observation and the simulation, and a smaller distance means that both match better.

Thus, the condition of $\rho\left(\tilde{\boldsymbol{Y}},\boldsymbol{Y}\left(\boldsymbol{\theta}\right)\right) \leq \varepsilon$ is changed into $f\left(\boldsymbol{\theta}\right) \geq \varphi - \varepsilon$ with $\varphi = \varepsilon$, which indicates that the candidate parameter values will be accepted under the conditions of non-negative fitness, i.e. $f\left(\boldsymbol{\theta}\right) \geq 0$. Based on it, a reversible Markov chain is created, and the successive samples are used to approximate the posterior parameter distribution.

With the computed acceptance probability, $\alpha\left(\boldsymbol{X}^t,\boldsymbol{\theta}\right)$, the new state $\boldsymbol{X}^{t+1}$ can be determined by

$$\boldsymbol{X}^{t+1} = \begin{cases} \boldsymbol{X}^t & if\,\alpha\left(\boldsymbol{X}^t,\boldsymbol{\theta}\right) = 1 \\ \boldsymbol{\theta} & if\,\alpha\left(\boldsymbol{X}^t,\boldsymbol{\theta}\right) = 0 \end{cases}$$

In the ABC-MCMC method, these steps above are repeated until the samples converge to a stationary posterior distribution.

With the widespread implement of the basic MCMC method, researchers have found that an effective proposal distribution is essential that helps to converge to a reasonable distribution in a limited amount of time. If the proposal distribution is too wide, too many candidate parameter values are rejected, and hence chains cannot mix sufficiently and results in a slow convergence. On the contrary, when the proposal distribution is too narrow, the searching space is so small that it takes a large number of iterations to find a solution. Moreover, the convergence efficiency is related to the scale and the orientation of the proposal distribution.

Some adaptive MCMC methods are sequentially proposed to automatically tune the size and the shape of a proposal distribution and overcome the slow convergence of the MCMC which is frequently caused by an inappropriate selection of the proposal distribution. These adaptive methods, such as the Adaptive Metropolis algorithm (Haario et al., 2001), are modified from the Adaptive Proposal (Haario et al., 1999) by a covariance adaption strategy.

In the Adaptive Proposal algorithm, the proposal parameter distribution is automatically tuned using a Gaussian distribution with the mean at current state, $\boldsymbol{X^t}$, and the covariance that is calculated from a finite number of historical states as

$$q\left(\cdot\middle|\boldsymbol{X^t}\right) \sim N\left(\boldsymbol{X^t}, c_d^2 \cdot R^t\right)$$

where R^t is a $d \times d$-covariance matrix determined by the H state, $\left\{\boldsymbol{X^t}, \ldots \boldsymbol{X^{t-H+2}}, \boldsymbol{X^{t-H+1}}\right\}$, c_d is a scaling factor that depends on the dimension of parameters, d.

It has been proved that the covariance adaptation affects significantly both the size and the spatial orientation of the proposal distribution and adapts continuously to the target distribution.

7.4.3 Differential evolution adaptive Metropolis algorithm

The differential evolution adaptive Metropolis (DREAM) method is first used by Vrugt et al. (2008) in hydrologic modelling. DREAM is a follow up on the Differential Evolution Markov chain (DE-MC) (Ter Braak et al., 2006) whose advantages over other MCMC methods are simplicity and convergence speed, even for nearly collinear parameters and multimodal densities. To describe clearly DREAM, we have a closer look at DE-MC algorithm first.

7.4.3.1 Differential evolution Markov chain

The DE-MC algorithm integrates the point of Differential Evolution (Price and Storn, 1997) and the MCMC algorithm, resulting in a population MCMC algorithm where multiple chains can run parallelly.

In the DE-MC method, several different chains run simultaneously in parallel, instead of one single chain. Then all the parameter values sampled from all chains at the current state form a population, conveniently stored as a $m \times d$ matrix $\boldsymbol{X} = \left\{ \boldsymbol{X}_{\cdot 1}^{t}, ..., \boldsymbol{X}_{\cdot j}^{t}, ..., \boldsymbol{X}_{\cdot m}^{t} \right\}$ and $\boldsymbol{X}_{\cdot j}^{t} = \left\{ x_{1j}^{t}, ..., x_{ij}^{t}, ..., x_{dj}^{t} \right\}$, where m is the number of chains, d is the number of parameter dimensions. One trial point in one certain chain, θ_{ij}^{t+1}, is generated by weighted adding the difference of two members to the sample at current state, which is called mutation, as

$$\theta_{ij}^{t+1} = x_{ij}^{t} + \gamma \left(x_{1r_1}^{t} - x_{1r_2}^{t} \right) + e$$

where r_1, r_2 are one pair of randomly selected members from the population, $r_1 \neq r_2 \neq j \in [1, m]$; γ is a scaling factor that depends on the parameter dimension d, and $\gamma = 2.38 / \sqrt{2d}$ is an optimal taken value; e is one value drawn from a symmetric distribution with a small variance compared to that of the target distribution, i.e. $e \sim N(0, b)$ with a minor value b; x_{ij}^{t} signifies the value of parameter i in Chain j at current state t; θ_{ij}^{t+1} represents a trial value for parameter i in Chain j for next state $t+1$.

As mentioned in this section, DE-MC directly uses parameter values at the current state to produce a candidate parameter vector, instead of the covariance adaption that is used in the MCMC algorithm.

The combination of DE and MCMC solves an important problem in real parameter spaces for MCMC, namely that of choosing an appropriate scale and the orientation for the jumping distribution (Ter Braak et al., 2006).

7.4.3.2 Differential evolution adaptive metropolis algorithm

The differential evolution adaptive Metropolis (DREAM) algorithm extends the usage of the DE-MC method to improve search efficiency. For example, one pair of randomly selected members in the DE-MC method is replaced by higher-order pairs to increase diversity. Since it is not optimal to update all dimensional parameters simultaneously, the randomized subspace sampling strategy selects parameter(s) to be modified according to a certain probability. The DREAM algorithm works as following:

(1) Draw an initial population for each chain, $\boldsymbol{X} = \left\{ \boldsymbol{X}_{\cdot 1}^{t=1}, ..., \boldsymbol{X}_{\cdot j}^{t=1}, ..., \boldsymbol{X}_{\cdot m}^{t=1} \right\}$ and $\boldsymbol{X}_{\cdot j}^{t=1} = \left\{ x_{1j}^{t=1}, ..., x_{ij}^{t=1}, ..., x_{dj}^{t=1} \right\}$, using the prior distribution, which is uniform distribution

in our case.

DO evolution of Markov chain for all the chains $(j=1,...,m)$:

(2) Randomized subspace sampling:

a. sample *P* from a discrete multinomial distribution, $P \sim F(\boldsymbol{CR}|p)$, where ***CR*** is a crossover constant vector in the range of 0 and 1, and $\boldsymbol{CR}=\left\{\frac{1}{n_{CR}},\frac{2}{n_{CR}},...,1\right\}$ with a user-defined parameter n_{CR}.

b. draw *d*-labels, *Z*, from a multivariate uniform distribution, i.e. $Z \sim U_d(0,1)$.

c. If $Z>(1-P), i=1,...,d$, the *i*th parameter is added to the subset A_j and being updated with the proposal distribution.

(3) Trial vector generating:

a. a trial jump distance for *i*th parameter in Chain *j*, $D_{i,j}^{t+1}$, is determined using similar evolution in DE-MC as

$$D_{i,j}^{t+1}=\begin{cases}(1+\lambda)\gamma(\delta,d)\left(\sum_{k=1}^{\delta}X_{g_k,j}^{t}-\sum_{k=1}^{\delta}X_{r_k,j}^{t}\right)+\zeta & X_{i,j}^{t}\in A_j\\ 0 & X_{i,j}^{t}\notin A_j\end{cases}$$

where δ signifies the number of chain pairs used to generate the jump; ***g*** and ***r*** are δ -dimensional vectors with integer values drawn without replacement from $\{1,...,j-1,j+1,...,m\}$, normally $\delta=2$; $\gamma=2.38/\sqrt{2\delta d}$ is the jump rate; λ and ζ are sampled respectively, according to $\lambda \sim U(-c,c)$ and $\zeta \sim N(0,c^{*})$ with *c* (typically, *c*=0.1) and c^{*} which is small compared to the width of the target distribution ($c^{*}=10^{-12}$).

b. the candidate parameter vector in Chain *j* is calculated as

$$\boldsymbol{\theta}_{\cdot j}=\boldsymbol{X}_{\cdot j}^{t}+\boldsymbol{D}_{\cdot j}^{t+1}$$

c. the acceptance probability, $\alpha(\boldsymbol{X}_{\cdot j}^{t},\boldsymbol{\theta}_{\cdot j})$, of the candidate vector, $\boldsymbol{\theta}_{\cdot j}$, is computed and then determine sample values at next state, as

$$\boldsymbol{X}_{\cdot j}^{t+1} = \begin{cases} \boldsymbol{X}_{\cdot j}^{t} & if\, \alpha\left(\boldsymbol{X}_{\cdot j}^{t}, \boldsymbol{\theta}_{\cdot j}\right) = 1 \\ \boldsymbol{\theta}_{\cdot j} & if\, \alpha\left(\boldsymbol{X}_{\cdot j}^{t}, \boldsymbol{\theta}_{\cdot j}\right) = 0 \end{cases}$$

END DO for chain evolution

(4) Convergence judgement: the diagnostic statistic of Gelman and Rubin (1992), $\widehat{R}$, is chose to monitor whether parameter samples in chains converges to a stable range, as

$$\widehat{R}_i = \sqrt{\widehat{V}_i / W}$$

where $\widehat{R}_i$ is the potential scale reduction factor of i^{th} parameter; $\widehat{V}_i$ is the variance of the stationary distribution for i^{th} parameter, estimated by a weighted average of within-chain variance, W_i, and between-chain variance, B_i, by

$$\widehat{V}_i = \left(1 - \frac{1}{n}\right) W_i + \frac{1}{n} B_i$$

$$W_i = \frac{1}{m} \sum_{j=1}^{m} \left(\frac{1}{n-1} \sum_{k=1}^{n} \left(x_{ij}^{k} - \overline{x}_{ij} \right)^2 \right)$$

$$B_i = \frac{n}{m-1} \sum_{j=1}^{m} \left(\overline{x}_{ij} - \overline{\overline{x}}_i \right)^2$$

$$\overline{\overline{x}}_i = \frac{1}{m} \sum_{j=1}^{m} \overline{x}_{ij}$$

$$\overline{x}_{ij} = \frac{1}{n} \sum_{k=1}^{n} x_{ij}^{k}$$

where n is the number of last half samples in every chain (each chain has a length of $2n$); m is the number of chains ($m \geqslant 2$); x_{ij}^{k} is one sampled parameter value; $\overline{x}_{ij}$ is the mean of sampled values for i^{th} parameter in Chain j; $\overline{\overline{x}}_i$ is the mean of i^{th} parameter in all last half chains.

(5) If $\widehat{R}_i < 1.2\left(i = 1, \ldots, d\right)$, stop iteration; otherwise, keep iterating for chain evolution from Step (2).

7.4.4 Application to a parabolic regression model

As a test, the DREAM algorithm (in Fortran) is used to automatically calibrate parameters for a simple parabolic regression model, $y=Ax^2+Bx+C$. A synthetic dataset with a number of equidistant points (n=100) between x_1=0 and x_2=10 is created using A=-0.8, B=8.0, C=1.0. Taken this synthetic dataset as the reference time series (as shown in Fig. 7-5 (black line)), the DREAM program is employed to automatically calibrate the parameters of the parabolic regression model, with

(1) The number of chain pairs for mutation, $\delta = 3$;

(2) Multinomial distribution with crossover constant, $n_{CR} = 3$;

(3) The threshold of Nash-Sutcliffe efficiency coefficient, $\varphi = 75\%$. Nash-Sutcliffe efficiency coefficient is only selected to quantify the goodness-of-fitness between the observation and the simulation.

The time series of the multivariate potential scale reduction factor ($\hat{R}$) over the iteration process is depicted in Fig. 7-3. It can be known from Fig. 7-3 that the potential scale reduction factors fluctuate during the first half length and then stably decrease during the last half iterations until convergence ($\hat{R}_i < 1.2, i = 1, \ldots, d$).

Additionally, how well the chains are mixing and how they move around the searching space are displayed by visual inspection, as shown in Fig. 7-4(a), (c), and (e). Fig. 7-4 shows that sampled values for three parameters gradually converge to concentrated areas from initially broad ranges. It indicates that this calibration model works well for the parabolic regression model.

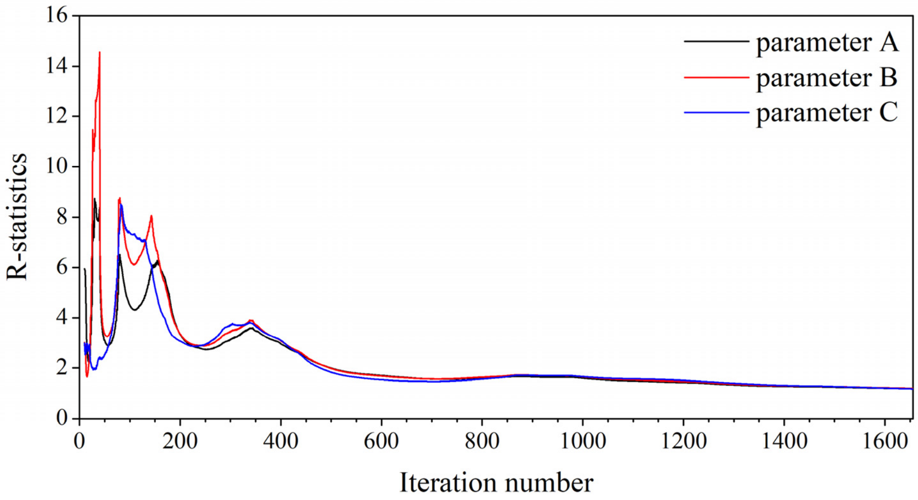

Fig. 7-3 Trace plot of R-statistics with increasing iterations.

Owing to the stable convergence, the marginal distributions are able to represent the posterior distributions for parameters. The sampled values in the second half iterations are used to estimate the posterior distribution for the parameters of the parabolic regression model, as shown in Fig. 7-4.

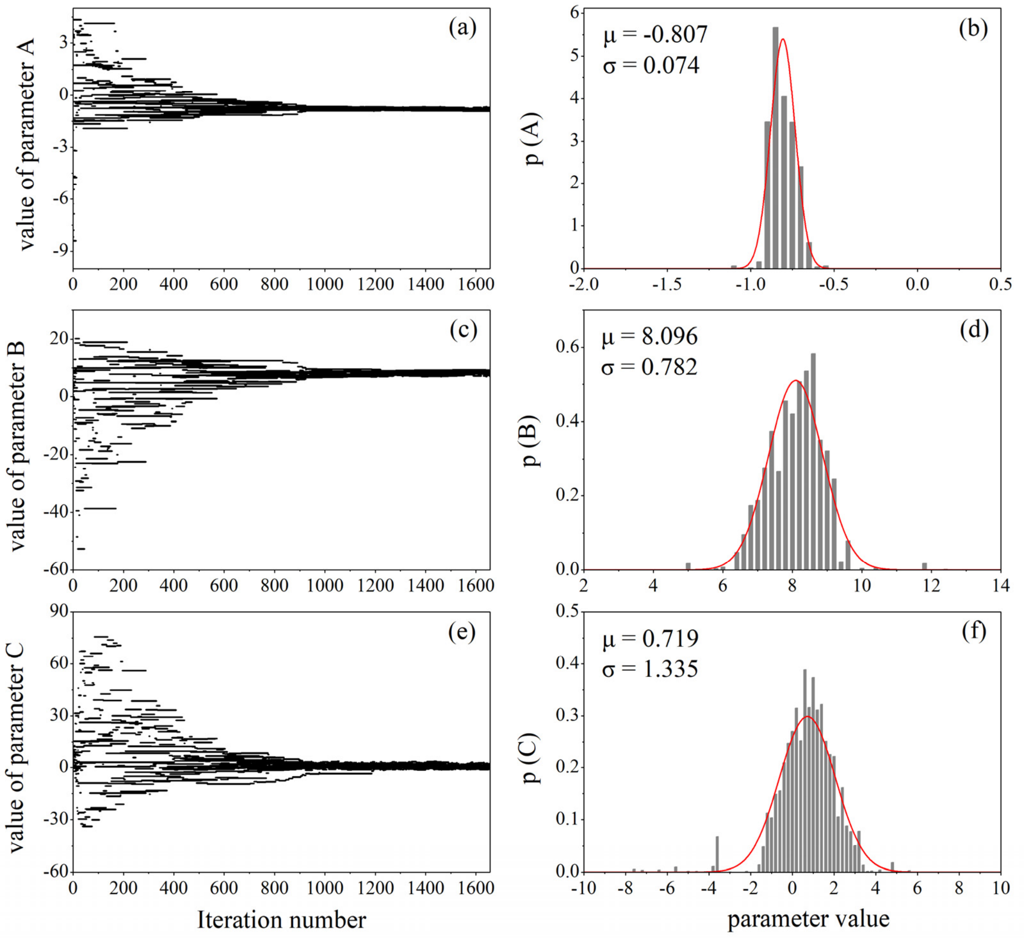

Fig. 7-4 Trace plots and probability density function for three parameters in the defined parabolic regression model. (a) and (b) for parameter A, (c) and (d) for parameter B, (e) and (f) for parameter C.

The mean of normal distribution is selected as the parameter value in the parabolic regression model, i.e. A = -0.807 (as shown in Fig. 7-4(b)), B = 8.096 (as shown in Fig. 7-4(d)), C = 0.719 (as shown in Fig. 7-4(f)). Hence, the estimated parabolic regression model by calibrated parameter values is shown as Fig. 7-5 (red line); the estimated curve nearly coincides with the synthetic curve. This illustrates that this automatic calibration program based on the DREAM algorithm performs excellent for calibrating parameters in the parabolic regression model.

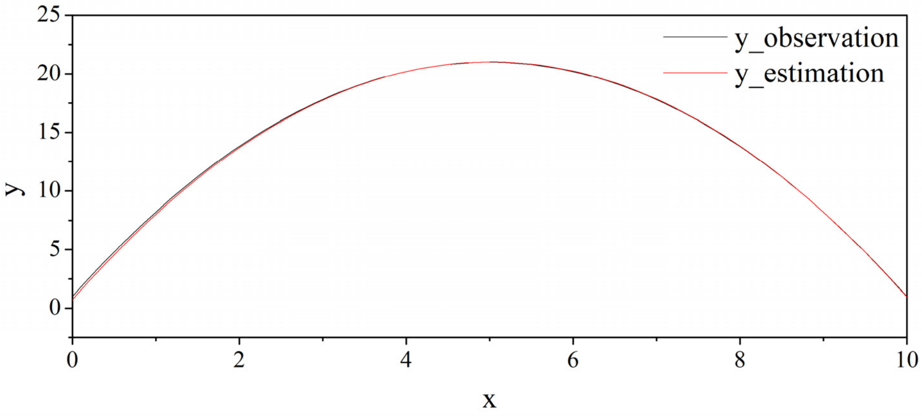

Fig. 7-5 Comparison of observed and estimated parabolic regression models.

8 Reference

Arnell, N. W. (2003). Effects of IPCC SRES* emissions scenarios on river runoff: a global perspective. Hydrol. Earth Sys. Sci., 7(5), 619–641.

Arnell, N. W. (2004). Climate change and global water resources: SRES emissions and socio-economic scenarios. Global. Envion. Change. 14, 31–52.

Ashby, S. F. and R. D. Falgout (1996). A parallel multigrid preconditioned conjugate gradient algorithm for groundwater flow simulations. Nucl. Sci. Eng., 124, 145–159.

Bao, H. and L. Zhao (2011). Hydraulic model with roughness coefficient updating method based on Kalman filter for channel flood forecast. Water Sci. Eng., 4(1), 13–23, doi:10.3882/j.issn.1674-2370.2011.01.002.

Bao, Y., C. Meng, S. Shen, X. Qiu, P. Gao, C. Liu (2011). Temporal and spatial patterns of droughts for recent 50 years in Jiangsu based on meteorological drought composite index (in Chinese). Acta Geogr. Sin., 66(5), 599–608.

Bastiaanssen, W. G. M., M. Menenti, R. A. Feddes, et al. (1998). A remote sensing surface energy balance algorithm for land (SEBAL): 1. Formulation. J. Hydrol., 212/213(1/2/3/4): 198–212.

Beaumont, M. A., W. Zhang, D. J. Balding (2002). Approximate Bayesian computation in population genetics. Genetics, 162(4), 2025–2035.

Berg, P., S. Wagner, H. Kunstmann, G. Schaedler (2013). High resolution climate model simulations for Germany: Part 1 –validation. Clim. Dyn., 40(1–2), 401–414, doi:10.1007/s00382-012-1508-8.

Beven, K. J. and M. J. Kirkby (1979). A physically bases, variable contributing area model of basin hydrology. Hydrol. Sci. J., 24, 43–69.

Booij, M. J. (2005). Impact of climate change on river flooding assessed with different spatial model resolutions. J. Hydrol., 303, 176–198.

Brooks, R. H. and A. T. Corey (1964). Hydraulic properties of porous media. Hydrology Paper 3, Colorado State University, Fort Collins.

Butts, M., M. Drews, M. A.D. Larsen, S. Lerer, S. Rasmussen, J. Groos, J. Overgaard, J. C. Refsgaard, O. Christensen, J. H. Christensen (2014). Embedding complex hydrology in the regional climate system – Dynamic coupling across different modelling domains. Adv. Water Res., 74, 166–184.

Calanca, P. (2007). Climate change and drought occurrence in the Alpine region: How severe are becoming the extremes. Glob. Planet. Change, 57, 151–160.

Chen, J. and P. Kumar (2001). Topographic influence on the seasonal and interannual variation of water and energy balance of basins in North America. J. Climate, 14, 1989–2014.

Chen, X., Z. Wang, and Z. Wang (2013). Analysis of drought characteristic in the Huaihe River basin in recent 60 years. South-to-North Water Transfers and Water Sci. & Tech., 11(6): 20–24.

Clapp, R. B. and G. M. Hornberger (1978). Empirical equations for some soil hydraulic properties. Water Resour. Res., 14, 601–604.

Clark, D. B. and N. Gedney (2008). Representing the effects of subgrid variability of soil moisture on runoff generation in a land surface model. J. Geophys. Res., 113, D10111, doi:10.1029/2007JD008940.

Cosby, B. J., R. B. Hornberger, R. B. Clapp and T. R. Ginn (1984). A statistical exploration of the relationships of soil moisture characteristics to the physical properties of soils. Water Resour. Res., 20, 682–690.

Dai, Y. J. and Q.-C. Zeng (1997). A land surface model (IA94) for climate studies. Part I: Formulation and validation in offline experiments. Adv. Atmos. Sci., 14, 433–460.

De Graaf, I. E.M., R. L.P.H. van Beek, T. Gleeson, N. Moosdorf, O. Schmitz, E. H. Sutanudjaja, M. F.P. Bierkens (2017). A global-scale two-layer transient groundwater model: Development and application to groundwater depletion. Adv. Water Resour., 102, 53–67.

Easterling, D. R., J. L. Evans, P. YA. Groisman, T. R. Karl, K. E. Kunkel, P. Ambenje (2000). Observed variability and trends in extreme climate events: a brief review. Bull. Am. Meteorol. Soc., 81, 417–425.

Famiglietti, J. S. and E. F. Wood (1994). Multiscale modeling of spatially variable water and energy balance processes. Water Resour. Res., 30, 3061–3078.

Fersch, B. and H. Kunstmann (2014). Atmospheric and terrestrial water budgets: Sensitivity and performance of configurations and global driving data for long term continental scale WRF simulations. Clim. Dyn., 42(9–10), 2367–2396, doi:10.1007/s00382-013-1915-5.

Gelman, A. and D. B. Runbin (1992). Inference from iterative simulation using multiple sequences. Stat. Sci., 7, 457–472.

Gochis, D. J., W. Yu, D. N. Yates (2015). The WRF-Hydro model technical description and user's guide, version 3.0, NCAR Technical Document, pp. 1–120, available online at: http://www.ral.ucar.edu/projects/wrf_hydro/.

Godfrey, C. M. and D. J. Stensrud (2010). An empirical latent heat flux parameterization for the Noah land surface model. J. applied Meteor. Clim., 49: 1696–1713.

Groisman, P. YA. and R. W. Knight (2008). Prolonged dry episodes over the conterminous United States: new tendencies emerging during the last 40 years. J. Clim., 21: 1850–1862.

Guo, S., J. Wang, L. Xiong, A. Ying, D. Li (2002). A macro-scale and semi-distributed monthly water balance model to predict climate change impacts in China. J. Hydrol. 268, 1–15.

Haario, H., E. Saksman, J. Tamminen (1999). Adaptive proposal distribution for random walk Metropolis algorithm. Comp. Stat., 14, 375–395.

Haario, H., E. Saksman, J. Tamminen (2001). An adaptive algorithm. Bernoulli, 7, 223–242.

Habets, F., J. Noilhan, C. Golaz, J. P. Goutorbe, P. Lacarrère, E. Leblois, E. Ledoux, E. Martin, C. Ottlé, D. Vidal-Madjar (1999a). The ISBA surface scheme in a macroscale hydrological model applied to the Hapex-Mobilhy area; Part I: Model and database. J. Hydrol., 217, 75–96.

Habets, F., J. Noilhan, C. Golaz, J. P. Goutorbe, P. Lacarrère, E. Leblois, E. Ledoux, E. Martin, C. Ottlé, D. Vidal-Madjar (1999b). The ISBA surface scheme in a macroscale hydrological model applied to the Hapex-Mobilhy area; Part I: simulation of streamflows and annual water budget. J. Hydrol., 217, 97–118.

Habets, F., P. Etchevers, C. Golaz, E. Leblois, E. Ledoux, E. Martin, J. Noilhan, C. Ottlé (1999c). Simulation of the water budget and the river flows of the Rhone basin. J. Geophys. Res., 104, 31,145–31,172.

Hasting, W. K. (1970). Monte Carlo sampling methods using Markov chains and their applications. Biometrika, 57(1), 97–109.

Hostetler, S. W. (1994). Hydrologic and atmospheric models: the (continuing) problem of discordant scales (an editorial comment). Clim. Change, 27, 345–350.

Huang X. (1992). Hydrology (in Chinese). Beijing: Higher Education Press, 89–99.

Klein Tank, A. M. G. and G. P. Können (2003). Trends in indices of daily temperature and precipitation extremes in Europe, 1946–1999. J. Clim., 16, 3665–3680.

Klein Tank, A. M. G., T. C. Peterson, D. A. Quadir, S. Dorji, X. Zou, H. Tang, K. Santhosh, U. R. Joshi, A. K. Jaswal, R. K. K. Kolli, A. B. Sikder, N. R. Deshpande, J. V. R. Revadekar, K. Yeleuova, S. Vandasheva, M. Falezeva, P. Gomboluudev, K. P. Budhathoki, A. Hussain, M. Afzaal, L. Chandrapala, H. Anvar, D. Amanmurad, V. S. Asanova, P. D. Jones, M. G. New. T. K. Spektorman (2006). Changes in daily temperature and precipitation extremes in central and south Asia. J. Geophys. Res. 111, D16105, doi:10.1029/2005JD006316.

Lehner, B., P. Döll, J. Alcamo, T. Henrichs, F. Kaspar (2006). Estimating the impact of global change on flood and drought risks in Europe: A continental, integrated analysis. Climate Change, 75, 273–299.

Leopold, L. B., and T. J. Maddock (1953). The hydraulic geometry of stream channels and some physiographic implications, U.S. Geol. Surv. Prof. Pap., 252, 56pp.

Levine, J. B. and G. D. Salvucci (1999). Equilibrium analysis of groundwater-vadose zone interactions and the resulting spatial distribution of hydrologic fluxes across a Canadian prairie. Water Resour. Res., 35(5), 1369–1383.

Li, M., Z. Lin, C. Yang, Q. Shao (2014). Application of a coupled land surface-hydrological model to flood simulation in the Huaihe River Basin of China. Atmos. Oceanic Sci. Lett., 7:6, 493–498.

Li, M., Z. Lin, Y. Shao, C. Yang, S. Liu (2015). Improvement of a coupled land surface-hydrological model with calibrated hydraulic parameters (in Chinese). Clim. Environ. Res., 20(2), 141–153.

Liang, X., D. P. Lettenmaier, E. F. Wood, S. J. Burges (1994). A simple hydrologically based model of land surface water and energy fluxes for generation circulation models. J. Geophys. Res., 99, 14,415–14,428.

Liang, X., E. F. Wood, D. P. Lettenmaier (1996). Surface soil moisture parameterization of the VIC-2L model: evaluation and modification. Global Planet. Change, 13, 195–206.

Manabe, S., J. Smagorinsky, R. F. Strickler (1965). Simulated climatology of a general circulation model with a hydrologic cycle. Mon. Wea. Rev., 93, 769–798.

Maplet (2016, Oct. 16th). The spatiotemporal variability of precipitation and evaporation in the Huaihe basin, China (in Chinese). Retrieved from http://www.maplet.org/post/e987a.

Maxwell, R. M., F. K. Chow, and S. J. Kollet (2007). The groundwater-land surface-atmosphere connection: Soil moisture effects on the atmospheric boundary layer in fully-coupled simulations. Adv. Water Resour., 30, 2447–2466.

Maxwell, R. M., J. K. Lundquist, J. D. Mirocha, S. G. Smith, C. S. Woodward, A. F. N. Tompson (2011). Development of a coupled groundwater-atmosphere model. Mon. Wea. Rev., 139, 96–116, doi:10.1175/2010MWR3392.1.

Maxwell, R. M. and N. L. Miller (2005). Development of a coupled land surface and groundwater model. J. Hydrometeor., 6, 233–247.

Maxwell, R. M. and S. J. Kollet (2008). Interdependence of groundwater dynamic and land-energy feedbacks under climate change. Nat. Geosci., 1, 665–669, doi:10.1038/nego315.

McDonald, M. G. and A. W. Harbaugh (1988). Techniques of water-resources investigations of the United States Geological Survey: a modular three-dimensional finite-difference groundwater flow model. United States GPO, Washington, pp. 6-1 – 6–36.

Middelkoop, H., K. Daamen, D. Gellens, W. Grabs, J. C. J. Kwadijk, H. Lang, B. W. A. H. Parmet, B. Schädler, J. Schulla, K. Wilke (2001). Impact of climate change on hydrological regimes and water resources management in the Rhine basin. Clim. Change, 49, 105–128.

Miller, J. R., G. L. Russel, and G. Caliri (1994). Continental-scale river flow in climate models. J. Clim., 7, 914–928.

Mölders, N. and A. Raabe (1997). Testing the effect of a two-way-coupling of a meteorological and a hydrologic model on the predicted local weather. Atmos. Res., 45, 81–107.

Neal, J., G. Schumann, and P. Bates (2012). A subgrid channel model for simulating river hydraulics and floodplain inundation over large and data sparse areas. Water Resour. Res., 48, W11506, doi:10.1029/2012WR012514.

Niu, G.-Y. and Z.-L. Yang (2003). The vetsatile integrator of surface and atmosphere processes (VISA); Part II: evaluation of three topography-based runoff schemes. Global Planet. Change, 38, 191–208.

Niu, G.-Y., Z.-L. Yang, R. E. Dickinson, L. E. Gulden (2005). A simple TOPMODEL-based runoff parameterization (SIMTOP) for use in global climate models. J. Geophys. Res., 110, D21106, doi:10.1029/2005JD006111.

Osman, Y. Z., M. P. Bruen (2002). Modelling stream-aquifer seepage in an alluvial aquifer: an improved loosing-stream package for MODFLOW. J. Hydrol., 264, 69–86.

Pollard, D. and S. L. Thompson (1995). Use of a land-surface-transfer scheme (LSX) in a global climate model: The response to doubling stomatal resistance. Global Planet. Change, 10, 129–161.

Qiu, Y., B. Fu, J. Wang, L. Chen (2001). Soil moisture variation in relation to topography and land use in a hillslope catchment of the Loess Plateau, China. J. Hydrol., 240 (3–4), 243–263.

Schneider, U., A. Becker, P. Finger, A. Meyer-Christoffer, B. Rudolf, and M. Ziese (2011). GPCC full data reanalysis version 6.0 at 0.5º: Monthly Global Precipitation Climatol. Cent., Offenbach, Germany, doi:10.5676/DWD_GPCC/FD_M_V6_050.

Seuffert, G., P. Gross, C. Simmer, E. F. Wood (2002). The influence of hydrologic modeling on the predicted local weather: Two-way coupling of a mesoscale weather prediction model and a land surface hydrologic model. J. Hydrometeor., 3, 505–523.

Shi, P., C. Gu, T. Chen (1992). 1991 flood and waterlogging and strategy to reduce disaster issue of rural area in Huaihe drainage basin of China (in Chinese). Acta Geogr. Sin., 47(5), 385–393.

Shrestha, P., M. Sulis, M. Masbou, S. Kollet, C. Simmer (2014). A scale-consistent terrestrial systems modeling platform based on COSMO, CLM, and ParFlow. Mon. Wea. Rev., 142, 3466–3483.

Skamarock, W., J. Klemp, J. Dudhia, D. Gill, D. Barker, M. Duda, X. Huang, W. Wang, and J. Powers (2008). A description of the Advanced Research WRF version 3, NCAR Tech. Note 475. Natl. Cent. for Atmo. Res., Boulder, Colo.

Song, S., L. Li, X. Chen, J. Bai (2015). The dominate role of heavy precipitation in precipitation change despite opposite trends in west and east of northern China. Int. J. Climatol., 35, 4329–4336.

Stieglitz, M., D. Ring, J. Famiglietti, C. Rosenzweig (1997). An efficient approach to modeling the topographic control of surface hydrology for regional and global climate modeling. J. Climate, 10, 118–137.

Storn, R. and K. Price (1997). Differential Evolution – a simple and efficient heuristic for global optimization over continuous spaces. J. Global Optim., 11, 341–359.

Strzepek, K., G. Yohe, J. Neumann, B. Boehlert (2010). Characterizing changes in drought risk for the United States from climate change. Environ. Res. Lett., 5, doi:10.1088/1748-9326/5/4/044012.

Ter Braak, Cajo J. F. (2006). A Markov chain Monte Carlo version of the genetic algorithm Differential Evolution: easy Bayesian computing for real parameter spaces. Stat. Comput., 16, 239–249.

Tian, W., X. Li, G.-D. Cheng, X.-S. Wang, B. X. Hu (2012). Coupling a groundwater model with a land surface model to improve water and energy cycle simulation. Hydrol. Earth Syst. Sci. Discuss, 16, 4707–4723.

Tostes, J. O., G. B. Lyra, J. F. Oliveira-Júnior, M. R. Francelino (2017). Assessment of gridded precipitation and air temperature products for the State of Acre, southwestern Amazonia, Brazil. Environ. Earth Sci., 76(4), DOI: 10.1007/s12665-017-6467-2.

Toth, J. (1962). A theory of groundwater motion in small drainage basins in central Alberta, Canada. J. Geophys. Res., 67(11), 4375–4387.

Trenberth, K. E., P. D. Jones, P. Ambenje, R. Bojariu, D. Easterling, A. Klein Tank, D. Parker, F. Rahimzadeh, J. A. Renwick, M. Rusticucci, B. Soden and P. Zhai (2007). Observations: Surface and Atmospheric Climate Change. In: Climate Change 2007: The Physical Science Basis. Contribution of Working Group I to the Fourth Assessment Report of the Intergovernmental Panel on Climate Change [Solomon, S., D. Qin, M. Manning, Z. Chen, M. Marquis, K. B. Averyt, M. Tignor and H. L. Miller (eds.)]. Cambridge University Press, Cambridge, United Kingdom and New York, NY, USA.

Valcke, S. (2013). The OASIS3 coupler: a European climate modelling community software. Geosci. Model Dev., 6, 373–388, doi:10.5194/gmd-6-373-2013.

Van Genuchten, M. Th. (1980). A close-form equation for predicting the hydraulic conductivity of unsaturated soils. Soil Sci. Soc. Am. J., 44, 892–898.

Vrugt, J. A., C. J. F. ter Braak, G. H. Diks, B. A. Robinson, J. M. Hyman (2008). Accelerating Markov chain Monte Carlo simulation by differential evolution with self-adaptive randomized subspace sampling. Int. J. Nonlinear Sci. Numer. Simul., in press.

Vrugt, J. A. and M. Sadegh (2013). Toward diagnostic model calibration and evaluation: Approximate Bayesian computation. Water Resour. Res., 49, 4335–4345.

Wagner, S., Fersch B., Yuan F., Z. Yu, H. Kunstmann (2016). Fully coupled atmospheric-hydrological modeling at regional and long-term scales: Development, application, and analysis of WRF-HMS. Water Resour. Res., 52, 3187–3211, doi:10.1002/2015WR018185.

Walko, R. L., L. E. Band, J. Baron, T. G. F. Kittel, R. Lammers, T. J. Lee, D. Ojima, R. A. Pielke Sr., C. Taylor, C. Tague, C. J. Tremback, P. L. Vidale (2000). Coupled atmosphere-biophysics-hydrology models for environmental modeling. J. Appl. Meteor., 39, 931–944.

Warrach, K., M. Stiegltz, H. T. Mengelkamp, and E. Raschke (2002). Advantages of a topographical controlled runoff simulation in a soil-vegetation-atmosphere transfer model. J. Hydrometeor.,131–148.

Willmott, C. J. and K. Matsuura (n.d.). Monthly global gridded high resolution station (land) data for air temperature and precipitation from 1900–2014. Available on https://www.esrl.noaa.gov/psd/data/gridded/data.UDel_AirT_Precip.html.

Xu, Y.-P., X. Zhang, Q. Ran, Y. Tian (2013). Impact of climate change on hydrology of upper reaches of Qiantang River Basin, East China. J. Hydrol., 483, 51–60.

Yan, Z., J. Xia, L. Gottschalk (2010). Mapping runoff based on water balance: a case study of the Huaihe River basin above Bengbu. Acta Geogr. Sin., 65(7), 841–852.

Yang, C., Y. Shao, Z. Lin, et al. (2011). Development of a two-way coupled land surface-hydrology model: Method and application, in: Proceedings of International Symposium on climate change and water (ISCCCW), Nanjing, 20–21 April, 2011, 309–317.

Yang, C., Z. Yu, Z. Hao, J. Zhang, J. Zhu (2012). Impact of climate change on flood and drought events in Huaihe River Basin, China. Hydrol. Res., 43, 14–22, doi:10.2166/nh.2011.112.

Yang, X., G. Wang, J. Ye, and Y. Li (2015). Spatial and temporal changing analysis of terrestrial evapotranspiration in Huai River basin based on GLEAM data (in Chinese). Transactions of the Chinese Society of Agricultural Engineering, 31(9): 133–139.

Ye, Z. and Z. Li (2017). Spatiotemporal variability and trends of extreme precipitation in Huaihe River basin, a climatic transitional zone in east China. Adv. Meteor., doi.org/10.1155/2017/3197435.

Yeh, P. J.-F. and E. A. B. Eltahir (2005a). Representation of water table dynamics in a land surface scheme. Part I: model development. J. Climate, 18, 1861–1880.

Yeh, P. J.-F. and E. A. B. Eltahir (2005b). Representation of water table dynamics in a land surface scheme. Part II: subgrid variability. J. Climate, 18, 1881–1901.

Yu, B., J. Ni, P. Ben, P. Wu, J. Sui (2016). The combined operation of flood plain and flood diversion channel in the middle reach of Huaihe River. 1797–1803. River Flow 2016 [Constantinescu, G., M. Garcia, D. Hanes (eds.)]. Taylor & Francis Group, London, ISBN 978-1-138-28912-8.

Yu, P.-S., T.-C. Yang, C.-K. Wu (2002). Impact of climate change on water resources in southern Taiwan. J. Hydrol., 260, 161–175.

Yu, Z., D. Pollard, L. Cheng (2006). On continental-scale hydrologic simulations with a coupled hydrologic model. J. Hydrol., 331, 110–124.

Zeng, X. and M. Decker (2009). Improving the numerical solution of soil moisture-based Richards equation for land models with a deep or shallow water table. J. Hydrometeor., 10, 308–319.

Zhang, Y., P. Zhai, and Y. Qian (2005). Variations of Meiyu indicators in the Yangtz-Huaihe River Basin during 1954–2003. Acta Meteor. Sin., 4(19), 479–484.

Zhao, R. J. (1992). The Xinanjiang model applied in Chian. J. Hydrol., 134, 317–381.

9 Acknowledgements

I would like to express my gratitude to my supervisor Prof. Dr. Yaping Shao, who has inspired, motivated and guided me on this challenging research topic. My horizons have been boarded under his guidance and encouragement. I am grateful to him for training me in programming and modelling, and leading me in academical research.

I thank Prof. Dr. Karl Schneider for being the second reviewer of my thesis and giving me good advices for academic research.

This work was granted by the China Scholarship Council (CSC). I would like to thank the consultant in the China Consulate General in Dusseldorf, Dr. Xia Lu, for her helps and supports. I thank Prof. Dr. Zhihui Liu from Chinese Academy of Sciences for offering me help and sharing me some academic experience.

I would like to thank Dr. Chi Yan Tsui for his instructions on FORTRAN programming and using Linux operating system, and Dr. Sven Ulbrich for his technique supports for modelling. And I would like to thank Dr. Mark Reyers, Dr. Cedrick Ansorge, Dr. Sven Ulbrich, and Dr. Chi Yan Tsui for their professional suggestions and proof-readings.

I also wish to thank other group members, Dr. Donata Banyte, Dr. Jie Zhang, Dr. Martina Klose, Dr. Michael Hintz, Dr. Patrick Ludwig, Dr. Shaofeng Liu, Dr. Stefanie Neske, Dr. Zhuoqun Li, Dr. Erik Jan Schaffernicht, Christian Wegener, Cong Jiang, Konstantin Klein, Philipp Henckes, Philipp Schlüter, Robert Daniel Rauterkus, Xin Yin, Zahrasadat Parsakhoo for the discussion of my work in group meetings. In addition, I wish to express my thanks to all the colleagues in the institute for Geophysics and Meteorology for their friendly to me.

Last but not least, I appreciate the understanding and support of my beloved family throughout these years. Very special thanks go to my husband Dr. Yangzhen Fan for his supports and encouragement as always.

10 Erklärung

Ich versichere, dass ich die von mir vorgelete Dissertation selbständing angefertigt, die benutzen Quellen und Hilfsmittel vollständig angegeben und die Stellen der Arbeit – einschließlich Tabellen, Karten unde Abbildungen –, die anderen Werken im Wortlaut oder dem Sinn nach entnommen sind, in jedem Einzelfall als Entlehnung kenntlich gemacht habe; dass diese Dissertation noch keiner anderen Fakultät oder Universität zur Prüfung vorgelen hat; dass sie – abgesehen von unten angegebenen Teilpublikationen – noch nicht veröffentlicht worden ist sowie, dass ich eine solche Veröffentlichung vor Abschluss des Promotionsverfahrens nicht vornehmen werde. Die Bestimmungen dieser Promotionsordung sind mir bekannt. Die von mir vorgelegte Dissertation ist von Prof. Dr. Y. Shao betreut worden.

Teilpublikationen liegen nicht vor.

Köln, den 18. 03. 2019

Qian Xia